UNIVERSITY OF HELSINKI REPORT SERIES IN ASTRONOMY

No. 25

Hydrodynamical simulations and synthetic observations of merging galaxies

Natalia Lahén

Academic dissertation

Department of Physics
Faculty of Science
University of Helsinki
Helsinki, Finland

To be presented, with the permission of the Faculty of Science of the University of Helsinki, for public criticism in Auditorium I of the Metsätalo building (Unionkatu 40, Helsinki) on June 8th 2020, at 12 o'clock noon.

Helsinki 2020

Cover picture: A colour-composite image of the merging Antennae galaxies (NGC 4038/4039) at various wavelengths from 435 nanometres (optical B-band) to 2.6 millimetres composed of observations made with the Atacama Large Millimetre/submillimetre Array and the Hubble Space Telescope. Credit: ALMA (ESO/NAOJ/NRAO). Visible light image: the NASA/ESA Hubble Space Telescope.

ISSN 1799-3024 (print version)
ISBN 978-951-51-6133-8 (print version)
Helsinki 2020
Helsinki University Print (Unigrafia)

ISSN 1799-3024 (pdf version)
ISBN 978-951-51-6134-5 (pdf version)
ISSN-L 1799-3024

http://ethesis.helsinki.fi/
Helsinki 2020
Electronic Publications @ University of Helsinki
(Helsingin yliopiston verkkojulkaisut)

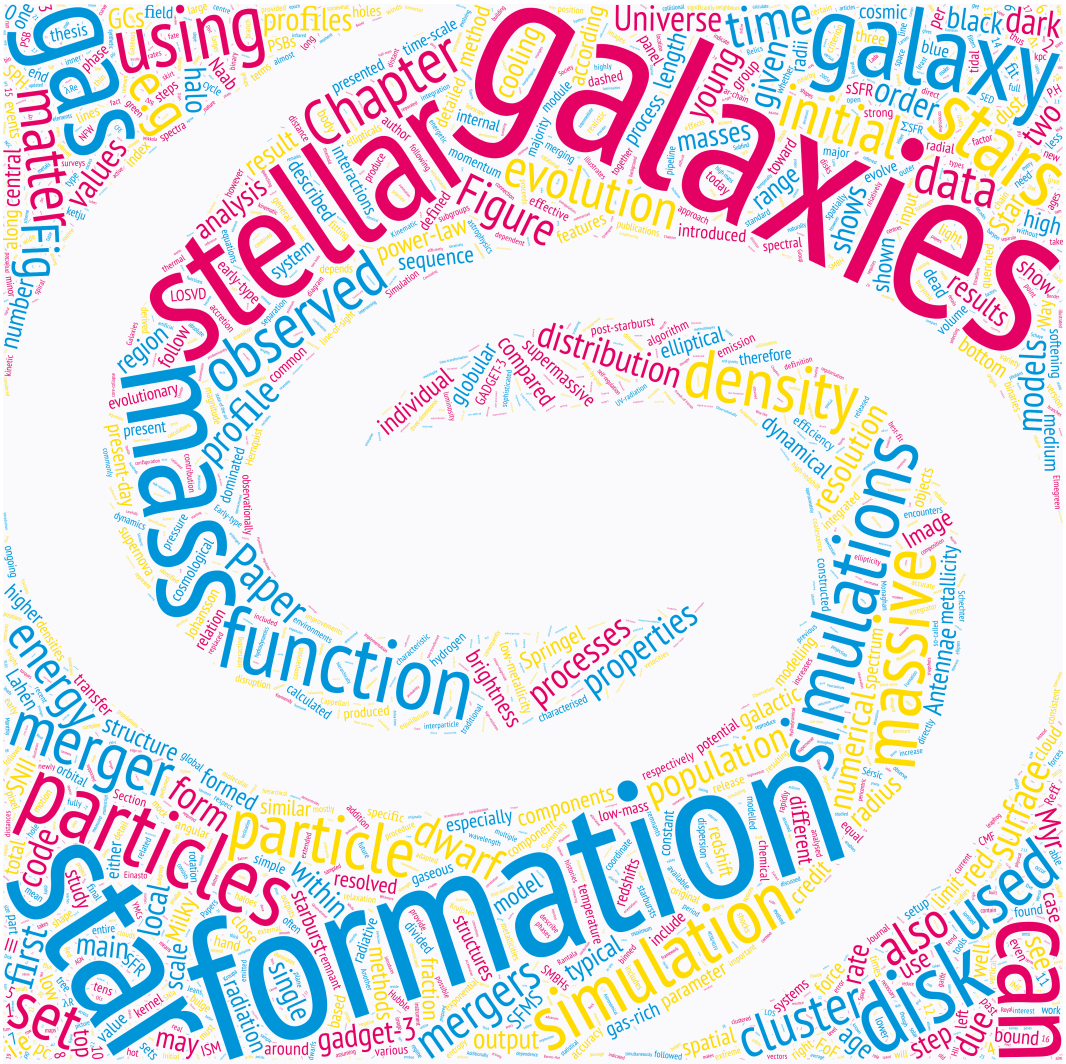
galaxies
formation
stellar
simulations
star
mass
function
particles
galaxy
data
stars
time
using
Universe
Chapter
evolution
Figure
observed
density
distribution
simulation
massive
profile
paper
properties
processes
energy
merger
particle
dwarf
population
resolution
disk
used
also
cluster
mergers
gadget-3
methods
single
first
set
matter
dark
black
cosmic
given
young
initial
order
shows
results
models
high
show
Stars
two
region
sequence
power-law
analysis
result
system
early-type
LOSVD
follow
evolutionary
present
present-day
dominated
cosmological
individual
globular
compared
supermassive
post-starburst
algorithm
elliptical
emission
therefore
efficiency
dynamical
mediated
objects
encounters
Image
metallicity
Antennae
numerical
spectrum
radius
galactic
modelling
constructed
credit
different
equal
redshift
chemical
dispersion
potential
respectively
release
low-mass
components
especially
similar
formed
form
structure
transfer
Laherty
higher
Springel
hydrogen
brightness
low-metallicity
characterised
produced
calculated
disruption
relation
Johansson
Sérsic
Elmegreen
softening
medium
bottom
dead
volume
shown
input
light
spectral
approach
introduced
today
range
toward
major
radial
ΣSFR
sSFR
strong
tidal
blue
three
pair
kpc
dust
less
new
high
Wetzel
quenched
Sagittarius
Kinetic
number
along
central
values
eg
using
Naab
halo
profiles
holes
field
GCs
thesis
One
SPH
end
phase
steps
cycle
lines
Spectra
induced
ketju
distance
described
interactions
produce
author
following
dynamic
momentum
merging
module
majority
internal
detailed
method
cooling
according
time-scale
presented
dashed
process
length
panel
Universe
Chapter
evolution
Figure
observed
density
distribution
simulation
massive
profile
paper
properties
processes
energy
merger
particle
dwarf
population
resolution
disk
used
also
cluster
mergers
gadget-3
methods
single
first
set
matter
dark
black
cosmic
given
young
initial
order
shows
results
models
high
show
Stars
two
region
sequence
power-law
analysis
result
system
early-type
LOSVD
follow
evolutionary
present
present-day
dominated
cosmological
individual
globular
compared
supermassive
post-starburst
algorithm
elliptical
emission
therefore
efficiency
dynamical
mediated
objects
encounters
Image
metallicity
Antennae
numerical
spectrum
radius
galactic
modelling
constructed
credit
different
equal
redshift
chemical
dispersion
potential
respectively
release
low-mass
components
especially
similar
formed
form
structure
transfer
Laherty
higher
Springel
hydrogen
brightness
low-metallicity
characterised
produced
calculated
disruption
relation
Johansson
Sérsic
Elmegreen
softening
medium
bottom
dead
volume
shown
input
light
spectral
approach
introduced
today
range
toward
major
radial
ΣSFR
sSFR
strong
tidal
blue
three
pair
kpc
dust
less
new
high
Wetzel
quenched
Sagittarius
Kinetic
number
along
central
values
eg
using
Naab
halo
profiles
holes
field
GCs
thesis
One
SPH
end
phase
steps
cycle
lines
Spectra
induced
ketju
distance
described
interactions
produce
author
following
dynamic
momentum
merging
module
majority
internal
detailed
method
cooling
according
time-scale
presented
dashed
process
length
panel

"I hope you'll make mistakes. If you're making mistakes, it means you're out there doing something."

From Make Good Art
by Neil Gaiman

Natalia Lahén: **Hydrodynamical simulations and synthetic observations of merging galaxies**, University of Helsinki, 2020, 75 p. + appendices, University of Helsinki Report Series in Astronomy, No. 25, ISSN 1799-3024 (print version), ISBN 978-951-51-6133-8 (print version), ISSN 1799-3024 (pdf version), ISBN 978-951-51-6134-5 (pdf version), ISSN-L 1799-3024

Abstract

Interactions and mergers between galaxies are among the most spectacular astrophysical phenomena that drive morphological transformations of galaxies as they evolve throughout cosmic times. Specifically, galactic encounters induce star formation due to the compression of the interstellar medium through tidal torques, ram pressure and shocks. The in-situ star formation process is in turn self-regulated by various stellar feedback processes, such as ultraviolet radiation from young massive stars and energetic supernova explosions. The thermodynamical processes in the interstellar gas with temperatures ranging from a few degrees to millions of Kelvins, coupled with the stellar lifecycle, are therefore the subjects of a wide range of ongoing observational and numerical studies. Significant technological advances in recent decades have resulted in a general framework for the formation and evolution of galaxies, but the complete astrophysical picture still remains incomplete.

Here we study the evolution of galaxies undergoing mergers by running high-resolution hydrodynamical simulations. We use state-of-the-art numerical methods, post-processing methods, and observational data analysis tools. The simulations presented here span a wide range of initial conditions from gas-rich dwarf galaxies, through Milky Way-like disk galaxies, to massive early-type galaxies which include central supermassive black holes. The employed simulation methods include some of the most sophisticated astrophysical models available for galactic-scale simulations. The cooling of the star-forming gas is modelled in detail using a chemical network, and the newly formed stars sample a mass resolution down to the masses of individual massive stars. We also follow the spatially and the temporally evolving interstellar radiation field emanating from the individually modelled stars into the surrounding interstellar medium, while simultaneously accounting for dust attenuation and gas self-shielding.

In this thesis we investigate how the extreme star formation environment produced by a gas-rich, low-metallicity dwarf galaxy merger can be used as a proxy

for the turbulent star formation conditions present in the high-redshift Universe. Specifically, we follow the formation of a population of young star clusters during the interactions of dwarf galaxies. We show that the star cluster formation proceeds most efficiently during the starburst phase. Young star clusters are, however, already present with an observationally consistent power-law mass function after the first pericentric passage. We take special interest in the formation and early evolution of the three most massive star clusters, which form hierarchically during the most intense starburst. These objects are shown to evolve in terms of their sizes and surface mass densities to resemble the present-day globular clusters observed in the Local Group.

Another simulation, specifically set up to reproduce the observed properties of the Antennae galaxy merger (NGC 4038/4039), is in turn used to study the spatially extended star formation during a disk galaxy merger. The simulation output is post-processed using radiative transfer and the results are reduced with observational data analysis methods. We compare the spatial star formation properties and the metallicity distribution to the observed present-day Antennae. We further follow the enrichment of the interstellar medium through stellar winds and supernovae, and show how the merger remnant evolves into a red and dead elliptical galaxy. We continue simulating the Antennae merger for a prolonged period of time after the coalescence of the galactic disks, and use the surface brightness and kinematic properties of the simulated remnant to search for an observational counterpart to the possible future fate of the present-day Antennae galaxies.

The outputs of our numerical simulations are used as well to discern how long a period a galaxy merger can be identified in optical images of observed mergers, and the results are used in building a comprehensive picture of the origin of post-starburst galaxies. Finally, we show how the supermassive black holes, found in the centres of all massive early-type galaxies, end in binaries at the centres of merger remnants of elliptical galaxies. The binaries scour the galactic centres while producing cored surface brightness profiles often observed in ellipticals, and coalesce as a result of gravitational wave driven binary evolution.

Acknowledgements

This thesis contains 352 (intro) + 930 (papers) mentions of the word *galaxy*. I will here offer my sincerest gratitude to all the people who have either helped or entertained me during the past five years of gathering the galactic knowledge.

First I would like to address my gratitude to my supervisor Professor Peter Johansson for guiding me throughout almost my entire academic education. His door has always been open for discussions and advice both on and off-topic. I am also extremely grateful for the continuous support of Dr. Thorsten Naab and his immeasurably valuable advice regarding an academic career and life in general without which I would maybe not have pursued to apply for post-doc positions in astrophysics.

The finalisation of the thesis and the preparations for the defence coincided with the time when the COVID-19 situation exploded and made the practicalities somewhat difficult to handle. I would like to address an enormous thank you to my opponent Clare Dobbs for her flexibility and interest with the defence process. I am sorry she cannot see the full Finnish academic defence tradition! I want to also thank the thesis pre-examiners Professor Seppo Mattila and Dr. Diederik Kruijssen for their on-point and extremely encouraging reports.

Our Theoretical Extragalactic Research group has provided a low-pressure environment where the quality of our work is appreciated above all else. I thank my science big brothers Pauli Pihajoki (for IT-support and mutual online-rants), Till Sawala (for being a role model in many aspects of life) and Stuart McAlpine (for showing that science should not always be so serious).

The relaxed environment in the Physicum 3rd floor D-corridor has been a wonderful place to work. I have fully enjoyed all the hour-long coffee breaks, Christmas parties, outing events and so on. Mika, Akke, Teemu, Matias, Thomas, Mikael, Jorma, Laura Z., Olli W., thank you for the chats! I also want to address special thanks to Emma for the procrast... writing company during the corona spring, and Elisabetta (and Guilhem!) and Erika (and Paul!) for reminding us all of the importance of social extracurricular activities.

It has been fascinating to follow the journeys of all the friends from undergraduate times. Even though our paths may branch, cross and diverge, for some reason broken printers seem to be a common denominator always worth a cry/laugh. Our juopot-chat (which has at the moment 57 members) has been an unending source of memes, IT-advice, free books and plants, and most importantly peer support. Just to mention a few, thank you Laura M., Joonatan, Anton, Antton, TeriSan, Amalia, Jere, Kaiu, Joona, AP, Ilmo, Kimmo, Krista, Noora, I never say it but I love you all!

I used to wish for a baby brother which would then turn into a big brother as we grow up (?!). I guess my wish was filled in the form of Jussi Aaltonen, because except for my partner I have spent more time with Jussi than anyone else ranting, drinking beer and playing boardgames. Thank you for always being there, in the good and the bad times!

My family now extends across to my to-be-mother-and-farther-in-law Päivi and Matti, and my to-be-sister-in-law Petra and her husband Aleksi (and the cats Luna and Hilda of course, *purr*). I want to thank them for always being interested in my wellbeing and making sure I know they believe in me regardless of my own doubts. Our yearly traditions, such as the Rapujuhlat, have been the bright beacons shining light into my gray everyday life as a PhD student!

During my journey towards a PhD and through the first 30 years I have always, unconditionally, been supported by my mother Tarja, her husband Hannu, my sister Oona, my grandmothers, and my aunts. My mom especially has always pushed me to exceed my internalised limitations and I am grateful to be able to rely on her advice any day. It gives me so much joy to be able to make her proud. Kiitos kaikille sukulaisille tuesta! Ja kertauksena, vaikka avaruus laajenee, se ei edelleenkään laajene *minnekään* koska avaruuden ulkopuolella ei ole mitään.

Finally, I address my eternal gratitude to my other half and my best friend/fiancé. We have supported each other throughout our joint struggle through the university life emotionally and scientifically ("together for scientific reasons *adjusts glasses*"), and I am so happy to be able to follow in his footsteps into the real world. Thank you Antti, we are the masters of the Galaxy!

List of publications

Paper I: Lahén, N., Johansson, P.H., Rantala, A., Naab, T., & Frigo, M., 2018, 'The fate of the Antennae galaxies', Monthly Notices of the Royal Astronomical Society, 475, 3934. DOI:10.1093/mnras/sty060-

Paper II: Lahén, N., Naab, T., Johansson, P.H., Elmegreen, B., Hu, C.-Y., Walch, S., 2019, 'Formation of low-metallicity globular clusters in dwarf galaxy mergers', The Astrophysical Journal Letters, 879, L18. DOI:10.3847/2041-8213/ab2a13

Paper III: Lahén, N., Naab, T., Johansson, P.H., Elmegreen, B., Hu, C.-Y., Walch, S., Steinwandel, U.P., Moster, B.P., 2019, 'The GRIFFIN project – formation of star clusters with individual massive stars in a simulated dwarf galaxy starburst', The Astrophysical Journal, 891, 2. DOI:10.3847/1538-4357/ab7190

Paper IV: Pawlik, M. M., Taj Aldeen, L., Wild, V., Mendez-Abreu, J., **Lahén, N.**, Johansson, P. H., Jimenez, N., Lucas, W., Zheng, Y., Walcher, C. J., Rowlands, K., 2018, 'The origins of post-starburst galaxies at $z < 0.05$', Monthly Notices of the Royal Astronomical Society, 477, 1708. DOI:10.1093/mnras/sty589

Paper V: Rantala, A., Pihajoki, P., Johansson, P.H., Naab, T., **Lahén, N.**, & Sawala, T., 2017. 'Post-Newtonian dynamical modeling of supermassive black holes in galactic-scale simulations', The Astrophysical Journal, 840, 53. DOI:10.3847/1538-4357/aa6d65

List of abbreviations

AGN	active galactic nucleus
CMF	cluster mass function
DM	dark matter
FoF	friends-of-friends algorithm
GC	globular cluster
HST	Hubble Space Telescope
IFU	integral field unit spectrograph
IMF	initial mass function
ISM	interstellar medium
pc, kpc, Mpc	parsec, kiloparsec, megaparsec
(U)LIRG	(ultra)luminous infrared galaxy
LOS	line-of-sight
LOSVD	line-of-sight velocity distribution
NFW	Navarro-Frenk-White profile
PSB	post-starburst
SED	spectral energy distribution
SF	star formation
SFR	star formation rate
SFMS	star-forming main sequence (of galaxies)
SMBH	supermassive black hole
SN (SNIa/II)	supernova (type Ia/II)
SPH	smoothed particle hydrodynamics
YMC	young massive star cluster

Contents

1 Introduction

1.1 Hydrodynamical simulations of galaxy mergers

The existence of galaxies outside of our local realm in the Milky Way was established almost a hundred years ago by Edwin Hubble (Hubble, 1925). Hubble was also the first person to attempt to explain how galaxies evolve throughout the cosmic ages (Hubble, 1926). Since then, our understanding of the evolutionary cycle of galaxies has been comprehensively rewritten. A vast array of observational surveys and numerical simulation studies have resulted in the currently favoured cosmological ΛCDM standard model. According to this model galaxies are dominated by dark matter and grow hierarchically bottom-up (White & Frenk, 1991). Thus, in this framework, mergers of galaxies play a crucial role in building up their stellar structure. The stellar mass in galaxies grows in mergers both through accretion of pre-existing stars, and in bursty episodes of in-situ star formation caused by gas compression due to tidal torques, ram pressure and internal shocks.

Observationally, we can only study each galaxy at one single epoch. Although all galaxies are unique, the statistical models based on the growing database of galaxies observed at different ages along the cosmic timeline can be used in constructing theories of the evolutionary cycle of galaxies. Hydrodynamical simulations, on the other hand, are an important tool in making connections between the observational results. Recent advancements in simulation methodology, such as the inclusion of advanced cooling models, and stellar and black hole feedback processes, have shed light onto many cosmic puzzles. For example, one of the most fundamental issues that has been solved was the over-cooling problem of star formation. Stars tended to form too efficiently in hydrodynamical simulations, resulting in galaxies with too high stellar masses, which was alleviated by the inclusion of detailed astrophysical models (Marinacci et al., 2014; Schaye et al., 2015).

The mass resolution of gas and stars in numerical simulations have today reached a point where the stellar particles can be directly sampled from an initial stellar mass function (Hu et al., 2017; Emerick et al., 2019). This enables the modelling of

the coupling between the interstellar medium and the stars through the interstellar radiation field, HII regions, and the supernova events produced by single stars. We are finally entering an era of galaxy simulations where we can follow the formation and evolution of galaxies at a resolution of single stars while simultaneously resolving global galactic-scale processes.

1.2 Synthetic observations

The observed spectrum emitted by stars in real galaxies is affected by internal, external, as well as observational factors. Firstly, the intrinsic properties such as the initial mass, age, rotational properties, temperature and metallicity of stars in a galaxy set the initial spectrum. Secondly, the interstellar conditions along the observed line-of-sight transform the spectrum as the photons get absorbed, re-emitted, and scattered due to the intervening gas and dust. Thirdly, a multitude of observational factors such as the atmospheric seeing, the use of a telescope, and the choice of the specific instruments blur the spatial information and limit the wavelength range of the observations.

A variety of data analysis tools for observations, such as for example GALFIT for photometric profile fitting (Peng et al., 2002), can also be used by the numerical simulation community. However, in order to enable a direct comparison between the observational data products and the output of numerical simulations, the data need to be processed through a pipeline which mimics processes affecting the observed data. The reduction of the simulation outputs has also to be able to produce realistic mock observations to be given as an input to the observational analysis tools.

The pipeline used in the reduction of the simulated data may involve for example radiative transfer calculations. The three-dimensional stellar particle data can be, for example, used to produce a spatially varying stellar spectrum. The spectra are transported through lines-of-sight and projected onto a two-dimensional observation plane. Most of the modern radiative transfer programs use observation-based models for the emission from the simulated stellar population and the interstellar dust, and model the radiation transport through the intervening dusty gas in one, two or three dimensions. A sophisticated three-dimensional radiative transfer code, such as SKIRT (Camps & Baes, 2015), can also take into account the full morphology and the chemical composition of the system under study. The output of such a code can be for example a ready-to-use FITS-format data cube that can be analysed with standard observational tools.

1.3 Aims of this thesis

The hydrodynamical simulation framework presented in this thesis was constructed to take full advantage of the state-of-the-art astrophysical models developed during the past few decades. The preparatory work included improvements to the chemical and stellar population properties of the initial conditions of the simulations. We also introduced the KETJU module, which is a novel dynamical method for the accurate modelling of small scale gravitational interactions. We pinned down the main post-processing methods necessary for a data reduction consistent with state-of-the-art observations, and constructed a pipeline for the production of mock observations. All the steps between the construction of the initial conditions and the analysis of the simulated observations have the common goal of maximising the realism in terms of the comparison to the observations.

This thesis aims first at building a comprehensive picture of the galaxy merger process using a variety of initial conditions and simulation methodologies. We present numerical simulations of mergers consisting of gas-rich dwarf galaxies, disk galaxies, and elliptical galaxies and follow the transformation of the galactic properties throughout the merger process. The simulations of low-metallicity gas-rich dwarf galaxy mergers are used to investigate the star formation process, and especially the formation of star clusters, in conditions resembling the high-redshift Universe. The disk galaxy mergers, one of which is constructed to reproduce the conditions in the observed Antennae galaxies, produce spatially extended star formation and merger remnants that evolve into elliptical galaxies. The elliptical galaxy mergers with central supermassive black holes produce triaxial stellar distributions, and the dynamical evolution of the supermassive black hole binaries formed during the mergers leads to the coalescence of the binaries in the centres of the merger remnants.

Secondly, we aim at assessing the ability of our simulation tools to produce observationally consistent outputs with respect to the star formation environment in merging galaxies. We also investigate in great detail how the clustered star formation and the formation of globular clusters proceed in our simulations. These processes are amongst those most intensely studied in both the numerical and the observational communities (Krumholz et al., 2019). Future observational facilities such as the James Webb Space Telescope and the Extremely Large Telescope will among other targets observe the sites of clustered star formation at high redshifts during the following decades (Vanzella et al., 2019).

1.4 Structure of this thesis

This thesis consists of two parts; an introduction followed by five original peer-reviewed journal articles, numbered I-V. The introductory part is organised as follows. The observational background of the evolutionary cycle of galaxies in the context of star formation is reviewed in Chapter 2. The tools for simulating processes related to star formation and the accurate gravitational dynamics of supermassive black holes in galaxy mergers are described in Chapter 3. In Chapter 4 we describe the initial conditions and post-processing methods used to reduce and interpret the simulation data products in an observationally motivated fashion. The articles and the detailed author's contribution are summarised in Chapter 5, and concluding remarks are given in Chapter 6.

2 Star formation in galaxies

The stellar mass of galaxies can grow either through in-situ star formation, accretion of stellar structures, or through minor and major mergers, with several processes potentially occurring simultaneously. The dominant mode of the stellar mass growth for a given galaxy depends on the redshift, the galaxy type and the surrounding environment. As galaxies evolve, they may alternate between these different modes, which makes it anything but straightforward to infer the current and future evolutionary state of a galaxy just by studying its visual image.

The general picture of the typical evolutionary pathways of galaxies can be drawn on a statistical basis. The observational data today spans millions of galaxies from large multiwavelength surveys such as the Sloan Digital Sky Survey (SDSS, York et al. 2000), which has been in operation for approximately 20 years. The level of star formation in galaxies is often quantified using the specific star formation rate (sSFR, $[\mathrm{yr}^{-1}]$), which is defined by normalising the star formation rate (SFR, $[\mathrm{M}_\odot\,\mathrm{yr}^{-1}]$) by the stellar mass M_* as

$$\mathrm{sSFR} = \frac{\mathrm{SFR}}{M_*}. \tag{2.1}$$

Fig. 2.1 shows a typical schematic for the sSFR as a function of the stellar mass, inferred from tens of thousands of galaxies in the SDSS data (Schiminovich et al., 2007). The coloured regions outlined in Fig. 2.1 are used to differentiate star-forming galaxies from the so-called red and dead galaxies. Low-mass and/or gas-rich galaxies, such as typical dwarf and disk galaxies, populate the blue top-left region of the figure, while massive gas-poor galaxies, such as the present-day early-type galaxies, fill the red bottom-right region.

The majority of the global star formation today takes place in galaxies that have an almost constant value of sSFR irrespective of their stellar mass. This population of galaxies has been collectively named the star-forming main sequence (SFMS) (Elbaz et al., 2011; Speagle et al., 2014). Galaxies above the SFMS are referred to as starburst galaxies, and galaxies below the SFMS are mainly quenched of star formation. The quenched galaxies may consequently become red and dead. The

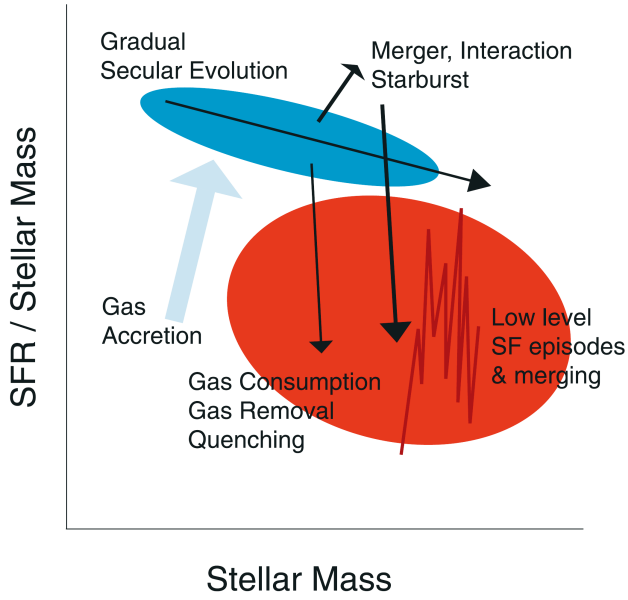

Figure 2.1: A schematic view of galaxy evolution in the stellar mass versus specific star formation rate diagram. The blue region shows the location of the star-forming main sequence. Galaxies move along the sequence and end up in the red region, which is dominated by quenched, dead galaxies with little or no star formation. Image credit: Figure 23 of Schiminovich et al. (2007).

evolution of galaxies along the picture given in Fig. 2.1 proceeds from top left toward the bottom right, as indicated by the arrows in the figure.

Another option for inferring the evolutionary state of a galaxy, which is less intuitive but more rooted in direct observations, would be the colour-magnitude diagram in which the galaxy's absolute magnitude is compared to its colour (defined as the difference between the apparent magnitudes observed in two different filters). In such a diagram the majority of galaxies reside either in the blue, low-luminosity region, or in the red, high-luminosity region, known as the blue and red clouds, respectively (Baldry et al., 2004). These regions correspond to the SFMS and to the low-SFR, high-stellar mass regions shown in Fig. 2.1. Between the bimodal distribution of the blue and red clouds lies the so-called green valley (Schawinski et al., 2014), which corresponds to galaxies transitioning between the star-forming and quenched regions. The non-equilibrium galaxies in the green valley are among the

most fascinating objects in the Universe due to their rare, and occasionally unique, observational properties.

In the following Chapters we will give an overview of the main evolutionary states of galaxies during their lifetimes, and review how we use numerical simulations to infer the past and future evolution of galaxies which we are only able to observe at one given epoch in time.

2.1 The star-forming main sequence

Similarly to the Hertzsprung–Russell diagram of stellar evolution, the SFMS tells a story of prolonged, steady-state evolution of star-forming galaxies. The SFMS in terms of the sSFR can be fitted with a power-law form

$$\mathrm{sSFR} = A\, M_*^{\alpha} \tag{2.2}$$

where α is the power-law index and A is a normalisation constant. The best-fit slope typically has values of the order of $\alpha \sim -0.3$ (between 0 and -1, e.g. Salim et al. 2007; Speagle et al. 2014). This almost flat relation holds over many orders of magnitude in stellar mass and is valid at least back to a redshift of $z \sim 6$, with some indications of a slight evolution toward a less negative slope as a function of increasing redshift (see Speagle et al. 2014 and references therein). At stellar masses below a few $10^{10}\,\mathrm{M}_\odot$, where the separation between star-forming galaxies and the red and dead galaxies is clear (as in the blue and red regions in Fig. 2.1), the sSFR – M_* relation is observed to be rather tight with only a few times 0.1 dex of scatter (Dutton et al., 2010). At larger masses, the scatter increases as more of the galaxies transition toward the quenched region.

Another simple relation, which connects the star formation rate to the gaseous star formation environment, is the Kennicutt-Schmidt relation (Schmidt, 1959; Kennicutt, 1998b). According to this relation the star formation rate surface density, Σ_{SFR}, and the gas surface density, Σ_{gas}, are related in star-forming galaxies by a power-law function of the form

$$\Sigma_{\mathrm{SFR}} = B\, \Sigma_{\mathrm{gas}}^{\beta} \tag{2.3}$$

where B is a normalisation factor, β is a power-law index typically between 1 and 2 (Bigiel et al., 2008), and Σ_{SFR} and Σ_{gas} are often expressed in units of $[\mathrm{M}_\odot\,\mathrm{yr}^{-1}\,\mathrm{kpc}^{-2}]$ and $[\mathrm{M}_\odot\,\mathrm{pc}^{-2}]$, respectively. Regions of interstellar gas at higher gas surface densities seem to form stars at higher SFR surface densities, which for

$\beta > 1$ would indicate a density dependent star formation efficiency (SFE, [yr^{-1}]),

$$\mathrm{SFE} = \frac{\Sigma_{\mathrm{SFR}}}{\Sigma_{\mathrm{gas}}} \tag{2.4}$$

at least when averaged over extended spatial regions (Daddi et al., 2010a). The expression above gives essentially the gas depletion time-scale as $\tau_{\mathrm{SF}} = \mathrm{SFE}^{-1}$, which is for star-forming galaxies typically of the order of a few Gyr (Leroy et al., 2008).

2.1.1 What regulates star formation?

Star formation across galaxies is regulated by a multitude of internal and external processes (Dekel & Birnboim, 2006). In star-forming galaxies, self-regulation from the star formation process itself is one of the main regulatory processes (Cole, 1991; Springel et al., 2005a). Young massive stars emit ionising photons, and release stellar winds and supernova feedback, all of which couple to the interstellar medium (ISM) heating the gas and thus reducing further star formation. Additionally, supermassive black holes and their accretion disks play a role in self-regulation (Kauffmann & Haehnelt, 2000; Springel et al., 2005a; Kormendy & Ho, 2013), as the potential energy of the infalling gas is converted into radiation (Shakura & Sunyaev, 1973). The dominant mode of self-regulation is theorised to be correlated with the mass of the galaxy; at the low-mass end of the stellar mass function, stellar feedback is thought to be the main driver of self-regulation, while the star formation in high-mass galaxies is thought to be regulated by the feedback from the central active galactic nuclei (AGN, see e.g. Ferrarese & Merritt 2000). In the extreme limit of the low-mass regime, the lowest mass dark matter haloes, which formed first at high redshifts, were not able to sustain almost any star formation. Their shallow gravitational potentials were unable to hold on to gas first heated due to the re-ionisation by the UV-radiation emitted by the first stars (Efstathiou, 1992) and then by the subsequent supernova explosions (Larson, 1974).

The internal regulation of star formation manifests itself in the galaxy stellar mass function, which cannot be described by a simple power-law, even though the SFR and stellar mass are clearly almost linearly correlated (Eq. 2.2). The galaxy mass function is often parametrised using the Schechter function Φ (Schechter, 1976) as

$$\Phi(M)dM = \Phi^* \left(\frac{M}{M^*}\right)^{\alpha} e^{-M/M^*} \frac{dM}{M^*} \tag{2.5}$$

where the stellar mass M^* (corresponding to the characteristic galaxy luminosity L^*) gives the transition between the exponential and the power-law parts, i.e. the

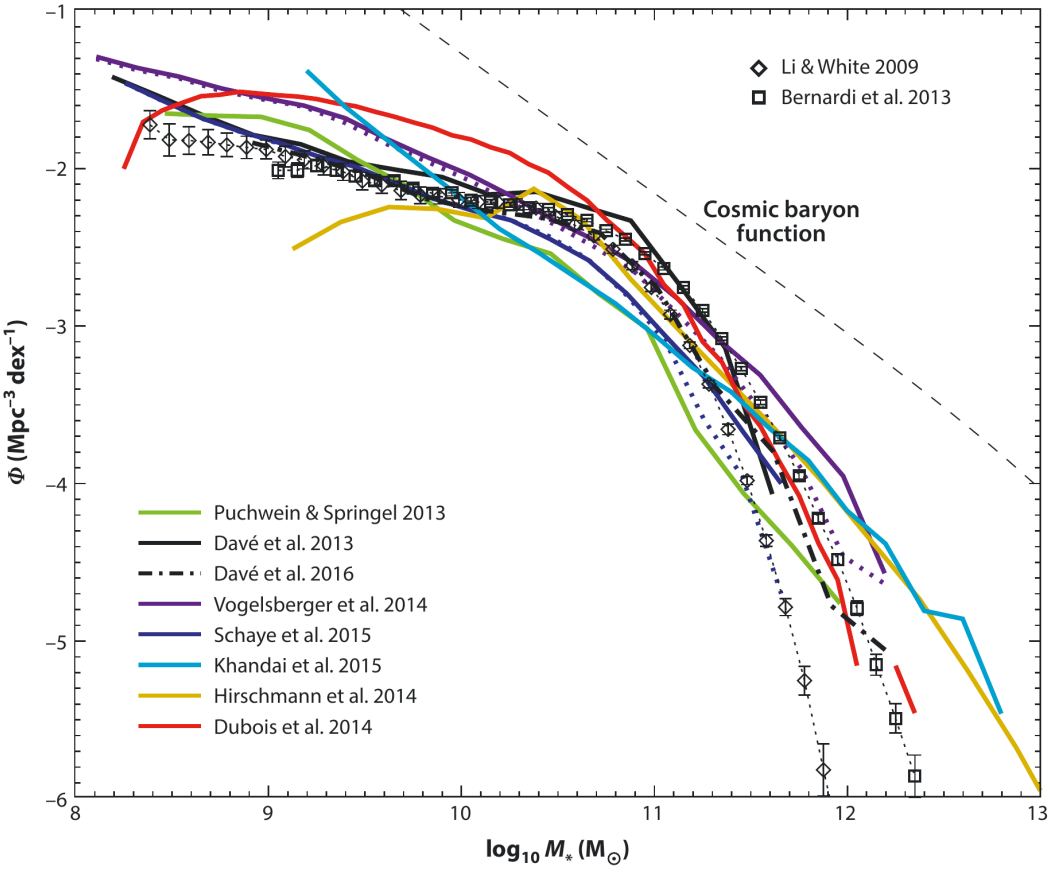

Figure 2.2: The $z = 0$ stellar mass function of observed (data points) and simulated (lines) galaxies. The simulated results are e.g. from the Eagle (Schaye et al., 2015), Illustris (Vogelsberger et al., 2014), Magneticum (Hirschmann et al., 2014) and the Horizon-AGN (Dubois et al., 2014) simulation projects. The dashed line shows what the stellar mass function would be assuming the universal cosmic baryon fraction of $\Omega_b/\Omega_m \sim 16\%$ (Planck Collaboration et al. 2016). Image credit: Figure 4 of Naab & Ostriker (2017).

knee, and Φ^* is the galaxy number density at M^* typically in units of [Mpc^{-3}]. A single Schechter function may underestimate the number density of the most massive galaxies, and this function is typically replaced with a sum of two or three Schechter functions (e.g. Li & White 2009).

Fig. 2.2 shows the observed galaxy stellar mass function, compared to results from cosmological simulations. The characteristic Schechter function shape is clearly demonstrated in the various data sets in Fig. 2.2. The shape of the mass function is regulated by feedback, predominantly by stellar feedback at the low-mass end and by AGN activity at the high-mass end. Consequently, star-forming galaxies populate the power-law part of the Schechter function while the red cloud spans the exponentially declining part of the mass function. The difference between the stellar mass function from what would be naively expected assuming the cosmic baryon fraction, $\Omega_b/\Omega_m \sim 16\%$, reveals that only a minor fraction of the baryonic mass in the Universe is actually locked in the stellar components of galaxies. Observations have in fact confirmed that the baryon content of the Universe is dominated by the hot gas in the intergalactic and intracluster medium (Fukugita et al., 1998).

Fig. 2.2 also demonstrates the variance in observed results and how the exact combination of the physical models incorporated in the simulations results in relatively small differences in the final outcome. Different simulation methodologies, for example the use of adaptive mesh refinement (Dubois et al., 2014) versus smoothed particle hydrodynamics (Schaye et al., 2015) in the hydrodynamical calculations, or including (Dubois et al., 2014) or excluding (Davé et al., 2013) explicit AGN feedback, all result in a reasonable fit to the observations as illustrated in Fig. 2.2, as long as some form of a physically motivated feedback process is included.

Another example of the feedback regulation is that galaxies at the low and high-mass ends of the galaxy stellar mass function have lower stellar to dark matter mass ratios, compared to Milky Way mass galaxies. Fig. 2.3 shows the stellar mass to halo mass relation of galaxies with respect to the mass of their dark matter haloes at redshift $z = 0.1$ collected in Behroozi et al. (2013). The figure includes the best-fit results from various techniques, where the observed galaxy mass function is connected to either a directly measured halo mass function (cluster catalogues, CL), or to a halo mass function derived from cosmological dark matter only simulations (abundance matching, AM; halo occupation distribution modelling, HOD; conditional luminosity function modelling, CLF). All the results consistently show how the haloes at around $M_{\rm DM} \sim 10^{12}\,{\rm M}_\odot$, corresponding to $M_* \sim 3 \times 10^{10}\,{\rm M}_\odot$, are the most efficient in forming stars and retaining their baryons. The transition from star-forming to mostly quenched galaxies appears at around this mass, which also corresponds to M^*, i.e. the knee of the Schechter mass function.

As illustrated in Figures 2.2 and 2.3, galaxies on the SFMS, corresponding to stellar masses below $10^{10.5} \sim 3 \times 10^{10}\,{\rm M}_\odot$, are also the most numerous. These star-forming galaxies have stellar masses that are typical for low-mass disk and dwarf galaxies (Kennicutt, 1998a).

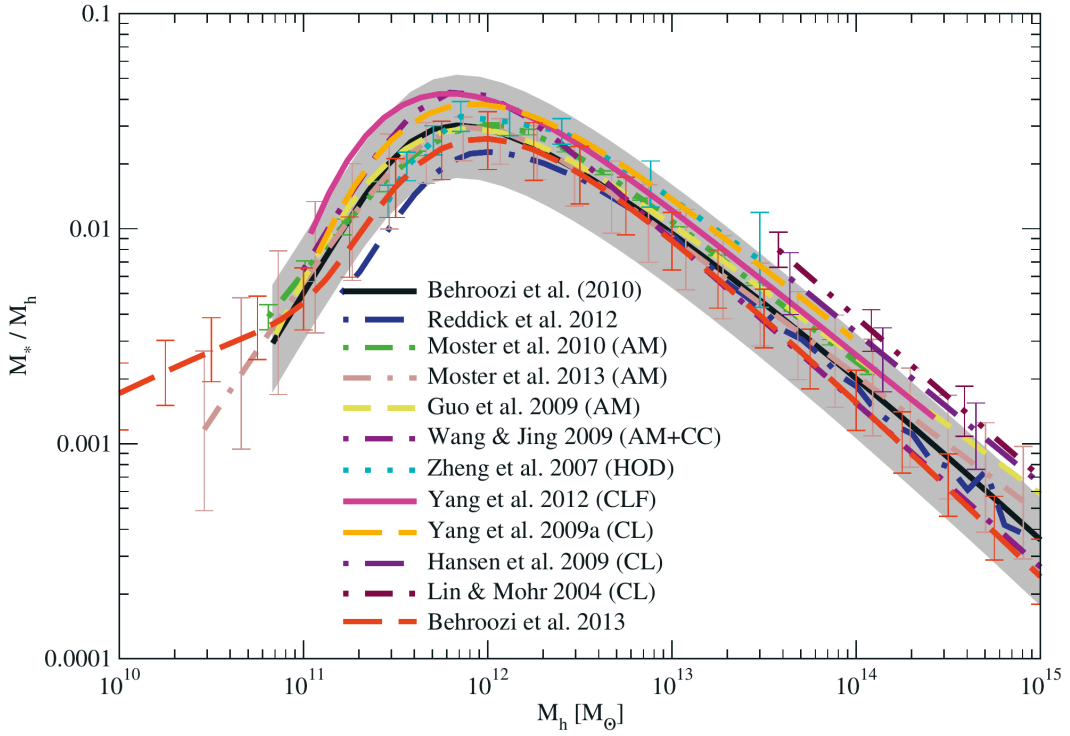

Figure 2.3: Some best-fit results for the stellar mass to halo mass relation (M_*/M_h) of galaxies as a function of the dark matter halo mass M_h. Image credit: Figure 14 of Behroozi et al. (2013).

2.1.2 Disk galaxies

Rotationally supported disk galaxies are the most archetypal galaxies, of which our own Milky Way is a prime example. The spiral arm structures, dust lanes and central bars seen typically in face-on projection are organised in a vertically thin structure which, when viewed edge-on, looks like a razor sharp disk. Our location within the Milky Way's disk has made it possible to study many of its matter components in great detail, in spite of the obscuring dust in the immediate vicinity of the mid-plane. Modelling the structure of disk galaxies from first principles has, however, proven to be very tricky due to the highly complex feedback processes present at various different astrophysical scales (Naab & Ostriker, 2017).

The total mass budget of all galaxies is dominated by the dark matter halo,

which in the case of disk galaxies, constitutes typically 95–99% of the total mass within the virial radius (Mo et al., 1998; Behroozi et al., 2013). Disk galaxies are characterised by the disk component, which consists usually of a stellar disk and an accompanying gaseous, star-forming disk. In the present-day Universe the gas fraction in disk galaxies is typically $\sim$ 10–20%, while at higher redshifts the gas disk was the dominant disk component, with e.g. more than 50% of the disk mass in gas at a redshift of $z \sim 1.5$ (Daddi et al., 2010b; Carilli & Walter, 2013). Disk galaxies are known to form their stellar structure inside-out (Boissier & Prantzos, 1999), and their sizes (half-mass radii) increase toward the present-day (Wuyts et al., 2011). Additionally, the central regions of disk galaxies often harbour a stellar bulge (Simien & de Vaucouleurs, 1986), while an extended, old low luminosity stellar halo is typically observed surrounding the plane of the disk (e.g. Sackett et al. 1994; Ibata et al. 2007). The bulge and the stellar halo are typically the oldest stellar components, and were formed during the first few Gyr of the cosmic timeline. As the gas contracted and cooled down, in order to conserve angular momentum, a disk component formed in the plane of rotation set by tidal torques exerted by other nearby dark matter structures (Mo et al., 1998).

The stellar disk

The detailed structures of the different matter components have been inferred from both observations and simulations. Observationally, the luminous components are typically described in terms of a surface brightness $I(R)$ (in mag arcsec^{-2}) or a surface mass density $\Sigma(R)$ (in $\mathrm{M}_\odot\,\mathrm{pc}^{-2}$) profile, which can be used to constrain the models of the three-dimensional structure derived from simulations. The total surface brightness profile $I(R, z)$ of most disks can be described with an exponential function in the radial direction (Freeman, 1970), coupled with a hyperbolic secant function along the vertical axis as

$$I(R, z) = I_{0,0} e^{-R/h_d} \operatorname{sech}^{2/n}(z/z_d) \tag{2.6}$$

where $I_{0,0}$ is the central brightness, h_d is the scale radius (or scale length), z_d is the characteristic thickness (scale height), and n sets the vertical shape with typical values of $n > 1$. The vertical distribution may be slightly more peaked than a simple sech-distribution (where $n = 2$), with for example $n \sim 4$ (de Grijs et al., 1997), and the value of z_d is typically significantly smaller than the horizontal size with $h_d/z_d \sim 5$ due to the disk rotation (van der Kruit & Searle, 1981). The value of z_d is also relatively constant as a function of radius. Some disk galaxies, such as Milky Way, have two disk components, referred to as the thin and the thick disk

(e.g. Bensby et al. 2003). The thick component is present as excess light when the traditional single disk is removed from the light profile. The two disk components may have differing elemental abundances and formation histories, and the thick disk may even be the result of a merger event (Read et al., 2008).

The interstellar medium

The interstellar medium of disk galaxies is mainly found in the star-forming gaseous disk, and the hot gaseous halo. The gas disk is, by volume, mostly dominated by hot, supernova-heated gas with a volume filling factor (fraction of the total ISM volume) of $f_{\rm hot} \sim 30$–90% (e.g. McKee & Ostriker 1977). The remainder of the ISM volume consists of gas at lower temperatures, with the cold, clumpy molecular phase constituting only a tiny fraction, $f_{\rm mol} < 1\%$. The gas disk is vertically thin, with its scale height typically smaller than the scale height of the stellar disk. For example, the Milky Way has a neutral gas disk scale height of ~ 100 pc (Marshall et al., 2006), versus the stellar disk scale heights of the order of 300 pc for the thin disk and more than 1000 pc for the thick disk (e.g. Gilmore & Reid 1983 and Carollo et al. 2010).

The gaseous disk and halo are coupled through a cycle of feedback and cooling, which results in a fountain-like exchange of matter between the two (Sancisi et al., 2008; Putman et al., 2012). Infalling gas from the hot halo and accretion through minor mergers replenish the gas disk, enabling the prolonged, stable star formation when coupled with the self-regulation discussed in Section 2.1.1.

The dark matter halo

The dark matter halo is the most difficult component to study, as it can only be observed through its gravitational effects, for example, using the galactic rotation curves and motions of satellite galaxies in galaxy clusters. Any observations of the dark matter structure are therefore indirect, and subject to biases in fitting e.g. the disk components especially in the inner galaxy. Based on cosmological simulations and observations of galaxies, it is known that the gravitational potential of dark matter is necessary both for the formation and the stability of the rotationally supported population of galaxies we observe today (White & Rees, 1978; Rubin et al., 1978; Mo et al., 1998).

From cosmological simulations, we know that dark matter haloes tend to follow a power-law density profile, with a shape of the order of $\rho(r) \propto r^{-3}$ in the outer parts of galaxies. Typical, purely empirical, parametrisations for the density profile

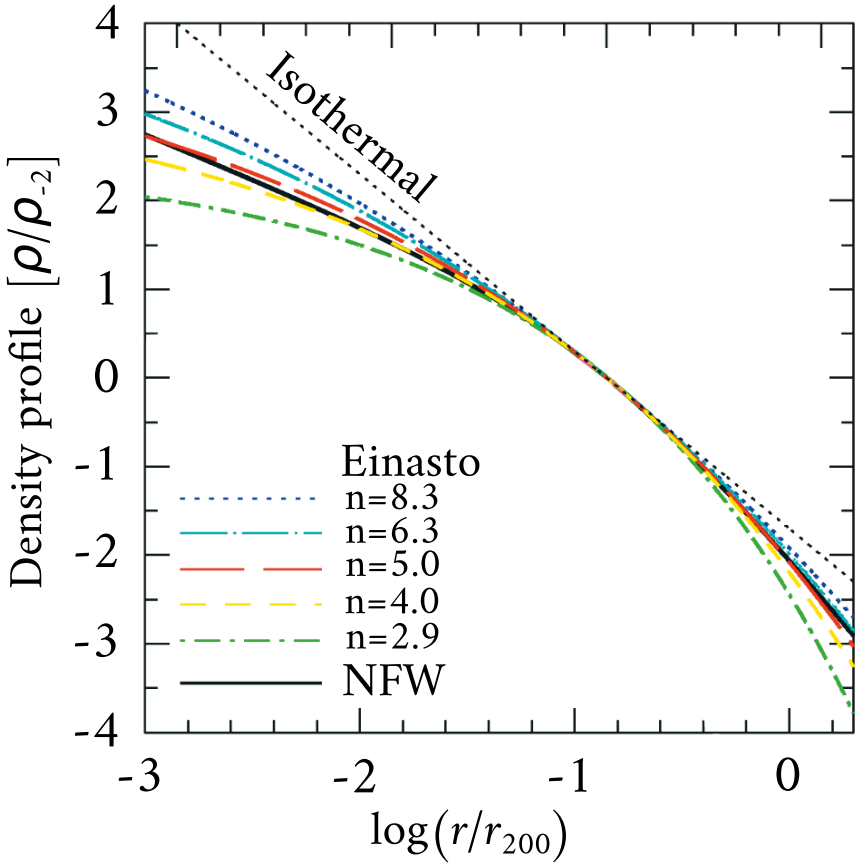

Figure 2.4: The NFW density profile (Eq. 2.7) and a few Einasto profiles (Eq. 2.8) for five values of n, compared with the isothermal density profile with a power-law slope of -2. The profiles have been normalised with the density at a radius where the slope of each of the profiles is -2. Image credit: adapted from Figure 2 of Dutton & Macciò (2014).

include the Navarro-Frenk-White (NFW) profile (Navarro et al., 1996) of the form

$$\rho(r) = \frac{\rho_0}{\frac{r}{r_s}\left(1+\frac{r}{r_s}\right)^2} \tag{2.7}$$

and the Einasto profile (Einasto, 1965) of the form

$$\rho(r) = \rho_0 \exp\left[-\left(\frac{r}{r_s}\right)^{1/n}\right], \tag{2.8}$$

where ρ_0 is the central density and r_s is the scale radius, defined as the radius where the density subceeds $\rho_0/2$ and ρ_0/e in the NFW and Einasto profiles, respectively. The Einasto index, n, has typical values in the range of $4 < n < 8$ (Navarro et al., 2004; Springel et al., 2005b).

The shape of the NFW and Einasto profiles can be characterised with a concentration parameter, $c = r_{200}/r_s$. Here r_{200} is defined as the radius at which the density profiles drop below 200 times the cosmic critical density (matter density of a flat Universe without a cosmological constant), which at $z = 0$ is of the order of $10^{-26}\,\mathrm{kg\,m^{-3}}$. Fig. 2.4 shows a comparison of the NFW and Einasto profiles at a few values of n, compared with a purely isothermal density profile of $\rho \propto r^{-2}$. The dark matter profiles differ from the isothermal profile in that their densities have a steeper decline at large radii and a more cored inner structure.

The total mass profile

Fig. 2.5 shows the decomposition of the rotation curve $V(R)$ of the Milky Way, which illustrates the total cumulative mass profile $M(< R)$ through

$$V(R) = \sqrt{\frac{GM(< R)}{R}}. \tag{2.9}$$

The baryonic components are shown separately, and the contribution from the dark matter halo is clearly visible in the constant velocity curve at larger radii. The bulge dominates the mass profile in the inner galaxy, the intermediate radii are dominated by the combined effect of the bulge and the disk, and the outer radii from 20 kpc or so are dominated by the dark matter halo. The oscillating nature of the disk profile represents the spiral arms which are added onto the exponential disk as perturbations.

2.1.3 Dwarf galaxies

As shown in Fig. 2.2, low-mass galaxies are the most numerous galaxies in the Universe. Galaxies at the low-mass end of the stellar mass function are collectively referred to as dwarf galaxies and encompass a plethora of subclasses, which are morphologically mostly low-mass extensions of the elliptical (dwarf ellipticals, dE)

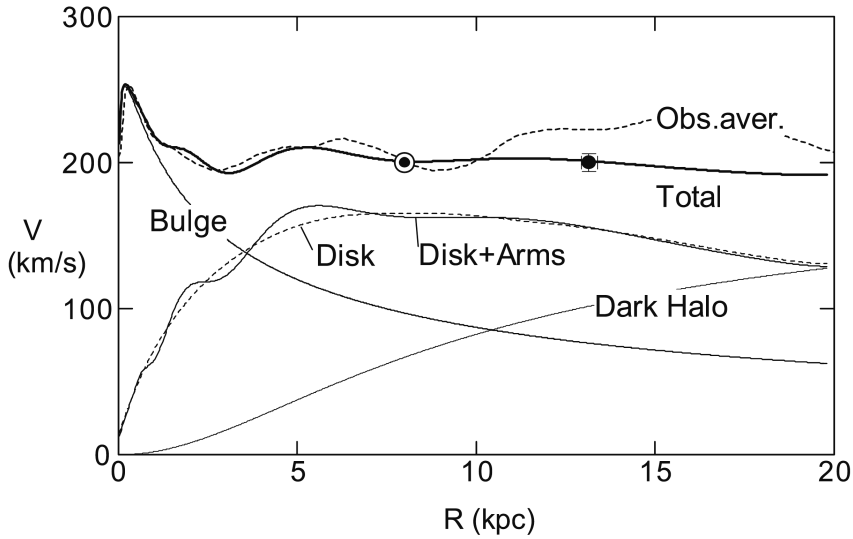

Figure 2.5: The averaged measurements of the observed rotation curve of the Milky Way, compared with a mass model composed of a de Vaucouleurs-type bulge, an exponential disk, and a semi-isothermal dark halo. The point at $R = 8$ kpc indicates the value of 200 km s^{-1} at the Solar radius, and the large circle with errorbars at $r = 13.1$ kpc shows a best-fit value based on a VLBI-measurement of a water maser (Honma et al., 2007). Image credit: Figure 3 of Sofue et al. (2009).

and spiral (dS) galaxy types (Sandage & Binggeli, 1984). Additionally, dwarf galaxies include the irregular galaxies (Im) and compact dwarfs, divided into ultra compact dwarfs (UCD) and blue compact dwarfs (BCD), which are found with bright clumps of stars (Haşegan et al., 2005; Chiboucas et al., 2011). In the context of the SFMS, the vast majority of dwarf galaxies are star-forming (Geha et al., 2012).

In addition to the low (stellar) masses, dwarf galaxies are characterised by small sizes (Barazza et al., 2006), low metallicities (Grebel, 2000), and larger gas fractions compared to higher mass galaxies. The range of baryon mass fractions in dwarfs are also significantly broader than for more massive galaxies. The extreme ends extend from dwarfs where even the inner regions are dominated by dark matter (Oh et al., 2011) to dwarfs where the baryon fraction within the virial radius may be up to 30% (Guo et al., 2019).

The wide variety of characteristics and the ubiquity of dwarf galaxies make them ideal for probing the conditions that were present in the early Universe.

Observational surveys (e.g. Stierwalt et al. 2015; Paudel et al. 2018) and simulation work (e.g. Emerick et al. 2019; Lahén et al. 2019) concentrating on star formation in isolated, merging and interacting dwarf galaxies can therefore be used to constrain models of high-redshift star formation.

2.2 Starburst galaxies then-and-now

The transition from the SFMS to the red cloud can either take place through a slow depletion of the gas reservoir through main sequence star formation (Noeske et al., 2007), or more rapidly due to some energetic event which either depletes, expels or strips the gas reservoir available for star formation. The class of starburst galaxies includes a wide range of star-forming galaxies with short, bursty periods of elevated star formation with temporary or permanent transformations in their global properties. The ultimate fate of all galaxies is to move toward the quenched red cloud, but during their lifetimes they may venture to and from the SFMS multiple times.

The term *starburst* is somewhat vague, as the specific astrophysical phenomenon which causes a galaxy to appear as a starburst may be anything from a single star-forming cloud to a major galaxy merger. The most direct definition is through the spectral energy distribution (SED) of a galaxy, which for ongoing starbursts is characterised with an excess amount of energy from young, hot stars indicative of recent star formation. Quantitatively, a common definition is to define galaxies with a sSFR twice that of the respective (current) value given by the star-forming main sequence (Eq. 2.2) as starbursts. Obtaining the absolute star formation rate from observations is, however, not straightforward. Detailed models of the SEDs of evolving stars, as well as the stellar populations and any intervening obscuration effects, must be used in converting from the SED to the absolute star formation rate.

(Ultra)luminous infrared galaxies, (U)LIRGS, are typical starburst galaxies in the present-day Universe, although not all starbursts exceed the luminosity threshold of being considered as bona fide LIRGs. The infrared luminosities in the wavelength range of $[8, 1000]\,\mu$m span $10^{11}\,\mathrm{L}_\odot \leqslant L_{8-1000\,\mu\mathrm{m}} \leqslant 10^{12}\,\mathrm{L}_\odot$ in LIRGs and $L_{8-1000\,\mu\mathrm{m}} > 10^{12}\,\mathrm{L}_\odot$ in ULIRGS. These luminosities need to be fuelled by some energetic, dust obscured phenomenon such as star formation and/or a central active galactic nucleus (e.g. Sanders & Mirabel 1996 and Howell et al. 2010). The energetic, gas-rich starburst galaxies provide a present-day analogue to the star and galaxy formation conditions prevalent in the early Universe at and beyond redshifts of $z \sim 1$–2.

2.2.1 Interacting galaxies

Interactions between galaxies are common, and the type of interaction correlates with both the galaxy mass and the environment. In galaxy clusters, the relative velocities between galaxies are high due to the high velocity dispersion, and most of the galactic interactions are high-speed long-distance encounters (Moore et al., 1998). Galaxy groups on the other hand contain typically only a few massive galaxies along with tens of times more abundant dwarf galaxies. Galactic interactions in a group environment typically end in (minor) mergers.

When galaxies interact, the gas within them gets compressed due to tidal torques, ram pressure and shocks (Mihos & Hernquist, 1996; Renaud et al., 2008). The tidal forces also drive gas inflows to the central regions of the interacting galaxies (Barnes & Hernquist, 1996; Di Matteo et al., 2007). As the density of interstellar gas increases, be it in the tidal bridge between the interacting galaxies or in the central nuclear region, the cooling rate of the gas increases as $\propto \rho^2$ leading to an elevated rate of star formation. The strongest starbursts occur in co-planar mergers of roughly equal mass galaxies, where the SFR can increase by orders of magnitude and completely exhaust the gas in the remnant.

Galaxies form hierarchically from smaller structures, implying that mergers and interactions of galaxies must have been much more common in the past. Candidates of galaxies undergoing mergers can be identified in observations visually (without detailed spectral analysis) for example by their shape asymmetry, clumpiness, and the concentration of the surface brightness distribution. Based on observational surveys, some 5–20% of galaxies with stellar masses in the range $10^8\,\mathrm{M}_\odot \lesssim M_* \lesssim 10^{9.5}\,\mathrm{M}_\odot$ undergo major mergers (mass ratio in the range [1:1, 1:3]) at low redshifts $0 \lesssim z \lesssim 1$ (e.g. Patton et al. 1997 and Conselice et al. 2003). The merger fraction peaks for most galaxies in this mass range between redshifts $0 \lesssim z \lesssim 1$, which corresponds to the epoch when roughly half of the cosmic stellar mass forms (Behroozi et al., 2013; Madau & Dickinson, 2014). Higher-mass galaxies, on the other hand, with $M_* > 10^{10}\,\mathrm{M}_\odot$ have the highest merger fractions of up to 50% toward redshift $z \sim 3$, while their merger fraction is only a few percent in the present-day Universe. When the most massive galaxies, which today are mostly gas-depleted, undergo major mergers, their inability to form stars actually leaves them below the SFMS. Thus, not all mergers cause starbursts (Di Matteo et al., 2007).

2.2.2 The early Universe

The cosmic star formation rate was an order of magnitude higher at redshift $z \sim 2$ than it is today (Behroozi et al., 2013), which poses further problems for the definition

of a starburst. The cosmic time between $z \sim 0-2$, which encompasses the majority of the cosmic timeline, consequently includes the majority of the cosmic star formation (Madau & Dickinson, 2014). As the SFR and sSFR in galaxies increase as a function of higher gas fractions toward higher redshifts, the definition of the SFMS also shifts upwards. As a result, high-redshift galaxies in the (U)LIRG regime defined using absolute, rather than relative, luminosities, become normal SFMS galaxies. Fig. 2.6 shows the sSFR as a function of redshift, where the increase of the starburst-threshold of $2 \times$ mean(sSFR) with redshift is demonstrated. The median sSFR of star-forming galaxies increases from redshift $z = 0$ to $z = 2.5$ by more than an order of magnitude.

2.2.3 The aftermath: Post-starburst galaxies

Just as a starburst galaxy is characterised through excess star formation, the shut down of star formation is also imprinted in the SED of such galaxies. Post-starburst galaxies (PSBs) are identified based on their SED features, which include strong Balmer absorption lines due to the dominating population of A-type stars. A-type stars have typical lifetimes of 1 Gyr, which means PSBs are easily identifiable for a few 100 Myr after the star formation shuts down. Additionally, the hydrogen emission lines from HII regions, indicative of short lived O and B stars, can be used to exclude galaxies with any significant levels of ongoing star formation.

The main feature for a galaxy to be classified as post-starburst requires the star formation to be shut down relatively rapidly, because longer time-scales dilute the starburst indicators from the SED. The stronger the process which quenched the SF, the easier the galaxy can be detected as a PSB. The environmental dependence of the typical PSB features, as discussed in the context of starbursts in the previous Section, is also observed in the post-starburst population (Poggianti et al., 2009). The merger origin of starbursts in group environments leads to strong quenching, as the star-forming galaxy transforms into a dead elliptical merger remnant. In a cluster environment, on the other hand, slow quenching processes such as ram pressure stripping and strangulation may remove gas which would act as fuel for star formation. PSB galaxies tend to be dominated by low to intermediate mass galaxies ($M_* < 10^{11}\,\mathrm{M}_\odot$, Wild et al. 2016) at low redshifts of $z < 1$, while intermediate to massive galaxies ($M_* > 10^{10}\,\mathrm{M}_\odot$, Maltby et al. 2018) dominate the PSB population at higher redshifts.

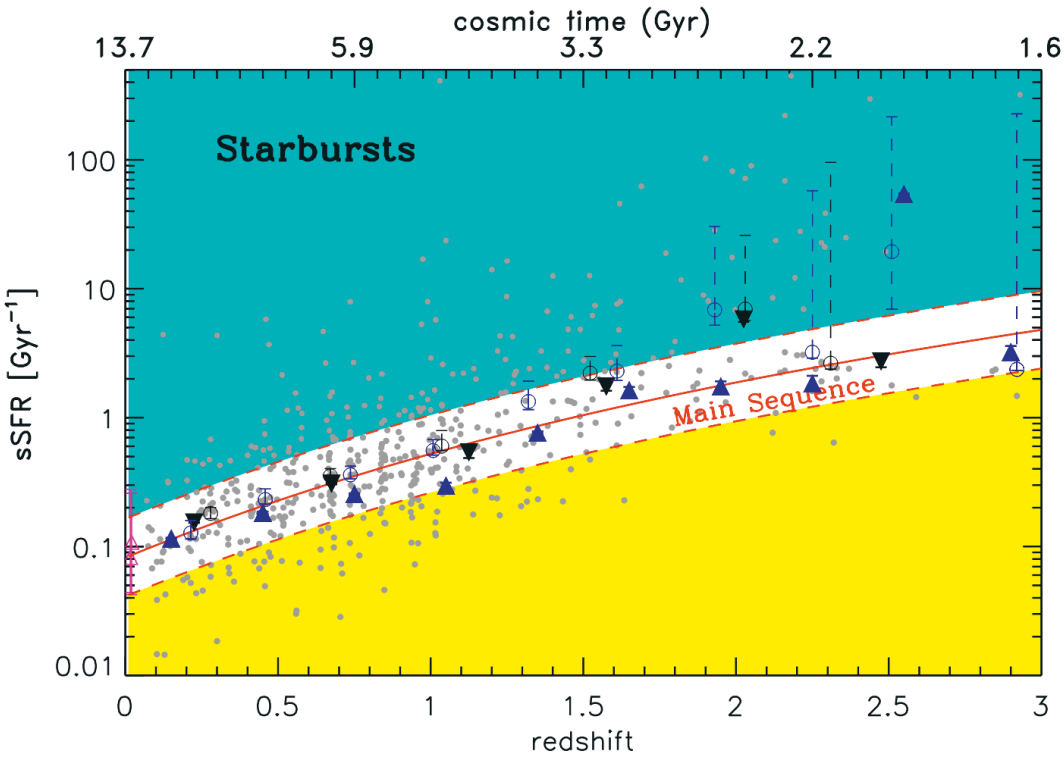

Figure 2.6: The sSFR of star-forming galaxies as a function of redshift. The grey points show individual measurements in the Great Observatories Origins Deep Survey (GOODS) taken with the Herschel Space Observatory (Pilbratt et al., 2010), the open circles show redshift-binned median values, and the triangles show the binned values but with undetected sources stacked. The black and blue symbols indicate values in the southern and northern hemispheres, respectively. The red line shows a SFMS fit of the form sSFR$\propto t^{-2.2}$, and the dashed red lines show values twice and half of the fit SFMS, which separate the SFMS galaxies from starbursts and low-sSFR galaxies. Image credit: Figure 18 of Elbaz et al. (2011).

2.3 Early-type galaxies: Red and dead

The red cloud spans the largest range of galaxy masses in the observed present-day Universe. The high-mass end of the galaxy mass function is dominated by early-type galaxies, which include elliptical galaxies and S0 galaxies. Deep, high-

resolution imaging have revealed disk structures, gas, and very complex stellar orbital structures, as well as black hole activity within the general population of early-type galaxies. These galaxies are predominantly found in the crowded environment of galaxy clusters (Dressler, 1980), where the centres of the clusters are populated by the most extreme objects named brightest cluster galaxies (Lin & Mohr, 2004). Galaxies in clusters tend to be quenched due to external processes, such as ram-pressure stripping (Bekki, 2009) or strangulation, which remove the cool disk gas and the hot halo gas required to fuel star formation.

Statistically, galaxies at the massive end of the galaxy mass function tend to fall on a fundamental plane in the parameter space, set by three directly observable parameters: the effective (or half-light) radius R_e, the stellar velocity dispersion σ_e measured within R_e, and the surface brightness I_e measured within R_e (e.g. Cappellari et al. 2006; Kormendy et al. 2009).

2.3.1 Surface brightness profiles of elliptical galaxies

Other correlated parameters arise from the analysis of the two-dimensional light profiles of elliptical galaxies. The isophotes in a projected image of an elliptical galaxy can be fit with concentric ellipses (using e.g. Fourier series) to high accuracy, though some galaxies deviate from the simple ellipses at a level of a few per cent (Bender et al., 1988). As illustrated in Fig. 2.7, depending on whether the deviation is characterised as extra-light in the direction of the major and minor axes, or in the "corners" of the ellipse, the galaxies are divided into disky and boxy ellipticals (Lauer, 1985; Bender & Moellenhoff, 1987), respectively. The oldest, more massive ellipticals tend to have boxy isophotes, while the somewhat younger, less massive ellipticals show more disky shapes reminiscent of S0 galaxies (Davies & Illingworth, 1983; Bender et al., 1994).

Averaging the two-dimensional map over the angular extent gives a radial profile, which can be fit with the Sérsic function (Sérsic, 1963)

$$I(r) = I_e \exp\left\{ b_n \left[\left(\frac{r}{R_e} \right)^{1/n} - 1 \right] \right\}, \tag{2.10}$$

where n is the Sérsic index which sets the power-law shape and b_n is a constant which depends on n (see e.g. Capaccioli 1989).

In Fig. 2.8 we illustrate the dependence of the surface brightness profile on the Sérsic index when the other parameters are kept fixed. Lower values of n give a more cored profile with a sharp drop in light at larger radii, while higher values of n have cuspy shapes with long wings toward large radii. The profile described by $n = 4$ is

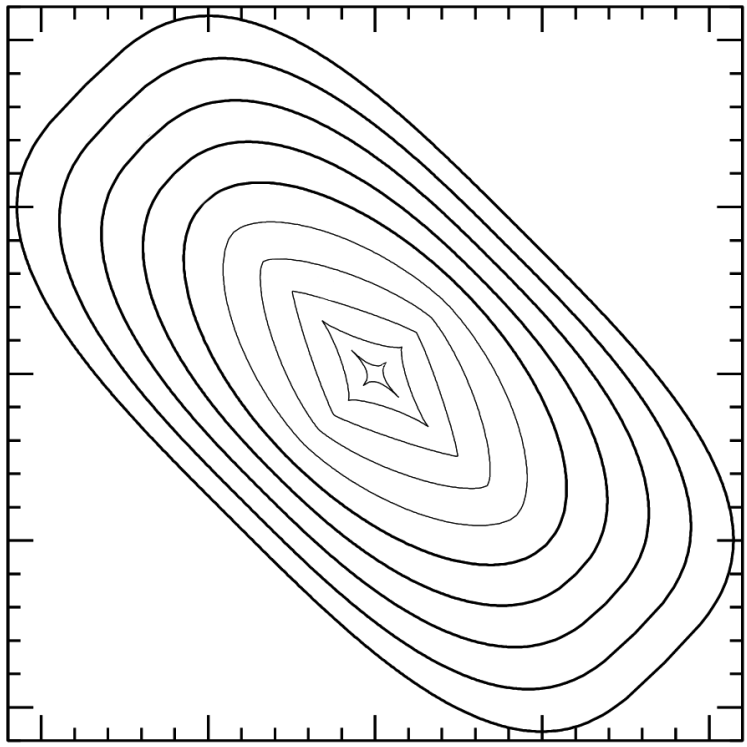

Figure 2.7: An illustration of the deviations from a pure elliptical shape. The inner and outer curves represent the disky and boxy shapes, respectively, while the 6th curve from the centre is a simple ellipse. Image credit: adapted from Figure 2 of Peng et al. (2002).

the traditional de Vaucouleurs profile (de Vaucouleurs, 1948). High-mass ellipticals are typically fit especially in the outer radii with a Sérsic index of $n \gtrsim 4$, while lower mass ellipticals agree better with lower values of n. For a disk galaxy, the Sérsic index would be of the order of $n \sim 1$ corresponding to the traditional exponential profile (as in Eq. 2.6), hence also the connection to disky isophotal shapes.

The innermost central regions of massive ellipticals are however not typically cuspy, as depicted by the high-n curves in Fig. 2.8, but rather strongly cored (Kormendy & Ho, 2013). The formation of the cored light profiles has been hypothesised to happen due to supermassive black hole binaries which vacate the central regions of massive elliptical galaxies through three-body interactions with

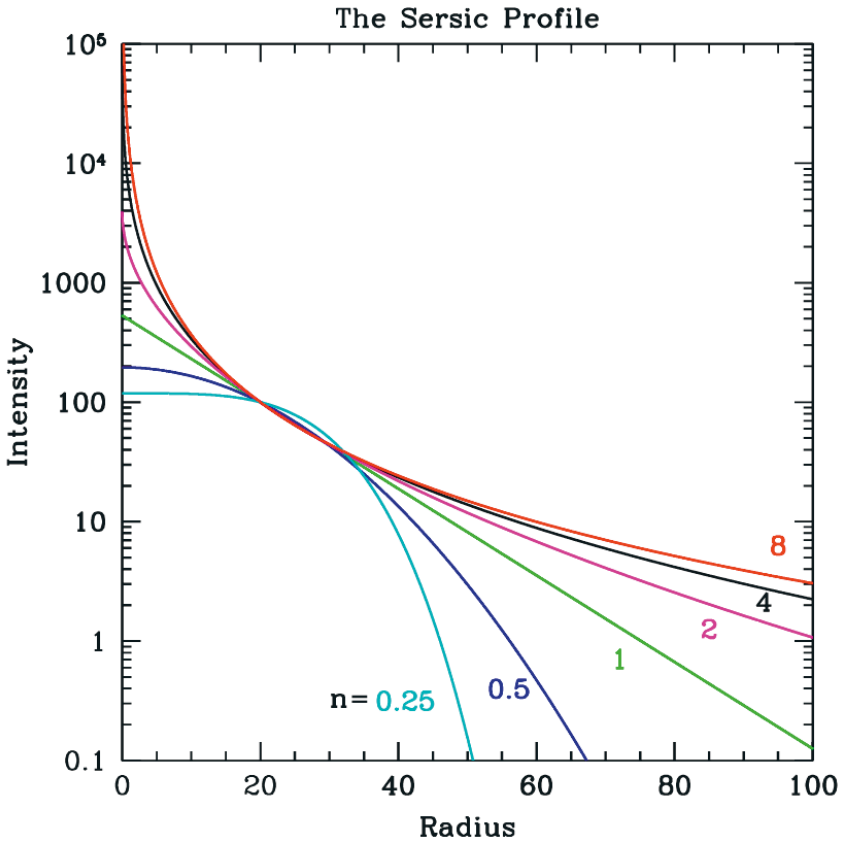

Figure 2.8: The effect of the Sérsic index n on the radial surface brightness profile when the normalisation and the effective radius are fixed. Image credit: Figure 3 of Peng et al. (2010).

stars (Kormendy et al., 2009). In massive ellipticals, the surface brightness profiles are better fit with a core-Sérsic profile (Trujillo et al., 2004), where the outer radii are described by a Sérsic profile while the inner radii follow a power-law function.

2.3.2 Kinematic properties

The development of integral field unit spectrographs (IFU) for observational surveys has revolutionised the study of resolved galactic dynamics in external galaxies. Instead of a single or a few spectra per galaxy, the use of IFUs enables taking a

spectrum for each pixel in the field of view. This results in resolved velocity data across a galaxy rather than a single recession velocity or the general direction of rotation. The derived velocity information can then be used to make connections between the dynamical properties and the formation histories of galaxies.

The velocity information is observed along the line-of-sight (LOS), in projection, where the phase-space density $f(\bar{\mathbf{x}}, \bar{\mathbf{v}})$ is compressed along the LOS to only a function of two coordinates (the position of a pixel) and the velocity along the line-of-sight, v_z. The spectrum in each pixel at position (x, y) encodes the line-of-sight velocity distribution (LOSVD)

$$\mathcal{D}(v_z, x, y) = \int \mathrm{d}z \int\int \mathrm{d}v_x \mathrm{d}v_y f(\bar{\mathbf{x}}, \bar{\mathbf{v}}) \tag{2.11}$$

of all emitting matter in a given pixel. The LOSVD can in turn be utilised to obtain the characteristic LOS parameters on a pixel-by-pixel basis, as the first few moments of Eq. 2.11 over v_z give the traditional observables used to describe the velocity properties of galaxies. The zeroth, first and second moments provide the surface brightness distribution I, the mean velocity V_{LOS}, and the velocity dispersion σ_V as

$$\begin{aligned} I(x, y) &= \int \mathcal{D}(v_z, x, y) \mathrm{d}v_z \\ V_{\mathrm{LOS}}(x, y) &= \int v_z \mathcal{D}(v_z, x, y) \mathrm{d}v_z \\ \sigma_V^2(x, y) &= \int v_z^2 \mathcal{D}(v_z, x, y) \mathrm{d}v_z, \end{aligned} \tag{2.12}$$

respectively (Gerhard, 1993). Expanding from this, the Gauss-Hermite coefficients h_3 and h_4 are commonly used to describe the higher-order deviations from a Gaussian (van der Marel & Franx, 1993). The h_3 and h_4 parameters resemble the kurtosis and skewness; the positive or negative values of h_3 describe a distribution with a peak value shifted toward left or right along the horizontal axis, and positive or negative values of h_4 describe a centrally peaked or a flat-topped distribution. The IFU data can be noisy especially in the outer regions of galaxies, and a common procedure for extracting the velocity data is to bin the pixel-by-pixel data into, for example, constant signal-to-noise bins using a Voronoi-tessellation method (Cappellari & Copin, 2003).

The result of the IFU-based LOSVD fitting is a two-dimensional map of pixel-averaged velocity properties for each galaxy, which sometimes show peculiar features such as decoupled core components and multiple peaks in the velocity dispersion. For asymmetric profiles, the anticorrelation between h_3 and $V_{\mathrm{LOS}}/\sigma_V$ can for example

indicate the leading and trailing sides of an embedded disk structure (Bender et al., 1994; Krajnović et al., 2008). A similar analysis can be performed with simulated galaxies as for example in Naab et al. (2014), where the past evolution of the galaxies formed in a cosmological simulation were used to infer the formation or recent evolution of the observed galaxies in the ATLAS^{3D} survey of nearby early-type galaxies (Cappellari et al., 2011). Publicly available methods for fitting the LOSVD from IFU data include for example the KINEMETRY code package by Krajnović et al. (2006).

In addition to the LOSVD maps, the radial dimensionless angular momentum parameter λ_R is a typical parameter used to characterise the global rotation of early-type galaxies (Emsellem et al., 2007, 2011). The radial λ_R parameter is defined as

$$\lambda_R = \frac{\sum_{i=1}^{N} F_i R_i |V_{\mathrm{LOS},i}|}{\sum_{i=1}^{N} F_i R_i \sqrt{V_{\mathrm{LOS},i}^2 + \sigma_{V,i}^2}} \tag{2.13}$$

where F_i is the flux in a given pixel, R_i is the radial distance of the pixel, and the sum goes over for example all N Voronoi-cells within a certain radius. The λ_R is often measured within the effective radius R_e as λ_{Re}, and compared to the value of R_e, ellipticity, or stellar mass.

Fast and slow-rotating elliptical galaxies can be identified in the λ_{Re} versus ellipticity plane, with the distinction being more difficult toward lower ellipticities due to the coupling of the inclination and galaxy shape. Fig. 2.9 shows the effective λ_{Re} as a function of the apparent ellipticity ϵ_e at the effective radius. The data points have been coded by the total stellar mass (top) and their rotation properties (bottom). The bottom panel shows the recently introduced division between slow and fast rotators of $\lambda_{Re} = 0.31\sqrt{\epsilon_e}$ (green line, Emsellem et al. 2011) which replaces the previously often used definition of $\lambda_{Re} = 0.1$ (e.g. Emsellem et al. 2007 and Cappellari et al. 2007). The magenta line in both panels shows a typical lower limit for observed fast-rotating galaxies, which corresponds to a linear connection between the velocity anisotropy and ellipticity when the galaxies are viewed edge-on. The dashed black lines show the λ_{Re} values for galaxies with a certain ellipticity ($\epsilon = [0.85, 0.75, 0.55, 0.45, 0.35]$ from top to bottom) but with varying the viewing angle (inclination changing from edge-on to face-on with decreasing λ_{Re}, see e.g. Cappellari et al. 2007).

The highest-mass galaxies tend to reside in the lowest angular momentum regime, while lower mass galaxies occupy a wide range in the parameter space. The low angular momentum galaxies also include most of the peculiar rotational features. These properties tell a tale of their recent evolution, as major mergers are one of the

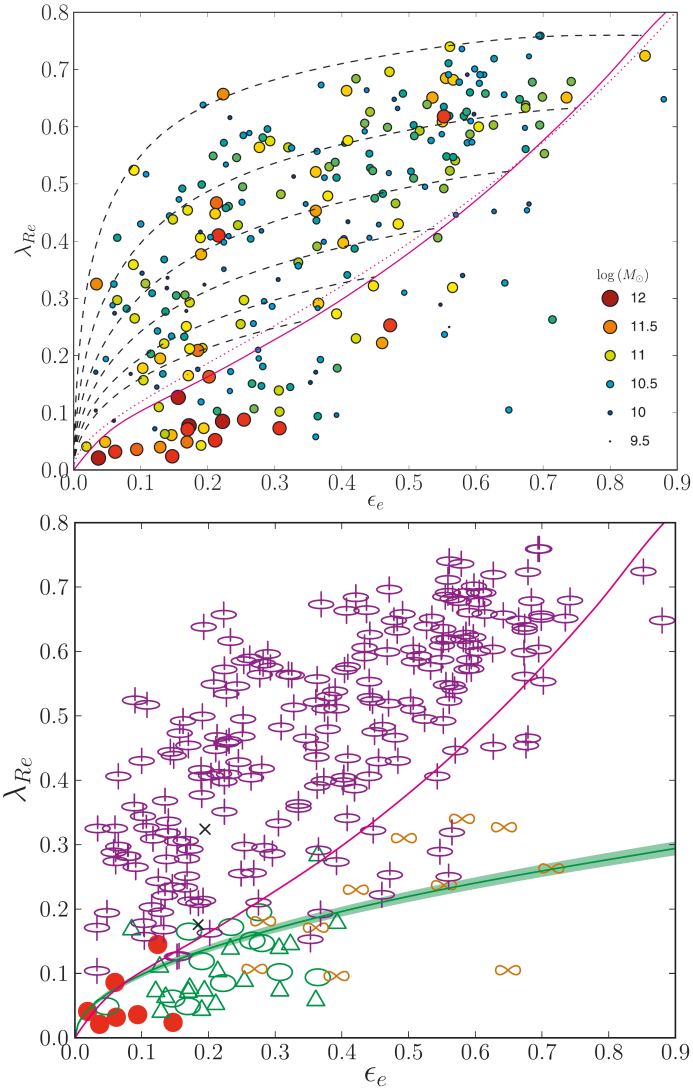

Figure 2.9: The λ_R within R_e as a function of the apparent ellipticity in the ATLAS^{3D} survey. The top panel shows the galaxies colour-coded by their stellar mass, and the bottom panel shows the galaxies separated into regular (purple ellipses) and non-regular (green ellipses) rotators, with kinematically decoupled cores (green triangles), with two off-centred velocity dispersion peaks (orange symbols), without clear rotational signal (red), and non-classified galaxies (crosses). See text for further details. Image credit: Figures 3 (top) and 7 (bottom) of Emsellem et al. (2011).

most common sources of kinematic peculiarities (Naab et al., 2014). Major mergers can either result in the spin-up or spin-down of the galaxy rotation, with the final outcome being the result of a complex combination of the gas fraction, galaxy mass ratio, orbital configuration, environment and redshift.

2.4 Relics of star formation: star clusters

Globular clusters (GCs) are the oldest, most massive self-bound stellar components in galaxies such as the Milky Way. These massive, dense star clusters have been able to survive for long periods of time while less massive star clusters, usually termed open clusters (OCs), disperse typically on a time-scale of up to ~ 100 Myr due to gradual mass loss and close encounters with molecular clouds. The formation of GCs is one of the key open questions of modern astrophysics. In addition, the connection of GCs to the population of young, massive clusters (YMCs) and whether YMCs might evolve later to show similar properties with GCs is under active study.

2.4.1 Present-day observations

The Milky Way contains some 160–170 GCs (Harris, 1991; McLaughlin & van der Marel, 2005), and more candidates are found in deep surveys such as the VVV and the Gaia survey (Moni Bidin et al., 2011; Camargo & Minniti, 2019). Table 2.1 shows a few parameters used in differentiating between different types of star clusters observed in the Milky Way. The GCs probe the age and matter structure, as well as the kinematics, of the galactic halo and the bulge, which consist of predominantly old

cluster	age [Myr]	$m_{\rm to}$ [$M_\odot$]	M [$M_\odot$]	$r_{\rm vir}$ [pc]	ρ_c [$M_\odot$ pc^{-3}]	Z [$Z_\odot$]	location	$t_{\rm dyn}$ [Myr]	$t_{\rm rh}$ [Myr]
OC	$\lesssim 0.3$	$\lesssim 4$	$\lesssim 10^3$	1	$\lesssim 10^3$	~ 1	disk	~ 1	$\lesssim 10^2$
GC	$\gtrsim 10$	~ 0.8	$\gtrsim 10^5$	10	$\gtrsim 10^3$	< 1	halo	$\gtrsim 1$	$\gtrsim 10^3$
YMC	$\lesssim 0.1$	$\gtrsim 5$	$\gtrsim 10^4$	1	$\gtrsim 10^3$	$\gtrsim 1$	galaxy	$\lesssim 1$	$\lesssim 10^2$

Table 2.1: Some typical values for the properties used to distinguish GCs, OCs and YMCs in the Milky Way. From left to right, the columns show the age, the stellar main-sequence turn-off mass, the total mass, the virial radius, the central density, the stellar metallicity, the typical location in the Milky Way, the dynamical time-scale, and the relaxation time-scale. Image credit: Table. 1 of Portegies Zwart et al. (2010).

stars formed at around the same time as the GCs. OCs and YMCs on the other hand populate the disk and other regions where star formation is still actively ongoing. These objects have typically ages up to only a few hundred Myr due to the fact that they are more prone to disruption, and they can be used to probe the more recent star formation activity.

Fig. 2.10 and 2.11 show the effective radii ($R_{\rm eff}$), stellar masses, and mean surface densities within $R_{\rm eff}$, calculated as

$$\Sigma_{\rm eff} = \frac{M_*}{2\pi R_{\rm eff}^2}, \tag{2.14}$$

of various types of hot, velocity dispersion supported stellar systems in and outside of the Local Group (Misgeld & Hilker, 2011). The dashed line in Fig. 2.10 indicates the zone-of-avoidance in the M_*–$R_{\rm eff}$ space where no objects seem to reside, and the dotted line shows the best-fit $M_* \propto R_{\rm eff}^{5/3}$ relation from Dabringhausen et al. (2008). The dot dashed line in Fig. 2.10 shows a version of the M_*–$R_{\rm eff}$ relation where the two-body relaxation time-scale (see e.g. Chapter 3.1.4) has been factored in and set as a constant values equal to the Hubble time (see Dabringhausen et al. 2008 and Misgeld & Hilker 2011 for details). In Fig. 2.11, the dashed and dot dashed lines indicate the same relations as in Fig. 2.10 but translated to a mean $\Sigma_{\rm eff}$ according to Eq. 2.14, and the two dotted lines show the $\Sigma_{\rm eff}$–$R_{\rm eff}$ relation at constant values of $R_{\rm eff} = 3$ pc and $R_{\rm eff} = 1$ kpc. Massive star clusters and GCs clearly populate a region of the parameter space in both of the figures separate from galactic bulges, elliptical galaxies, dwarf galaxies, and even nuclear star clusters.

The cluster mass function (CMF) of star clusters is described typically as a function of the number of clusters N per unit mass dM using a power-law function as

$$N \propto M^{\alpha} \quad \text{or} \quad dN \propto M^{\beta} dM \tag{2.15}$$

where the power-law index is typically of the order $\beta = \alpha - 1 \sim -2$ (Lada & Lada, 2003). The power-law provides usually a good fit to the CMF especially for observed star clusters, where the completeness limit extends only down to $10^{2.5}$–$10^{3}\,{\rm M}_{\odot}$ (Cook et al., 2012; Messa et al., 2018; Hannon et al., 2019). An exception is the special case of the Milky Way where also very low-mass OCs can be observed. The lower mass limit of the cluster mass distribution is usually defined as few tens of stars (Lada & Lada, 2003). The power-law mass function follows naturally from the self-similar power-law distribution of the progenitor molecular clouds (Elmegreen & Falgarone, 1996) which have a slightly shallower mass function with a power-law index typically of the order of $[-1.7, -1.8]$ (Lada et al., 1991; Heithausen et al., 1998).

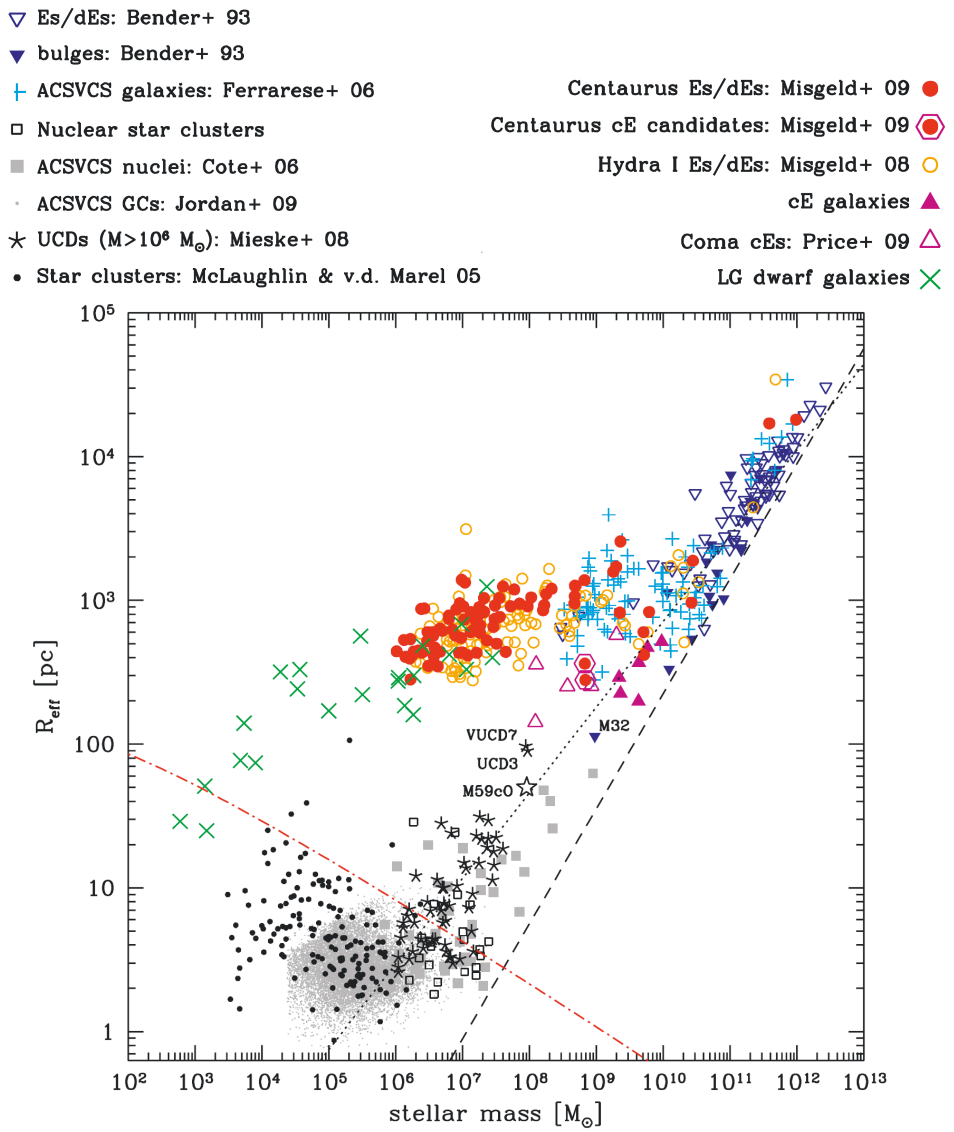

Figure 2.10: The effective radii $R_{\rm eff}$ as a function of stellar mass for star clusters in the Local Group and the Virgo cluster (black and grey dots), compared to various other types of hot, velocity dispersion supported stellar systems. Star cluster-type objects are clearly separated in the parameter space from the galaxy-type objects. Image credit: Figure 4 of Misgeld & Hilker (2011).

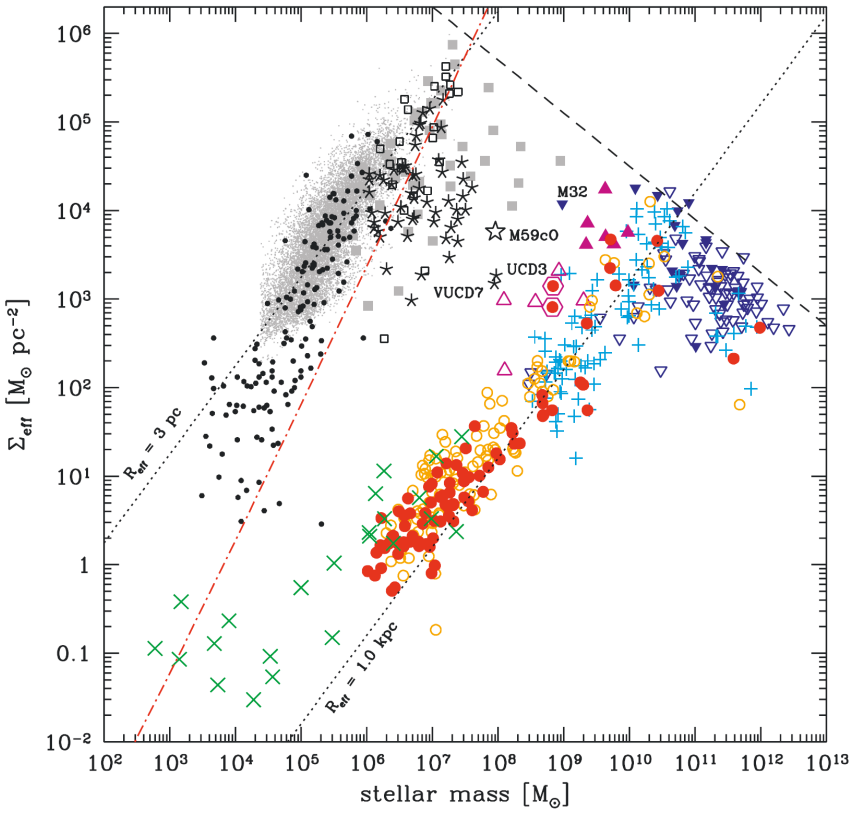

Figure 2.11: Same as Fig. 2.10 but instead as a function of the mean surface mass density within $R_{\rm eff}$. Image credit: Figure 5 of Misgeld & Hilker (2011)

Fig. 2.12 shows observed CMFs for eight galaxies binned with equal-width bins in $\log(M)$ and divided according to the cluster age. Fig. 2.13, on the other hand, shows the detailed CMF and the corresponding cumulative distribution of star clusters in M51 now binned with equal number of clusters per bin, where the low-mass end of the CMF is limited by the observational completeness limit. Fig. 2.12 in particular illustrates the effect of cluster disruption, which proceeds through internal and external processes as a function of the environment and the density and mass of the cluster (Spitzer, 1958; Lamers et al., 2005). The internal disruption is driven by dynamical relaxation processes, while the external disruption rate depends on the tidal field of the surrounding medium. Less dense clusters, which are typically also

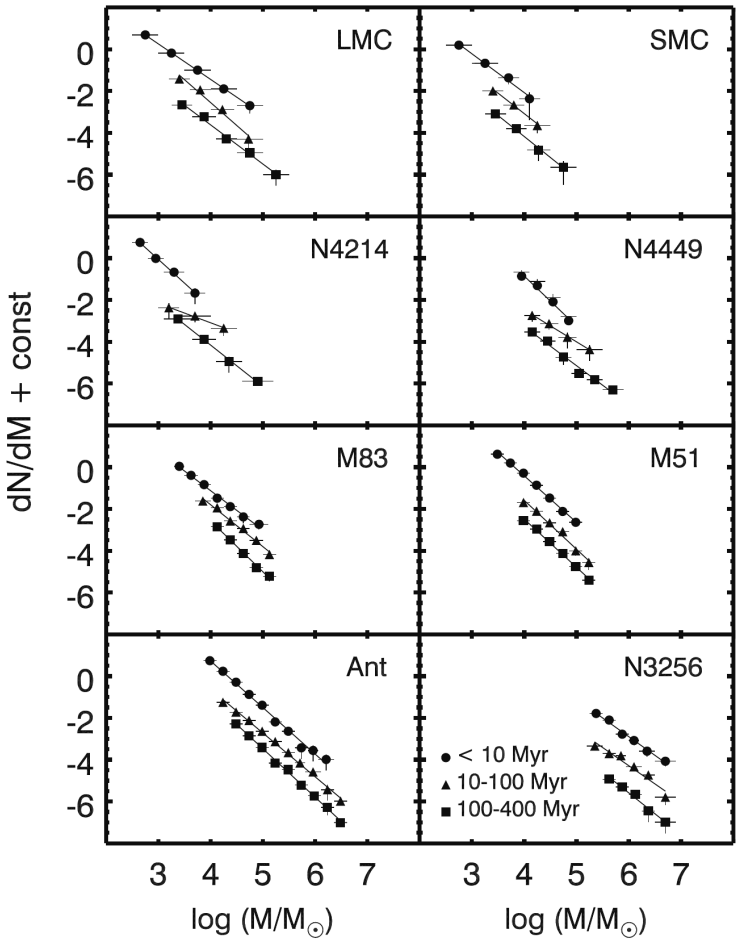

Figure 2.12: The binned (equal bin width) CMFs in a set of galaxies, where the clusters have been divided by age into three groups: < 10 Myr (circles), 10–100 Myr (triangles) and 100–400 Myr (squares). Image credit: Figure 4 of Chandar et al. (2017).

less massive, disrupt faster, and the denser the environment the faster the disruption is (Gieles et al., 2006). The most extreme disruption happens when the interstellar gas remains undisturbed, and the clusters remain in a field of high-density gas such as is present in the spiral structure of disk galaxies. The newly formed star clusters can disrupt as rapidly as a factor of ten in the number of clusters per each factor of

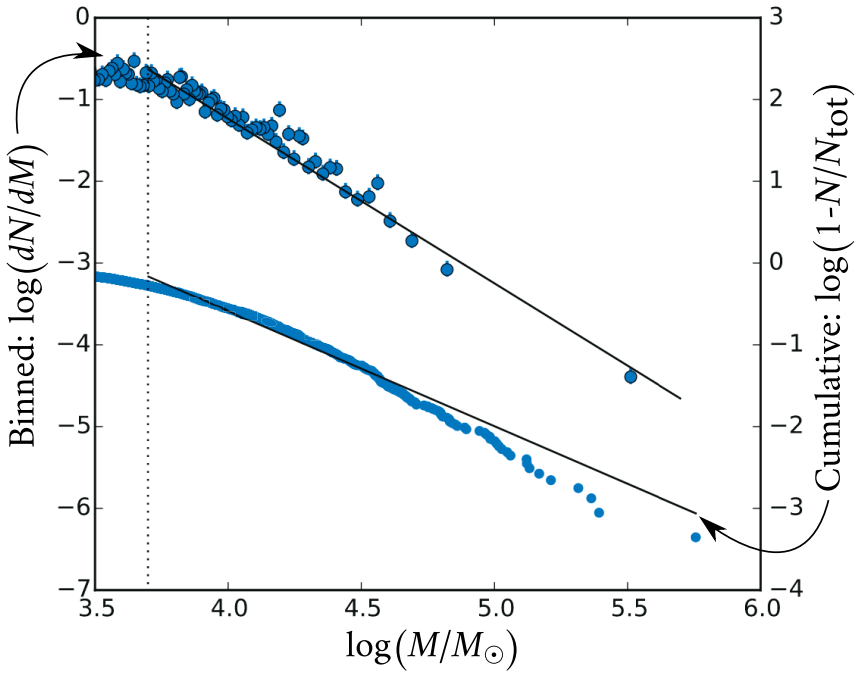

Figure 2.13: The binned (equal number of clusters per bin) CMF and the respective cumulative mass function in the M51 galaxy. The vertical dotted line shows the completeness limit of 5000 $M_\odot$. Image credit: Figure 11 adapted from Messa et al. (2018).

ten in age (τ) (Fall et al., 2005; Whitmore et al., 2007), i.e. $dN/d\tau \sim \tau^{-1}$.

There is an ongoing discussion on whether the upper limit of the CMF is a factor set by the star formation environment (Larsen, 2009; Portegies Zwart et al., 2010; Adamo et al., 2015; Kruijssen, 2015; Messa et al., 2018), or if such a limit exists at all (Mok et al., 2019). If the maximum cluster mass follows from the star formation environment, then the majority of GCs we observe locally should be the relics of high-redshift star formation (Kruijssen, 2015) and only able to form today in extreme environments. An environmentally dependent upper limit for allowed cluster masses could also indicate a more Schechter-like cluster mass function in for example galactic disks, where the gas surface densities decrease towards larger radii (Adamo et al., 2015).

The universality of the initial CMF has also been challenged by metallicity studies

in GCs in the Local Group, where significantly more low-metallicity stars are found in GCs (Larsen et al., 2012) than the $\sim 10\%$ expected from a power-law mass function down to $\sim 100\,\mathrm{M}_\odot$ combined with the traditional models for cluster disruption. These results have given rise to the idea of an environmental dependence of the lower-mass limit of clusters as well (Trujillo-Gomez et al., 2019), where the high-redshift star formation environments ($> 10^2\,\mathrm{M}_\odot\,\mathrm{pc}^{-2}$) would produce a CMF with a higher cut-off mass.

2.4.2 The cluster formation efficiency

Star clusters in general form in star formation regions at a few ten per cent cluster formation efficiency (CFE or Γ) defined as

$$\Gamma = \frac{M_{*,\,\mathrm{cl}}(\tau)}{M_*(\tau)} \quad \text{or} \quad \Gamma = \frac{\mathrm{CFR}}{\mathrm{SFR}} \tag{2.16}$$

where $M_{*,\,\mathrm{cl}}(\tau)$ is the mass in star clusters up to a certain age τ (e.g. τ =10 Myr) and $M_*(\tau)$ is the total mass in stars formed during the same period of time. The latter definition using cluster formation rate (CFR) and SFR assumes that they have both remained constant for the time period under study. More intense star formation regions characterised by higher SFR surface densities seem to both form star clusters that are more massive (Larsen, 2009; Elmegreen, 2018) and at a higher cluster formation efficiency (Larsen & Richtler, 2000; Kruijssen, 2012).

The observed values of the CFE depend strongly on the procedure of selecting the star clusters under study. Young clusters are a necessity for capturing the initially formed cluster population, but due to the disruption processes outlined in the previous Section the majority of the young clusters may be associations or open clusters on the verge of being disrupted. The observational literature relies on two methods when selecting the clusters to determine the CFE: the *inclusive* and the *exclusive* methodology. The inclusive observations aim at being complete by including all clusters in a relatively narrow age bracket (e.g. $\leq$ 10 Myr, Chandar et al. 2017), while the exclusive observations aim at only selecting bound star clusters but with a broader age interval (e.g. $\leq$ 100 Myr, Cook et al. 2012; Adamo et al. 2015; Messa et al. 2018). These two methodologies have consequently arrived at somewhat disagreeing conclusions in the recent literature (Chandar et al., 2017). The inclusive methods have implied a constant CFE independent of the environment, while the exclusive methods agree more with analytic predictions (Kruijssen 2012) where a positive correlation between the CFE and the environment is observed.

The connection between star and star cluster formation in different environments is therefore a topic of ongoing research in the field of star clusters.

2.4.3 The formation of globular clusters

Open questions related to the formation process of globular clusters also directly connect to the formation of galaxies. Understanding how GCs form is an integral part in our ability to interpret the past evolution of galaxies from observations. The formation of GCs in particular requires firstly the ability to collect more than $10^5\,M_\odot$ of bound stellar mass within a region with a half-mass radius of a few pc, and secondly the mass has to remain bound for an extended period of time. The star formation environment at high redshift was therefore particularly favourable for the formation of massive star clusters; the Jeans mass was higher and thus enabled the collapse of more massive structures in the higher temperature, lower metallicity, and more turbulent gas conditions present at high redshifts. If the GCs formed as massive clusters in the turbulent disks at high redshifts, they would then naturally end up in the haloes of today's massive galaxies through galaxy mergers and accretion due to the hierarchical nature of galaxy evolution (Kruijssen, 2015).

Observationally it is challenging to make direct connections between the present-day YMC formation and the formation of old GCs. Even the next generation observational facilities will only be able to resolve the formation sites of GCs at a resolution of a few pc at redshifts as high as $z \sim 6$ (Vanzella et al., 2019) where the majority of the old GCs appear to have built up their mass. The extreme environments, present in the high-redshift Universe, can however be probed in the present-day Universe through for example violent gas-rich galaxy mergers. The formation of massive star clusters is observed in the local Universe in the form of super star clusters (SSCs, $M_* > 10^6\,M_\odot$) in highly disturbed systems such as the Antennae galaxies (Whitmore et al., 2010). However, as indicated by the parameters shown in Table 2.1, the YMCs forming in today's spiral galaxies have higher metallicities and of course younger ages than the observed GCs. In principle the YMCs in the Milky Way cannot evolve into objects like the GCs we see today. In a different environment, such as a merger of low-metallicity dwarf galaxies as presented in Lahén et al. (2019), the observational disagreement between YMCs and GCs might however be somewhat alleviated by the galactic conditions. The debate on whether GCs can still form today or if they were the result of specific conditions only present in the young Universe is therefore still ongoing.

3 The hydrodynamical code GADGET-3

One key challenge in observational astronomy is that we only have a single snapshot of the Universe. The light we observe has travelled through vast interstellar and intergalactic distances, and we are restricted to view each object from only one point of view. To aid in alleviating this fundamental issue, we have turned to numerical simulations for the past fifty years. The enormous increases in computing power during the past couple of decades, and the increasing sophistication of simulation codes, have resulted in huge advances in both the number of resolution elements that can be simulated and the spatial scales that can be probed.

One of the most popular methods used to model the evolution of matter in the Universe is the N-body method, which represents the matter constituents in a simulation as gravitationally interacting point particles. Since the advent of the first N-body simulations performed with only tens or hundreds of particles (Aarseth, 1963; Toomre & Toomre, 1972), we can now follow for example the evolution of massive star clusters with stellar mass particles (Wang et al., 2016) and the formation of galaxy clusters at sub-kpc spatial resolution (Vogelsberger et al., 2018) over the entire cosmic history of the Universe.

GADGET-3, a successor to the highly successful GADGET-2 code (Springel, 2005), is a sophisticated hydrodynamical N-body code with a plethora of built-in astrophysical models. The astrophysical processes which cannot be fully resolved have been incorporated as a set of sub-resolution models, which can be used to follow for example stellar feedback in simulations with particles significantly more massive than a few solar masses. The underlying hydrodynamical framework is based on the initial work by Springel et al. (2001b), Springel & Hernquist (2002) and Springel (2005). The original two-phase gas physics, which used an effective equation of state (Springel & Hernquist, 2003) with a cooling temperature floor, has been recently replaced with detailed non-equilibrium cooling and heating processes using a chemical network for low-temperature gas (Hu et al., 2016).

3.1 N-body

3.1.1 The spatial tree structure

In general the gravitational force from any mass element has an infinite reach. Thus a true N-body code requires $N(N-1)/2$ force computations for N particles to decipher their movement. To alleviate the high computational demand, a spatial *tree* data structure can be used to clump together distant particles, substantially reducing the number of computations executed on each time step. The idea of the tree lies in its name; the entire simulation volume (root) is divided into hierarchical sub-regions (branches) until all N particles occupy their own cells (leaves). The specific version implemented in GADGET-3, the Barnes-Hut tree (Barnes & Hut, 1986), uses an octree based algorithm which recursively divides the volume into eight equal cubes and discards any cube with no particles. Fig. 3.1 illustrates the Barnes-Hut algorithm and its relevant parameters, projected in two dimensions.

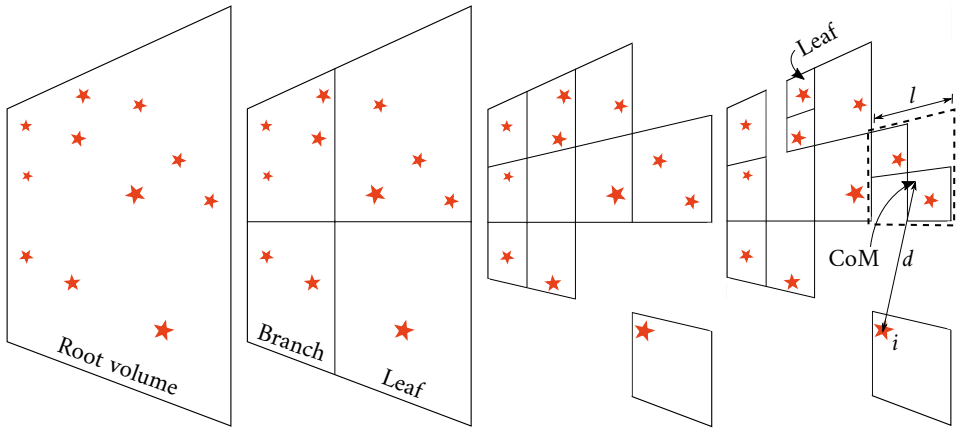

Figure 3.1: A simplified illustration of the Barnes-Hut algorithm in two dimensions (following Fig. 1 of Springel et al. 2001b). The dashed region, with its side length l and centre of mass (CoM) indicated, is a branch at a distance of d from particle i.

The gravitational force acting on a given particle can then be calculated explicitly from particles in nearby branches, or approximately from distant branches if a criterion for opening the tree further is not satisfied. In GADGET-3 the criterion is based on the so-called opening-angle $\theta = l/d$, where l is the side-length of the distant volume, and d is the distance between the particle and the centre of mass

of the distant volume (see Fig. 3.1). The simple opening angle is used on the first time step, with a typical value of $\theta \in [0.5, 0.7]$. At the limit of $\theta \to 0$ the calculation reduces to a direct summation (i.e. all branches are opened), resulting in the behaviour of an N-body code where all particle-to-particle forces are calculated.

During the rest of the simulation, GADGET-3 monitors the accuracy of the force calculations using a more sophisticated criterion of

$$\frac{GM_{\rm b}}{d}\left(\frac{l}{d}\right)^2 \leq \alpha_{\rm f}|\mathbf{a}| \tag{3.1}$$

where $M_{\rm b}$ is the mass of the distant branch, $|\mathbf{a}|$ is the acceleration of the branch on the previous time step, and $\alpha_{\rm f}$ is the input force error tolerance with a typical value set to $\alpha_{\rm f} \sim 0.005$. GADGET-3 uses only the monopole force (i.e. the Newtonian force) exerted by the distant branch, and the criterion above monitors the error estimate due to the fact that the quadrupole moment is discarded. If the criterion is not filled, the tree force acting on a given particle is calculated (at least) from the next deeper level of the tree.

Distant volumes which fill the criterion then exert a collective force on a given particle according to the position and velocity of the centre of mass of all particles in that volume. By considering the collective force instead of the force from each individual particle, the cost of using a tree for gravity calculations is reduced to $\mathcal{O}(N \log N)$ (Appel, 1985).

3.1.2 Softened gravity

A serious complication when computing the gravitational forces arises from the diverging nature of the gravitational potential at small separations. The stellar, gaseous and dark matter particles are mostly modelled with massive particles (mass resolution $\gg \mathrm{M}_\odot$), and for example the process of stellar collisions is beyond the scope of the majority of galactic-scale simulations. Therefore, due to the limited mass resolution, close interactions between particles are not in general resolved correctly. Artificial scattering events may occur, especially between particles with large mass ratios.

A popular solution to this problem is gravitational softening, which prevents close encounters from being too strong when massive particles are used. This is implemented by replacing the gravitational potential of a particle at distances near or smaller than a given softening length h with a smoothly transitioning potential which tends to a zero gravitational force at zero distance. The softened gravitational

force from a nearby particle is given by a softened Newtonian potential

$$\Phi(r) = \frac{Gm}{h} W\left(\frac{r}{h}\right) \tag{3.2}$$

where W is the softening kernel, implemented in GADGET-3 using the W_2 spline kernel (Springel et al., 2001b)

$$W_2\left(\frac{r}{h}\right) = \begin{cases} \frac{16}{3}\left(\frac{r}{h}\right)^2 - \frac{48}{5}\left(\frac{r}{h}\right)^4 + \frac{32}{5}\left(\frac{r}{h}\right)^5 - \frac{14}{5}, & 0 \le \frac{r}{h} < \frac{1}{2} \\ \frac{1}{15}\left(\frac{r}{h}\right)^{-1} + \frac{32}{3}\left(\frac{r}{h}\right)^2 - 16\left(\frac{r}{h}\right)^3 + \frac{48}{5}\left(\frac{r}{h}\right)^4 - \frac{32}{15}\left(\frac{r}{h}\right)^5 - \frac{16}{5}, & \frac{1}{2} \le \frac{r}{h} < 1 \\ -\left(\frac{r}{h}\right)^{-1} & \frac{r}{h} \ge 1 \end{cases} \tag{3.3}$$

Such a modification to the gravitational potential gives a Plummer-equivalent (Plummer, 1911) softened potential of

$$\Phi_P(r) = -\frac{Gm}{\sqrt{r^2 + \epsilon^2}} \tag{3.4}$$

at $r = 0$ when $h = 2.8\epsilon$, but follows more closely the Newtonian potential at intermediate radii as illustrated in Fig. 3.2. The gravitational softening also results in a speed-up of the numerical calculations because the strongest interactions requiring the shortest time steps are removed.

3.1.3 The leapfrog integrator

For galactic-scale simulations, consisting of millions of particles, the equations of motions need to be integrated accurately but also efficiently. For this, GADGET-3 employs the leapfrog-method which is used to evolve the positions and velocities according to kick and drift operators derived from Hamiltonian mechanics (see e.g. Quinn et al. 1997 and Springel 2005). The evolution of the system under study given by the approximate leapfrog Hamiltonian thus preserves the phase-space quantities, resulting in a long-term evolution with an oscillating, instead of accumulating, energy error. As a result, the total energy is approximately conserved even during very long integrations (Springel, 2005; Binney & Tremaine, 2008).

The time integration is executed using the kick-drift-kick scheme, whereby the positions and velocities are updated from time step n to $n+1$ step-wise as

$$\begin{aligned} \mathbf{v}_{n+1/2} &= \mathbf{v}_n + \frac{1}{2}\mathbf{a}(\mathbf{r}_n)\Delta t_g && 1/2\,\text{kick} \\ \mathbf{r}_{n+1} &= \mathbf{r}_n + \mathbf{v}_{n+1/2}\Delta t_g && \text{drift} \\ \mathbf{v}_{n+1} &= \mathbf{v}_{n+1/2} + \frac{1}{2}\mathbf{a}(\mathbf{r}_{n+1})\Delta t_g && 1/2\,\text{kick} \end{aligned} \tag{3.5}$$

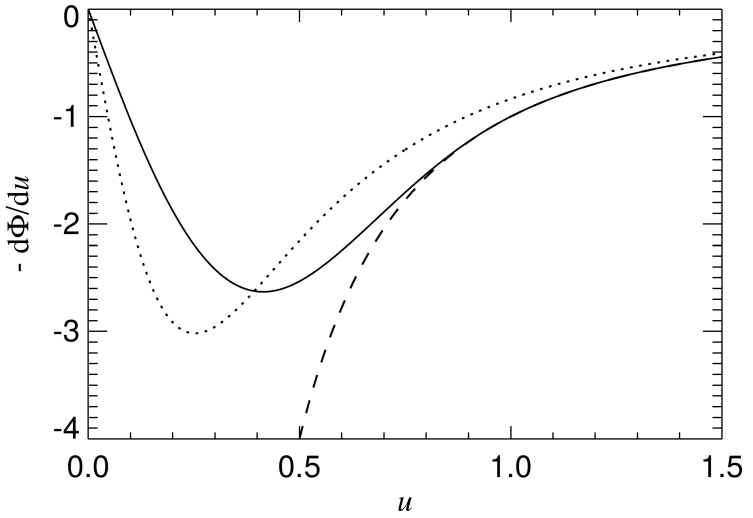

Figure 3.2: The softened gravitational force described by the W_2 kernel (solid) and the Plummer model (dotted) compared with the Newtonian force (dashed). Here $u = r/h$ as used in Eq. 3.2, and the softening lengths have been set as $h = 1.0$ and $\epsilon = h/2.8$. Image credit: Figure 14 of Springel et al. (2001b).

where Δt_g is the time step length, and $\mathbf{r}$, $\mathbf{v}$ and $\mathbf{a}$ are the position, velocity and acceleration of the particle on step n, on half-step $n + 1/2$ and on step $n + 1$. The result is an integrator which has an error proportional to the global time step as Δt_g^2.

3.1.4 Collisional dynamics: the KETJU module

Gravitational systems can be divided into collisionless and collisional depending on whether or not two-body interactions are driving relatively rapid dynamical relaxation. The relaxation time-scale of a gravitating system with N particles can be approximated using the crossing time-scale, $t_{\rm cross}$, as

$$\frac{t_{\rm relax}}{t_{\rm cross}} \approx \frac{N}{6\ln(N/2)} \tag{3.6}$$

(Binney & Tremaine, 2008). For globular clusters, with 10^5 stars and crossing times of the order of a Myr, the relaxation occurs on a time-scale of 10^3 Myr, while small clusters, such as open clusters with only a few hundred stars, relax over a time-scale of only tens of Myrs. Galaxies, on the other hand, contain of the order of 10^{11} stars with

crossing times of tens to hundreds of Myrs. Such systems take $\sim 10^{11}$–10^{12} Myr to relax, which is considerably longer than the age of the Universe (Sparke & Gallagher, 2007).

The main deficiency of the gravitational softening method is that it imposes a resolution limit on which the gravitational dynamics can be accurately resolved. This is acceptable and in fact necessary in collisionless systems, such as galaxies, where the close-range interactions are not important nor resolved. In collisional systems, where the evolution should be governed by gravitational scattering, such as stellar populations around supermassive black holes (SMBHs) or the inner regions of stellar clusters, the gravitational softening slows or completely halts the evolution of such systems.

Various implementations for adding the collisional nature of the interactions without having to calculate all the gravitational forces using a direct summation technique have been introduced in the literature. For example, short-range scattering of particles has been implemented in the form of artificial dynamical friction (Tremmel et al., 2015) using the density and velocity dependent dynamical friction formulae derived in Chandrasekhar (1943). Another approach is to actually solve the gravitational interactions with direct summation, but only within the systems of interest themselves. Such a method was introduced by Rantala et al. (2017), where certain regions within a GADGET-3 simulation are integrated using an algorithmic regularisation chain method, i.e. AR-CHAIN, implemented in the KETJU (Finnish for *chain*) integration module. AR-CHAIN, the core of the KETJU module, builds on three numerical methods which we briefly introduce here.

Algorithmic regularisation

The AR-CHAIN method employs the Logarithmic Hamiltonian method (Mikkola & Tanikawa, 1999; Preto & Tremaine, 1999; Mikkola & Merritt, 2006), where the equations of motion have been reformulated using a time-transformed coordinate system. The time-transformation introduces a new time-coordinate s, which is the old time scaled with the potential energy of the system, i.e. $s = |U|dt$. For example in a case of a close encounter, time is essentially slowed down, and the integrator has a longer (although fictitious) time-interval to process. Full regularisation, such as the KS-regularisation (see Kustaanheimo & Stiefel 1965), would require additional coordinate transformations which result in the complete removal of coordinate singularities. The time-transformation only makes it easier for the algorithm to calculate close encounters in the presence of a coordinate singularity. The *algorithmic* regularisation means that even though the singularity of the point

mass potential has not been removed, the time-transformation together with the chain-coordinates (see below) and the leap-frog integrator (see Section 3.1.3) allows successful integration of even collision orbits.

The chain-subsystem

Numerical floating-point round-off errors accumulate when large numbers of a similar magnitude are subtracted. Such a case is presented when we calculate the relative distances to a set of particles far from the origin of the global coordinate system. To reduce the numerical round-off error, the AR-CHAIN algorithm uses a chained coordinate system (Mikkola & Aarseth, 1993), which uses a local coordinate system and interparticle vectors.

For a set of particles in a pre-defined region, the *chain* is constructed as follows:

1. move the particles into their local centre of mass
2. calculate all interparticle vectors and search for the two particles closest to each other, and set them as the *head* and the *tail* of the chain
3. continue adding the next closest particle either as the new head or the new tail, until all particles have been included in the chain.

Particles close to each other in the chain use the chain interparticle vectors in summing up the gravitational forces, whereas the other distances in the chain-region are calculated in the local centre of mass coordinate-frame to prevent accumulating errors from summing up the interparticle vectors. Numerical tests have shown that particles up to a distance of two steps in the chain should be calculated using the interparticle vectors (Mikkola & Merritt, 2008).

The Gragg-Bulirsch-Stoer extrapolation method

The chained subsystem with the time-transformed equations of motion is then integrated using the standard leapfrog integrator (Section 3.1.3), but using the Gragg-Bulirsch-Stoer (GBS) extrapolation method. The GBS method ensures that the integration is performed at a desired accuracy. The central idea of GBS is to divide the current time step T into $n_k = 2k$ sub-steps $\Delta t = T/n_k$ (where $k = 1, 2, \dots$), just as in the global GADGET-3 time-stepping (see Chapter 3.2.2), and integrate the equations of motion in ever decreasing sub-steps Δt by calling the leapfrog over and over again. Each set of sub-steps results in a value for each dynamical variable $f(\Delta t)$, which yields a sequence of solutions in the Δt vs. $f(\Delta t)$

space. This set of solutions is then extrapolated to $\Delta t \to 0$ (that is $n_k \to \infty$) using simple polynomial extrapolation. If the difference between consecutive extrapolations of n_k and n_{k+1} is less than the pre-defined error tolerance, the current time step of the AR-CHAIN subsystem is considered converged. If the consecutive extrapolations do not converge after a few sub-divisions (namely 8 sets of extrapolations in Rantala et al. 2017, 2018), the original time step T is divided in half and the routine is started all over again.

3.2 Gaseous astrophysics

3.2.1 Smoothed particle hydrodynamics

The hydrodynamical forces in GADGET-3 use a smoothed particle hydrodynamics (SPH) formalism (Lucy, 1977; Gingold & Monaghan, 1977; Monaghan, 1992). SPH is used to model the gas as a fluid that is sampled by a finite set of particles. The idea is to use a discrete interpolant over a set of neighbouring particles with mass m and density ρ to obtain a hydrodynamical property f at any position defined as

$$f(\mathbf{r}) = \sum_b m_b \frac{f_b}{\rho_b} W(|\mathbf{r} - \mathbf{r}_b|, h_g). \tag{3.7}$$

Here W is a kernel function, which depends on the relative distances to each particle and the smoothing length h_g. For example, the density of a gas particle i is given as a smooth average over N neighbours as

$$\rho_i = \sum_{j=1}^{N} m_j W(|\mathbf{r}_i - \mathbf{r}_j|, h_g). \tag{3.8}$$

The smoothing length varies adaptively with the gas density, according to the chosen number of neighbours N. The original cubic spline softening kernel used in previous versions of GADGET can be replaced in GADGET-3 with the more numerically stable Wendland C^4 kernel (Dehnen & Aly, 2012), given that the number of neighbours (typically from tens to hundreds) is also set to a high number, of the order from $N \sim 100$ to $N \sim 200$.

When the chosen kernel function is differentiable, the equations of motion can then be obtained by differentiating the interpolant. The basic equation of motion of a particle i as a function of the pressure and density over its neighbours can be

written following Monaghan (1992) as

$$\frac{d\mathbf{v}_i}{dt} = -\sum_{j=1}^{N} m_i \left(\frac{P_j}{\rho_j^2} + \frac{P_i}{\rho_i^2} \right) \nabla_i W(|\mathbf{r}_i - \mathbf{r}_j|, h_g) \tag{3.9}$$

The hydrodynamical accuracy of SPH, especially in calculating fluid mixing at contact discontinuities, is set partly by the choice of variables used in the integration of Eq. 3.9. The most common formulations use density or pressure paired with either entropy or the internal energy (see e.g. Hopkins 2013).

The SPH formalism is constructed to conserve energy, entropy, and (angular) momentum. This poses problems when we encounter shocks, where the entropy may actually increase but should not dissipate out of the shock region too rapidly. Hence, the SPH equations are generally supplemented with a few extra terms. The most important addition is the artificial viscosity (AV) term Π as

$$\frac{d\mathbf{v}_i}{dt} = -\sum_{j=1}^{N} m_i \left(\frac{P_j}{\rho_j^2} + \frac{P_i}{\rho_i^2} + \Pi_{ij} \right) \nabla_i W(|\mathbf{r}_i - \mathbf{r}_j|, h_g), \tag{3.10}$$

which is used to make shocked gas viscid. The original formulation of AV (see e.g. Monaghan 1992), where the kinetic energy in the gas was simply transferred into internal energy, had difficulties for example with keeping the entropy and heat increase localised at the shock front.

To improve the treatment of dissipation in the case of shear motion, Balsara (1995) introduced a correction factor which reduces AV when rotational shear dominates (i.e. when the vorticity $\nabla \times \mathbf{v}$ of the local velocity field dominates over the convergence $\nabla \cdot \mathbf{v}$). Another improvement by Morris & Monaghan (1997) makes the strength of the AV adaptive for each particle as a function the local velocity convergence, in order to reduce dissipation in the presence of weak shocks. Morris & Monaghan (1997) also introduced a decay function for determining the strength of the AV, which sets a decay time-scale for the AV for example behind a shock front (see e.g. Wetzstein et al. 2009 and Hu et al. 2014 for more detailed discussions). Further improvements for better shock-detection and pre/post-shock differentiation have been proposed for example in Cullen & Dehnen (2010).

When two SPH particles approach and cross paths, the thermodynamical quantities (except for the ones being kernel-averaged) at that position may get multiple unequal values if the particles do not have identical gas properties. In real gas this would be alleviated by mixing, but SPH samples the gas as discrete particles which represent massive regions of gas. The kinetic energy is dissipated using AV,

while internal energy (or entropy) requires an implementation for thermal conduction (see e.g. Read & Hayfield 2012). Artificial conduction (AC), which mimics the effects of the traditional equation of thermal conduction, is a common solution to smooth out entropy discontinuities. AC is typically implemented with a similar limiter as with AV, which detects strong shocks and conducts heat away from entropy jumps (Read & Hayfield, 2012; Hu et al., 2014).

3.2.2 Time steps

The first particle-based numerical integration schemes used a single global time step length for all of the simulation particles. With the introduction of dissipational components, such as gas, the density contrasts between the simulated regions grew quickly, and using a global time step became quickly extremely inefficient. Therefore, various methods for selecting the time step length adaptively were introduced.

The time step structure in GADGET-3 is constructed using block time steps, i.e. by binning the particles into a sequence of pre-determined, hierarchical step lengths. The total simulation time is divided into smaller steps by dividing each consecutive step by two, and the time step bin of each particle is defined based on the local (hydro)dynamical time-scale. For collisionless particles, such as dark matter and stars, the time step bins are set using the criterion

$$\Delta t_{=} \left(\frac{2\eta\epsilon}{|\bar{\mathbf{a}}|} \right)^{1/2} \tag{3.11}$$

using the gravitational Plummer softening length $\epsilon = h/2.8$, the acceleration of the particle $|\bar{\mathbf{a}}|$, and an input accuracy parameter η. For SPH particles, the time stepping is set as the minimum of $[\Delta t_g, \Delta t_c]$, where Δt_c is the time-scale given by the Courant-condition

$$\Delta t_c = \frac{\alpha_c h_g}{\max(v_{\rm sig})} \tag{3.12}$$

where the denominator is the maximum local signal velocity, i.e. the sound speed, h_g is the hydrodynamical softening length, and α_c is an input accuracy parameter. Again, in regions where the gas conditions may vary rapidly (such as in shocks), an extra limiter should be used to restrict the time stepping (e.g. Saitoh & Makino 2013). For example, Hu et al. (2014) use a time step limiter which ensures that neighbouring SPH particles have time step lengths which are always within a factor of four of each other.

3.2.3 Cooling of the interstellar medium

The strength of each cooling process in the interstellar gas depends primarily on the chemical composition and the temperature. For gas consisting of primordial elements, i.e. only hydrogen and helium, the collisional excitation of H and He atoms dominate the cooling from 10^4 K to 10^6 K (Black, 1981). For temperatures above this regime the free-free emission dominates, while below 10^4 K (i.e. the hydrogen recombination limit) inefficiently cooling molecular hydrogen is required in large quantities. Adding metals to the composition increases the variety of possible coolants, which has an especially important role in the cooling of star-forming gas at temperatures less than 10^4 K, where primordial coolants are very inefficient. Fig. 3.3 shows the net cooling rate of gas with different chemical compositions at constant density as a function of temperature, and illustrates the effect metals have on the cooling rate especially at temperatures below $\sim 10^4$ K.

The sub-resolution models that govern the cooling of gas in hydrodynamical N-body simulations are typically either restricted by an equation of state at high densities to prevent artificial fragmentation in the star-formation regime (see e.g. Springel & Hernquist 2002; Schaye et al. 2015), or divided into high and low temperature regimes with appropriate cooling functions implemented separately (e.g. Hu et al. 2016). In modern hydrodynamical simulations, the stellar and gaseous abundances of the dozen most universally common elements (for example H, He, C, N, O, Fe, Ne, Mg, Si, S, Ca and Zn) are followed to ensure an accurate modelling of both cooling and feedback processes. At temperatures above $\sim 10^4$ K, the net cooling rate of a particle is simply selected from an array of pre-calculated tabulated values as a function of the gaseous metallicity (e.g. from Wiersma et al. 2009). Fig. 3.3 shows an example of the individual cooling rates of the elements followed in GADGET-3 at solar metallicity, concentrating on temperatures above $T \sim 10^4$ K. At temperatures below $\sim 10^4$ K, the abundance of the different chemical species becomes important, for which chemical networks (such as those presented in Nelson & Langer 1997 and Glover & Mac Low 2007) can be utilised as long as all the system specific reaction rates are included in the model.

3.2.4 Star formation

Gravity is the driving force behind the formation of stars, while the main processes resisting star formation are gas and radiation pressure, turbulence, and potentially magnetic fields. Which process dominates depends on the scale and the environment, but most if not all processes are necessary for the realistic modelling of star formation in galactic-scale simulations.

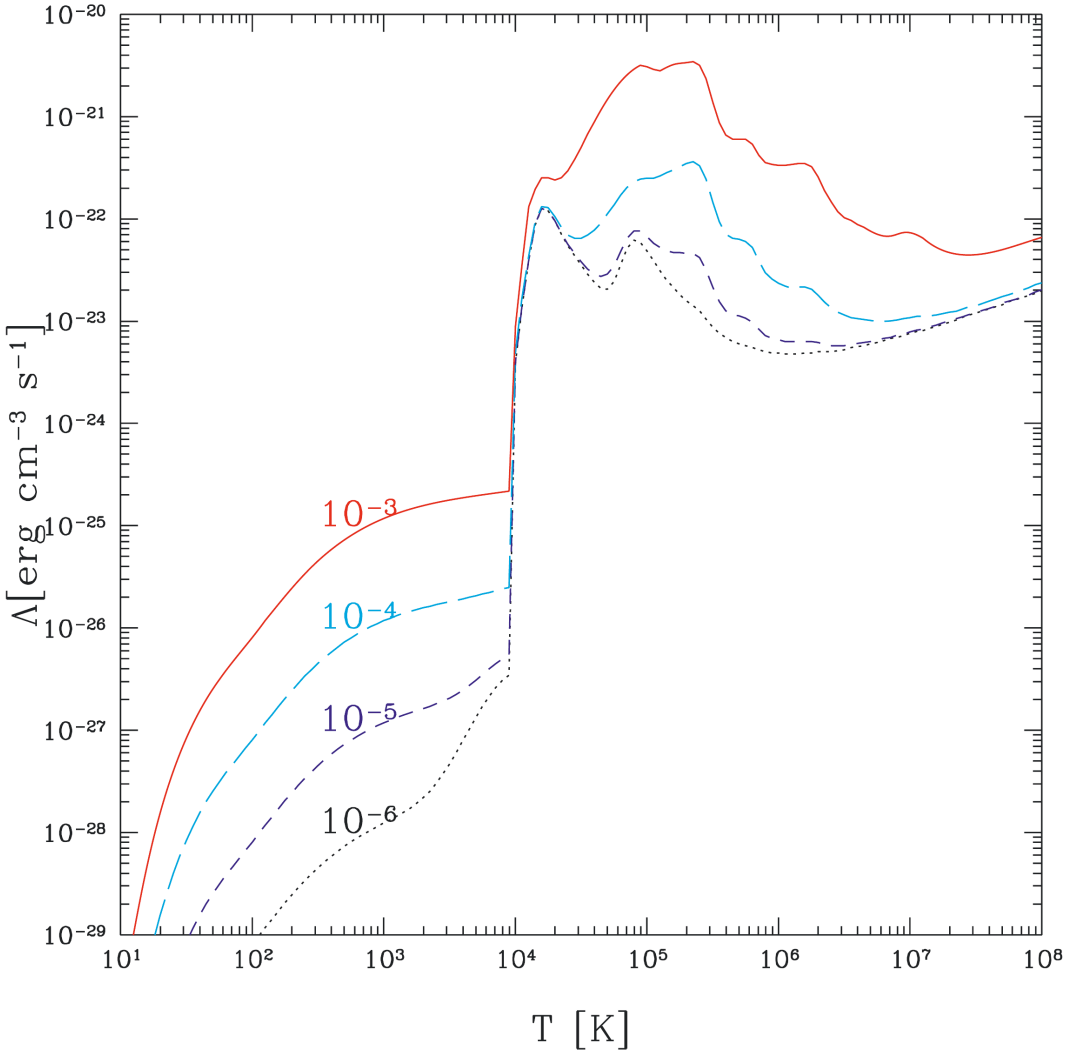

Figure 3.3: The total cooling rate from H, He, H_2 and hydrogen deuteride (dashed) compared with the cooling rate when metals are introduced (labelled according to the metal number fraction) in gas at $n_H = 1$ cm^{-3}. Image credit: Figure 4 of Maio et al. (2007).

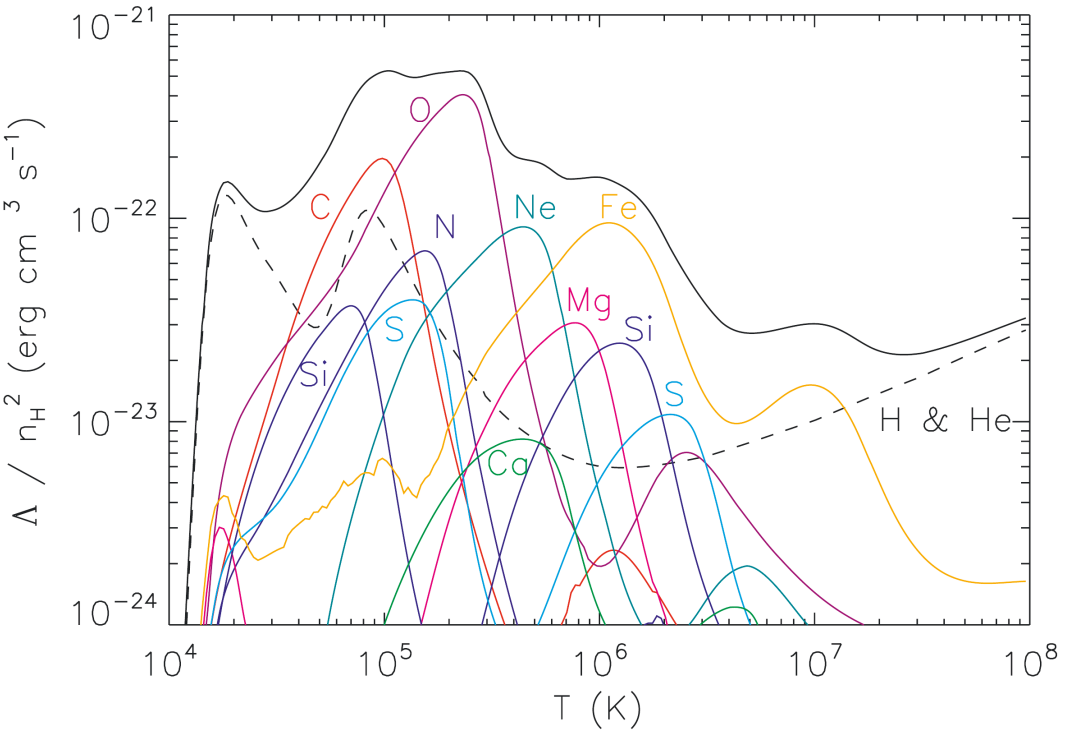

Figure 3.4: The primordial (dashed black) and solar metallicity (solid black) cooling rates in gas at $n_{\rm H} = 10^{-4}$ cm^{-3}. The contributions from the most common elements are indicated by the coloured lines. Image credit: Figure 14 of Wiersma et al. (2009).

Once the gas reaches the threshold for gravitational collapse, however, star formation itself can be described in fairly simple terms. The expected SFR in a gas element of mass m_g can be estimated using the free-fall time $t_{\rm ff}$ as

$$\mathrm{SFR} = \epsilon_{\rm SF} \frac{m_g}{t_{\rm ff}} \tag{3.13}$$

where $\epsilon_{\rm SF}$ is the star formation efficiency. The free-fall time can be derived from the harmonic oscillator frequency in a spherically symmetric cloud with density ρ as

$$t_{\rm ff} = \sqrt{\frac{3\pi}{32 G \rho}}, \tag{3.14}$$

and is often replaced with a similar estimate of the dynamical time-scale $t_{\rm dyn} \sim (4\pi G\rho)^{-1/2}$. The value of $\epsilon_{\rm SF}$ (a few %) can be determined statistically

from observations. The commonly implemented stochastic star formation scheme converts gas particles during every time step Δt into star particles according to the local density-dependent conversion probability

$$1 - \exp\left(-\epsilon_{\rm SF}\frac{\Delta t}{t_{\rm ff}}\right). \tag{3.15}$$

In detail, the numerical routine samples a uniform random number for each star-forming gas particle (see below) during each time step, compares the random number to the conversion probability (which increases with increasing density), and converts a given gas particle into a stellar particle with the same chemical composition if the probability is exceeded.

What complicates the modelling of star formation is determining what conditions must be satisfied for a gas particle to be able to form stars. The commonly used conditions include a number density threshold (typically $n_{\rm th} \in [0.1, 100]$ cm^{-3}) and a temperature threshold ($T_{\rm th} \sim 10^2$–10^4 K), as well as a requirement for the gas particle to be in a convergent flow. For interstellar gas, the fragmentation conditions can also be approximated using the Jeans length scale or Jeans mass (Jeans, 1902) beyond which the internal pressure cannot resist the self-gravity of a gas cloud. In the simulation the density and temperature thresholds can therefore also be replaced by a so-called Jeans mass criterion

$$M_J = \frac{\pi^{5/2} c_s^3}{6G^{3/2}\rho_g^{1/2}} < M_{\rm th} = N_{\rm th} M_{\rm kernel} = N_{\rm th} N_{\rm kernel} m_g \tag{3.16}$$

where c_s is the local sound speed, $N_{\rm kernel}$ is the number of neighbours in the SPH kernel, and the density and temperature thresholds have been replaced with one free parameter $N_{\rm th}$. Star formation in such a scheme is then allowed according to the local Jeans instability, i.e. only in regions where the gas is sufficiently close to gravitational collapse.

3.2.5 The stellar initial mass function

The evolution of stellar particles, typically with a mass resolution between 10^2–$10^6\,{\rm M}_\odot$, is best followed in a statistical sense using population-averaged feedback models. The stellar population within each stellar particle is most often today described by a Chabrier (Chabrier, 2003) or Kroupa (Kroupa, 2001) stellar initial mass function (IMF) with fixed minimum and maximum stellar masses of the order of 0.08–0.1 $\rm M_\odot$ and 50–100 $\rm M_\odot$, respectively. If the particle mass resolution is close

to the mass of single stars, each particle may even represent individual stars with their masses drawn directly from the IMF. Such high fidelity simulations have been routinely used in ISM studies, in modelling for example the star formation process in single molecular clouds (e.g. Bate et al. 2003; Padoan et al. 2017), but have only recently been demonstrated in galactic-scale simulations (Hu et al., 2017; Emerick et al., 2019).

3.3 The stellar feedback cycle

Stellar particles enrich and heat the local ISM by releasing radiation and matter into the surrounding gas particles. The release rates typically depend on the mass and metallicity of the particles, as well as the adapted IMF. For the case of a mass resolution close to the mass of single stars, and if the stellar IMF is adequately sampled, stellar feedback can also be resolved from individual stars.

3.3.1 Stellar radiation

The redshift-dependent cosmic UV-background produced by energetic phenomena such as quasars (Haardt & Madau 1996), is typically implemented as a spatially uniform heating mechanism. It is easy to implement because the ISM is assumed to be in ionisation equilibrium and optically thin to the UV-background. Non-uniform stellar radiation has however been shown to also affect the ISM properties and star formation especially when the simulation begins to resolve the scales relevant for the individual feedback processes.

UV radiation and the interstellar radiation field

In the SPHGal implementation of gadget-3, presented by Hu et al. (2016) and Hu et al. (2017), each young star is modelled as an individual source of UV-radiation using the young stellar masses sampled initially according to the Kroupa IMF. The contribution in the energy range $[6 - 13.6\,\mathrm{eV}]$ from each star is summed over a given stellar particle, and the resulting luminosity is propagated into the surrounding medium. At low metallicities, such as in dwarf galaxies or at a high redshift, the dust content of the ISM is low ($< 1\%$ of the gas mass). In such environments, the transfer of radiation through the medium can be propagated using a simple inverse square law together with an optically thin approximation (i.e. optical thickness $\tau \ll 1$). At

the location of a given gas particle, the energy density of the UV-radiation is thus

$$u_{6-13.6\mathrm{eV}} = \sum_i \frac{L_{i,6-13.6\,\mathrm{eV}}}{4\pi c r_i^2} \tag{3.17}$$

where c is the speed of light, r_i is the distance of each contributing star, and $L_{i,6-13.6\,\mathrm{eV}}$ is the luminosity of each star in the range $[6 - 13.6\,\mathrm{eV}]$, obtained from the BaSeL SED-library (Lejeune et al., 1997; Westera et al., 2002). The dust attenuation and gas self-absorption from intervening interstellar matter are accounted for by summing the column densities along a dozen lines of sight. As a result, the stars produce a spatially and temporally evolving interstellar radiation field, which depends on the gas temperature, dust-to-gas ratio, hydrogen number and column density, electron number density, and the distance from each individual UV-source. With respect to the cosmic UV-radiation, the minimum value of the interstellar radiation field can then be set to equal the extragalactic UV-background in the same energy range of 6–13.6 eV.

Photoionising radiation from individual massive stars

Photoionising radiation from young massive stars produces characteristic HII regions around them. HII regions are typically found around O and early-type B stars with effective temperatures of the order of a few 10^4 K (Stasińska, 1990). The size of the fully ionised volume can be approximated as given by the radius where the rate of ionising photons reaches a balance with recombination. The sizes of the fully ionised regions around the massive, photoionising stars in our simulations are thus set according to the so-called Strömgren radius (Strömgren, 1939) as

$$R_\mathrm{S} = \left(3\frac{S_c}{4\pi n_H^2 \alpha}\right)^{1/3} \tag{3.18}$$

where S_c is the rate of ionising photons emitted by each star, n_H is the local number density of hydrogen, and α is the temperature-dependent hydrogen recombination coefficient. The spherical volume within the Strömgren radius around each stellar particle with an initial mass more than $8\,\mathrm{M}_\odot$ (corresponding to effective temperatures of $\gtrsim 2.5 \times 10^4$ K, Eker et al. 2015) is consequently heated to 10^4 K and set to be fully ionised.

The approximation above works well for a single massive star, while multiple nearby HII regions need to be handled iteratively to prevent double counting and to ensure the assumed ionisation equilibrium.

3.3.2 Supernovae and stellar winds

Type II Supernovae

In the most commonly adopted stellar initial mass functions, described by Chabrier and Kroupa IMFs, approximately 20% of the stellar mass is locked in stars with masses in excess of $8\,M_\odot$ (Kroupa et al., 2013). These massive stars end their lives as core-collapse supernovae. We refer here to all core-collapse events as type II supernovae (SNII) as we do not model the characterising factors such as the detailed pre-supernova evolution and binarity required to differentiate between the core-collapse sub-categories (Ertl et al., 2016). Statistically, there can occur one or two SNII events for every $100\,M_\odot$ of stellar mass formed (and only one if the maximum adapted stellar mass is $50\,M_\odot$), i.e. at a mass resolution of $10^4\,M_\odot$ each new stellar particle will on average release 100 SNII events. Up to 12% of the mass in stars more massive than $8\,M_\odot$ returns to the ISM in the form of SNII enrichment (Woosley & Weaver, 1995; Chieffi & Limongi, 2004).

The procedure used for the SNII energy injection depends on the mass resolution of the simulation. Each SNII event releases a canonical amount of energy, 10^{51} erg (e.g. Janka 2012), with an outflow velocity of the order of 3000–4000 km s^{-1}. The SNII explosions from a massive stellar population may consist of multiple simultaneous SNIIe, and the typical energy for example released from a $10^5\,M_\odot$ particle equals to 10^{54} ergs. The stellar age at which the SNII explosion takes place can be either calculated directly as the stellar lifetime based on the mass of a single stellar particle (Georgy et al., 2013) given that the IMF is sufficiently sampled, or set beforehand as e.g. 3 Myr in the case of poor mass resolution ($\gg 1\,M_\odot$), corresponding to the typical stellar age of the most massive SNII progenitor stars.

The SN energy is released into the surrounding gas, either injected as pure thermal energy (resolved, single SNII) or using a radially varying fraction of kinetic and thermal energy (unresolved). At baryonic particle masses of $\gg 1\,M_\odot$ the energy released by a single SNII is radiated away too rapidly by the massive gas particles, which leads to artificial over-cooling. In such a case, the expansion of a supernova remnant is modelled as a combination of three phases; the momentum conserving free expansion phase with only kinetic injection and no cooling, the Sedov-Taylor phase with 70% of the energy injected as thermal and 30% as kinetic, and the snowplough phase which adds to the Sedov-Taylor phase cooling and a radially increasing escape fraction for the feedback energy. At a particle mass resolution close to a solar mass, the SNII feedback is considered resolved (Hu et al., 2016). In the case of such high-resolution simulations, the SNII energy can therefore be injected directly as purely thermal energy, and the different phases of the evolution of the supernova remnants

emerge naturally as directly calculated by the GADGET-3 code.

The modelled SNII events also enrich the surrounding ISM with metals. The explosive yield depends on the metallicity and the mass of the exploding star (Woosley & Weaver, 1995; Chieffi & Limongi, 2004), independent of whether the event is from an individual massive star or a collection of SNII events. The supernova material is released into the SPH kernel around the exploding particle, distributed either according to the SPH kernel function, a spline function, or equally between the receiving particles. In some cases, especially with the kernel-averaged distribution of the ejecta and when the gas mass resolution is of the order of solar masses, the gas particles nearest to the explosion may therefore receive more than their original mass in the form of enriched matter.

Supernova type Ia

Type Ia SN events are modelled in GADGET-3 with a statistical approach whereby the ejected material is released periodically using a delay-time distribution. The release rate decays as $\sim t^{-1}$, i.e. inversely proportional to the age of the stellar population assuming it formed in a single burst (Maoz et al., 2012). Each $10^3\,\mathrm{M}_\odot$ of new stellar mass produces on average two type Ia supernovae (Maoz & Mannucci, 2012). The method begins to release SNIa feedback after a given star particle reaches an age of 50 Myr (Maoz et al., 2011, 2012), and continues to eject matter every 50 Myr with a decreasing yield according to the delay-time distribution. Each SNIa ejection is distributed across the neighbouring particles weighted by the SPH kernel, and the total element release rates per each SNIa are taken from Iwamoto et al. (1999). The released matter transfers momentum as kinetic energy to the surrounding gas with a similar outflow velocity as in the SNII model.

As the SNIa events only occur once per every $500\,\mathrm{M}_\odot$ of newly formed stellar mass and release energy and metals with a considerable delay-time compared to the SNII events, the supernova feedback energies probed in the highest resolution simulations are dominated by the SNII feedback. The dwarf galaxy mergers presented here, for example, form stars at a relatively low rate from $10^{-4}\,\mathrm{M}_\odot\,\mathrm{yr}^{-1}$ to $0.1\,\mathrm{M}_\odot\,\mathrm{yr}^{-1}$, which would then start to gradually release SNIa feedback tens of Myrs past the time-interval of our current interest. At the moment we thus only consider the core-collapse type supernova feedback in the highest resolution simulations.

Asymptotic giant branch stars

As the stellar particles age, less energetic feedback modes continue to release

matter and energy for example in the form of stellar winds. The wind produced by the asymptotic giant branch (AGB) phase, i.e. the final nuclear-burning phase of practically all stars in our simulations except those which will explode as SNII (Herwig, 2005), is modelled in GADGET-3 using a similar statistical approach as in the SNIa feedback. The kinetic energy in the gradual AGB-wind is given by the outflow velocity of only 25 km s^{-1}, and the mass release rates, which depend on the stellar metallicity, are taken from Karakas (2010).

4 Simulation setup, output, and post-processing

In this Chapter we will briefly review the simulation setup and the data products of our simulations. The outputs from the simulations are snapshots, produced at a desired output interval. The snapshots contain all relevant variables for each particle and are stored along with the positions given in three dimensions. Observations, on the other hand, are commonly subject to projection effects and only provide results in two dimensions, with the three-dimensional structure (when possible) inferred only indirectly. To be certain that we compare apples with apples, the simulation output needs to be reduced while imposing similar limitations as if we were observing real objects. For this a large variety of tools both from the observational and modelling communities are available for us to utilise.

4.1 Initial conditions

4.1.1 The galaxy components

The results of a numerical simulation are largely determined by the input data, the physical models included in the simulation code, and the set of parameters used to configure the code. Galaxy merger simulations are typically constructed with galaxy mass ratios in the range of 1:1 to 1:10. The encounters are initially set as parabolic orbits, and the galaxies are originally in dynamical equilibrium. The initial setup ensures full control of the initial parameters, and allows for easy generation of parameter studies where each detail of the initial system can be straightforwardly adjusted.

The initial conditions used in this thesis span the range from gas-rich, low-mass dwarf galaxies, through Milky Way-like disk galaxies, to massive early-type galaxies which also contain supermassive black holes. In addition to the dominant dark matter haloes, the initial conditions for disk galaxies typically consist of gaseous and stellar disks, and stellar bulges. Early-type galaxies, on the other hand, are

characterised by a spherically symmetric isotropic stellar bulge component. The dark matter density distribution and the stellar bulges are typically set up with Hernquist profiles (Hernquist, 1990), defined using the total mass M and scale radius a as

$$\rho(r) = \frac{M}{2\pi} \frac{a}{r(r+a)^3}. \tag{4.1}$$

In the case of dark matter, the Hernquist profile declines more steeply at large radii compared to the NFW profile (Section 2.7). The parameter a can be expressed using the NFW scale radius r_s and the concentration parameter c as

$$a = r_s \sqrt{2[\ln(1+c) - c/(1+c)]} \tag{4.2}$$

(Springel et al., 2005a). The Hernquist profile converges to a finite mass as r approaches infinity, which makes it numerically convenient.

The disk component is somewhat more complicated to set up due to its rotational support which is set up by distributing a fraction of the angular momentum of the dark matter halo to the disk. This fraction is typically equal to the disk mass fraction, i.e. of the order of a few per cent (see e.g. Chapter 2.1.1). As a result the scale length of the stellar disk is set by the angular momentum of the disk (J_d) through

$$J_d = 2\pi \int_R \Sigma(R)\, R^2\, V_c(R)\, dR = M_d \int_0^\infty V_c(R) \left(\frac{R}{h_d}\right)^2 e^{-R/h_d} dR \tag{4.3}$$

assuming an infinitesimally thin disk with a total mass M_d and an exponential surface mass density

$$\Sigma_d = \frac{M_d}{2\pi h_d^2} e^{-R/h_d} \tag{4.4}$$

as in Eq. 2.6. The circular velocity can in Eq. 4.3 be determined from

$$\begin{aligned} V_c^2 =& \frac{G(M_d(<R) + M_{\rm DM}(<R))}{R} + \\ & \frac{2GM_d}{h_d} \left(\frac{R}{2h_d}\right)^2 \left[I_0\left(\frac{R}{2h_d}\right) K_0\left(\frac{R}{2h_d}\right) - I_1\left(\frac{R}{2h_d}\right) K_1\left(\frac{R}{2h_d}\right) \right] \end{aligned} \tag{4.5}$$

(Springel et al., 2005a), where the first term is the traditional circular velocity due to the enclosed disk and dark matter mass. The second term is comprised of the modified Bessel functions of the first and second kind, I and K, respectively. The vertical structure of the disk is set with a $\mathrm{sech}^2(z/z_d)$ function according

to observations with a scale height significantly less than the scale length, e.g. $z_d \sim 0.1 h_d$ (see Chapter 2.1.2).

The gas disk is set up typically with a scale length of a similar size to the stellar disk. The vertical size of the gas disk is in turn calculated iteratively by assuming a gas with density ρ and pressure P (and polytropic index γ) set in hydrostatic equilibrium,

$$\frac{\delta \rho}{\delta z} = -\frac{\rho^2}{\gamma P} \frac{\delta \Phi}{\delta z}, \tag{4.6}$$

where the gravitational potential Φ results from all the matter components. The density in Eq. 4.6 must result in an exponential surface density

$$\Sigma_g = \frac{M_g}{2\pi h_{\rm gas}^2} e^{-R/h_{\rm gas}}, \tag{4.7}$$

while the vertical structure, set by the scale height $h_{\rm gas}$, is iteratively adjusted until both hydrostatic equilibrium and the exponential surface density agree.

Once the matter densities are set, additional observables of interest can be added on top. Because the stellar feedback and gas cooling models depend on factors such as metallicity, the initial values should be set as realistically as possible. In Lahén et al. (2018) and Pawlik et al. (2018) the stellar disks and bulges were for example constructed with stellar age distributions according to Milky Way observations, and the stellar and gaseous metallicities were set to follow a radial distribution similar to the observations of local disk galaxies. As a result the feedback cycle carefully built in the sub-resolution models of GADGET-3 can be fully employed already from the start of the simulation when for example the stellar ages (which set the epoch of the SN events) follow naturally from the age distribution.

4.1.2 The orbital configuration

The initial orbit of the merging system sets the time-scale at which the merger proceeds, as well as the strength of tidal effects in the close encounters. The initial parameters defining the orbital configuration are divided into parameters which adjust the orbits, and parameters which set the galaxy orientations. In the case of a merging system of two galaxies, the pericentric separation r_p, the initial separation $r_{\rm sep}$ and the initial velocities $v_{\rm init}$ determine the early evolution during the merger, i.e. how strong the first encounter is, how long it takes for the first passage to occur, and what the interval between the subsequent close passages is. The pericentric separation is typically set at a couple of times of the disc scale length in order to produce a fairly strong tidal interaction during the first passage. The inclination i

and the pericentric argument ω, set separately for both of the galaxies, give their mutual orientations and define whether the interaction is co- or counter-rotating. Fig. 4.1 illustrates the parameters needed in configuring the initial orbit.

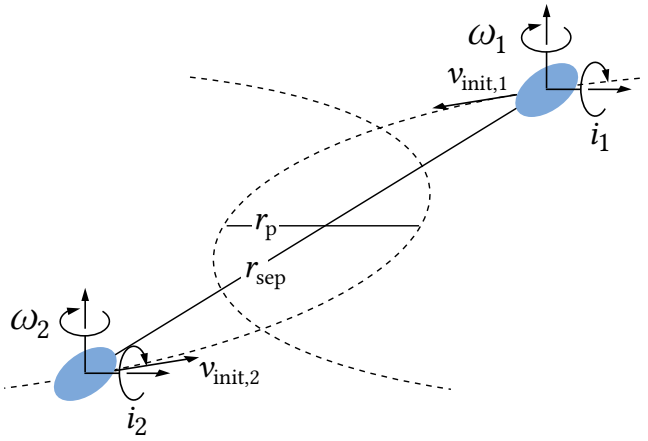

Figure 4.1: An illustration of the orbital parameters used in setting up the initial conditions for a merger simulation of two galaxies numbered 1 and 2. The initial separation r_{sep}, pericentric separation r_p and the initial orbital velocities v_{init} set the early evolution of the merger, while the inclination i and argument of pericentre ω define the initial orientations of the galaxies with respect to the orbital plane.

4.2 Photometry from evolved stellar particles

Observations of galaxies are mostly based on stellar photometry, where the astrophysical properties of galaxies are inferred from the integrated spectra of all stars in the object of interest. A similar analysis needs to be performed on the simulation output: the stellar masses, metallicites and ages need to be converted into a stellar spectrum and integrated in a similar fashion using a simulated instrument, as is done in the observations.

4.2.1 Integrated spectra from single stellar populations

The standard technique is to use spectral templates which provide the wavelength dependent flux from a stellar particle, or a population of particles, as a function of its age and metallicity, normalised to its mass. Such templates, referred to as stellar

population synthesis models, are available for example in Bruzual & Charlot (2003) and Conroy et al. (2009). These libraries typically use single stellar populations (SSP), where all stars in the population are assumed to have formed at the same time in calculating the synthetic spectrum emitted by the entire population. The synthetic spectra are based on models which follow the detailed evolution of different types of stars (e.g. the Padova tracks of Girardi et al. 2000) combined with models of the individual emission from a certain type of a star (e.g. Lejeune et al. 1997). These models are very complex and are constantly being updated.

Most commonly, in order to compare to observations, the entire simulated stellar population is either simply integrated using one single spectrum per galaxy, or projected onto a two-dimensional grid of spectra using for example the spatial resolution of an observational instrument.

4.2.2 Dusty radiative transfer: SKIRT

A further complexity arises as the stellar light travels through space. Intervening gas and dust absorb and re-emit the light, affecting the wavelength dependent intensity. Observations of objects at cosmological distances are also affected by the cosmological surface brightness dimming and redshift due to the expansion of the Universe. In addition, instrumental effects, such as the pixel scale and the filter transmission profile, as well as the Earth's atmosphere, smooth out and restrict the accessible data to only certain wavelengths.

For interstellar dust, the simplest approach would be to apply a simple dust screen to the stellar spectrum, to account for e.g. the dust in a stellar birth cloud. Such models, like the wavelength dependent attenuation model presented in Charlot & Fall (2000), can be easily applied once the stellar spectrum (be it globally integrated or spatially resolved) is known. However, such an approach does not take into account the morphology of the interstellar medium in the system at hand, which is an especially important factor in the study of galaxy mergers.

For resolved studies of interacting galaxies, more sophisticated methods, such as full radiative transfer, are used instead. The processing of the stellar spectrum can be done in a resolved fashion using for example Monte Carlo radiative transfer, in order to model the transmission of the stellar light all the way from a stellar particle to a mock instrument.

In this thesis work we use the radiative transfer code SKIRT (Camps & Baes, 2015) which can utilise different types of simulation outputs, and includes various models for the assumed dust content. SKIRT takes as input the positions, masses, ages and metallicities of stellar particles and asks the user to give the details of the 3D and

2D grids it uses to produce the output data. The emitted stellar spectrum is first integrated using a SSP model, such as provided in Bruzual & Charlot (2003), which is then propagated toward the specified observer using a Monte Carlo method. The radiative transfer calculation can use a specified hierarchical 3D dust grid created from the distribution of gas particles, using for example a spatial octree to refine the Monte Carlo paths according to the local gas density.

Special attention is paid to the young star-forming regions, which in the case of a low resolution simulation are not fully resolved. The typical structure of the nearby ISM around a young star-forming region consists of the ionised HII region and the photodissociation region (PDR). The smallest radii around young stars are dominated by ionised matter at a temperature of 10^4 K and the dissociation front at a few 100 K, which separates the regions of neutral and molecular hydrogen. UV-radiation from the young stars gets absorbed in the PDR region and re-emitted at infrared wavelengths. We account for the regions around the young stars by resampling the matter in these regions and by using a special spectral library for their emission. Following Camps et al. (2016), the cold or star-forming gas particles and star particles younger than 10 Myr are grouped and redistributed according to an observational mass function of the form $N \propto M^{-0.8}$ (Heithausen et al., 1998; Kramer et al., 1998) in the mass range of $700\,\mathrm{M}_\odot \leqslant 10^6\,\mathrm{M}_\odot$. These new particles get separate SEDs from a spectral library calculated originally with the MAPPINGSIII code (Groves et al., 2004, 2008), readily available in SKIRT. The MAPPINGSIII library accounts for the emission from the HII regions and the photodissociation regions, and the spectra can then be processed with the radiative transfer routine along with the radiation from the older stars.

The emitted light which has passed through the interstellar matter is then integrated using a 2D grid, resembling a CCD camera, and the result is a FITS-file similar to real observational data. The FITS-file contains the 2D data cube, with a 2D map at each wavelength specified in the SKIRT input. The data cubes can be combined to give a spectral energy distribution (SED) in each pixel. These spectra can then be convolved with the transmission curve of a given instrument, the result being the filtered flux in a few bands, again corresponding to an observational instrument.

The simulated surface brightness distribution can for example in the outer regions of merger remnants extend far beyond the sensitivity limit of observational instruments (see e.g. Lahén et al. 2018). To make the analysis process of the simulated images more realistic, a background noise component can be added on top of the synthetic signal. In the SDSS data, for example, the typical sky noise is detected at a level of 23 mag arcsec^{-2} in the r-band (Pawlik et al., 2018),

which sets a sensitivity limit at which extended objects can be separated from the background. Adding an observationally realistic noise component to the simulated images straightforwardly restricts the analysis of the synthetic data to the spatial regions relevant when comparing to observations.

Fig. 4.2 shows an example of mock colour composite images of the simulated Antennae galaxies (NGC 4038/4039) studied in Lahén et al. (2018), produced using methods described in this Chapter. The top row in Fig. 4.2 has been constructed using identical Hubble Space Telescope (HST) ACS/WFC F435W, F550M and F814W filters (shown in blue, green and red), except for the additional F658N (H_α +[NII]) filter in the top left image shown in pink. The bottom row uses HST filters converted to Johnson-Cousins $U + B$, V and I bands (shown in blue, green and red, respectively). The tidal tails in the top row span ~ 100 kpc across while the nuclei of the interacting disk galaxies depicted in the bottom row are separated by ~ 7 kpc.

4.2.3 Observational parameters: GALFIT

Once the simulation data has been reduced into an integrated flux, the following steps are exactly the same independent of whether the data is from real observations or numerical simulations. The projected images can be analysed with publicly available software such as DS9 by NASA (Joye & Mandel, 2003), IRAF (Tody, 1986), PyRAF[1], or in our case, GALFIT by Peng et al. (2010).

GALFIT is a photometric least-squares fitting tool which takes FITS-files as input, together with a set of initial parameters which are used to constrain the fitted model. GALFIT can be used to fit a variety of surface brightness profiles from simple one-dimensional axisymmetric radial profiles to highly complex compositions of an arbitrary number of differently oriented two-dimensional profiles, as well as coordinate rotations to allow for spiral arms. The algorithm can optionally take an image with the pixel-to-pixel Poisson-errors and a map of bad pixels which should be excluded from the fitting routine. The software outputs both the model parameters, their uncertainties, as well as the final two-dimensional models as FITS-files and their residuals compared to the input data.

The input for GALFIT must be in realistic flux-units, which is typically for observational data physical magnitudes per square arcsecond in a specific filter. The initial parameters, the pixel scale, the zero-point flux (magnitude), and some practical information related to the data (i.e. gain and exposure time in the FITS-header) in the image must be set to consistent values with respect to the input

[1]PyRAF is a product of the Space Telescope Science Institute, which is operated by AURA for NASA.

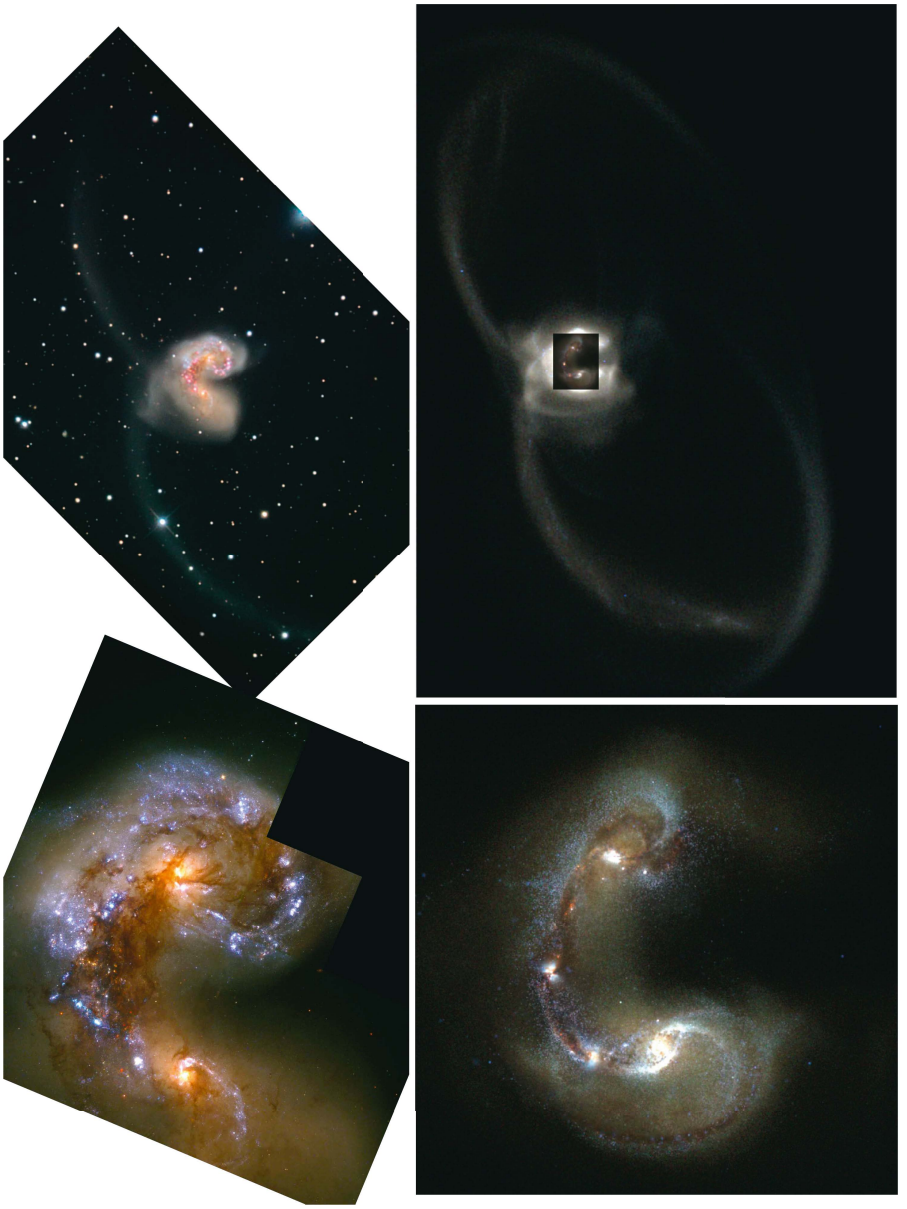

Figure 4.2: Examples of mock colour composite images (right column, see text for details) compared to real observations of the Antennae galaxies (NGC 4038/4039) from The Hubble Legacy Archive (top left) and from Whitmore et al. (1999) (bottom left). The inset in the top right panel depicts the region in the bottom right panel, while the tidal tails have been saturated for visibility. Image credit: Figure 4 of Paper I.

data itself. The input, in other words, must be in observational units (such as mag arcsec^{-2} in r-band) which is why we need to perform all the previous steps in the post-processing procedure to obtain observationally consistent results.

4.3 Kinematic profiles: the simulated LOSVD

As mentioned in Section 2.3.2, the kinematic properties of galaxies can provide information of their formation histories. Similar to observational kinematic analysis, we can derive for example the dimensionless angular momentum parameter λ_R (Eq. 2.13) from the simulation output using the simulated line-of-sight velocity information.

From the numerical simulations we get the full phase-space information which needs to be reduced to quantities such as the mean velocity and the velocity dispersion (Eq. 2.12) similar to what would be obtained from an observed spectrum. The main procedure is simply to replace fitting the velocity information encoded in the spectrum with fitting the true LOS properties of a collection of particles to obtain the simulated pixel-by-pixel LOSVD.

Firstly, most of the present-day numerical simulations are still run with mass resolutions where single point-mass particles represent for example entire star clusters. We follow Naab et al. (2014) who introduced a method to distribute the particles into larger spatial regions by dividing each particle into tens of pseudo-particles with a two-dimensional Gaussian distribution and identical LOS velocity with the original particle. The standard deviation of the spatial pseudo-particle distribution is set as the gravitational softening length. The new particle data are then binned into Cartesian pixels, similar to the pixel-by-pixel IFU-data. The pixels are further binned into cells with equal number of pseudo-particles per cell according to the same Voronoi-tessellation method of Cappellari & Copin (2003) typically used in observations with low signal-to-noise ratios. The pseudo-particle distribution can then be fit with a Gaussian LOSVD complemented with non-Gaussian deviations such as the Gauss-Hermite coefficients as was discussed in Chapter 2.3.2. The resulting two-dimensional velocity maps can be used to derive parameters such as the λ_R profile as described in Chapter 2.3.2. The simulated LOSVD maps can be produced for example along the entire evolutionary sequence of merging galaxies and any interesting features can be traced back to the underlying stellar population and the related astrophysical processes.

4.4 Identification of star clusters

As discussed in Section 2.4.3, gas-rich galaxy mergers are the formation sites of the most massive star clusters in the present-day Universe. In order to assess the process of star cluster formation in our simulations, we need a procedure for identifying the cluster population. The advantage in the simulation output lies in the fact that we have the full three-dimensional information of every particle, as opposed to observations where the information is always provided as a projection along the line-of-sight. We can utilise the simulation output to extract the true population of bound stellar structures within the evolving galaxies. The clusters can also be traced back to their formation sites, and we can follow the interplay between the young star clusters and the gas structures during the merger, which would in observations mostly be obscured by the gas and dust of the star formation environment.

GADGET-3 includes a couple of built-in methods for the search of bound groups of particles; the friends-of-friends (FoF) and the sub halo finder SUBFIND algorithms (Springel et al., 2001a; Dolag et al., 2009). The methods were originally developed for the study of dark matter structures in cosmological simulations, but we apply them to the newly formed population of stellar particles and use the identified structures in following the formation and evolution of the bound star clusters.

The principles used in the cluster identification can be summarised as follows: FoF finds particle groups by searching for linked particles, and SUBFIND identifies the particles bound gravitationally to each group, while distinguishing also bound subgroups within a FoF group. The FoF group is built first by linking particles within a maximum distance given by a linking length l, where the group must typically contain at least a few tens of members depending on the mass resolution. The name of the algorithm comes from the fact that all the connected particles are part of the group, even though not all are connected to one another by the linking length. The value of l is typically set as a fraction (e.g. 20%) of the mean separation between all particles under consideration. The structures found with FoF may be spherical, but they may as well be linear as long as the particles are connected; thus a more sophisticated method, such as SUBFIND, is used together with FoF to exclude structures which are not of interest to us.

The 3D particle data is fully utilised in the SUBFIND routine. The FoF group is used as a starting point for the identification of the subgroups, which are local overdensities within the FoF group. The self-bound mass, i.e. the particles with negative total energy with respect to the local mean velocity and the position of the most bound particle are then searched for. The algorithm works from low to high densities, starting from the largest subgroup which typically includes most of the

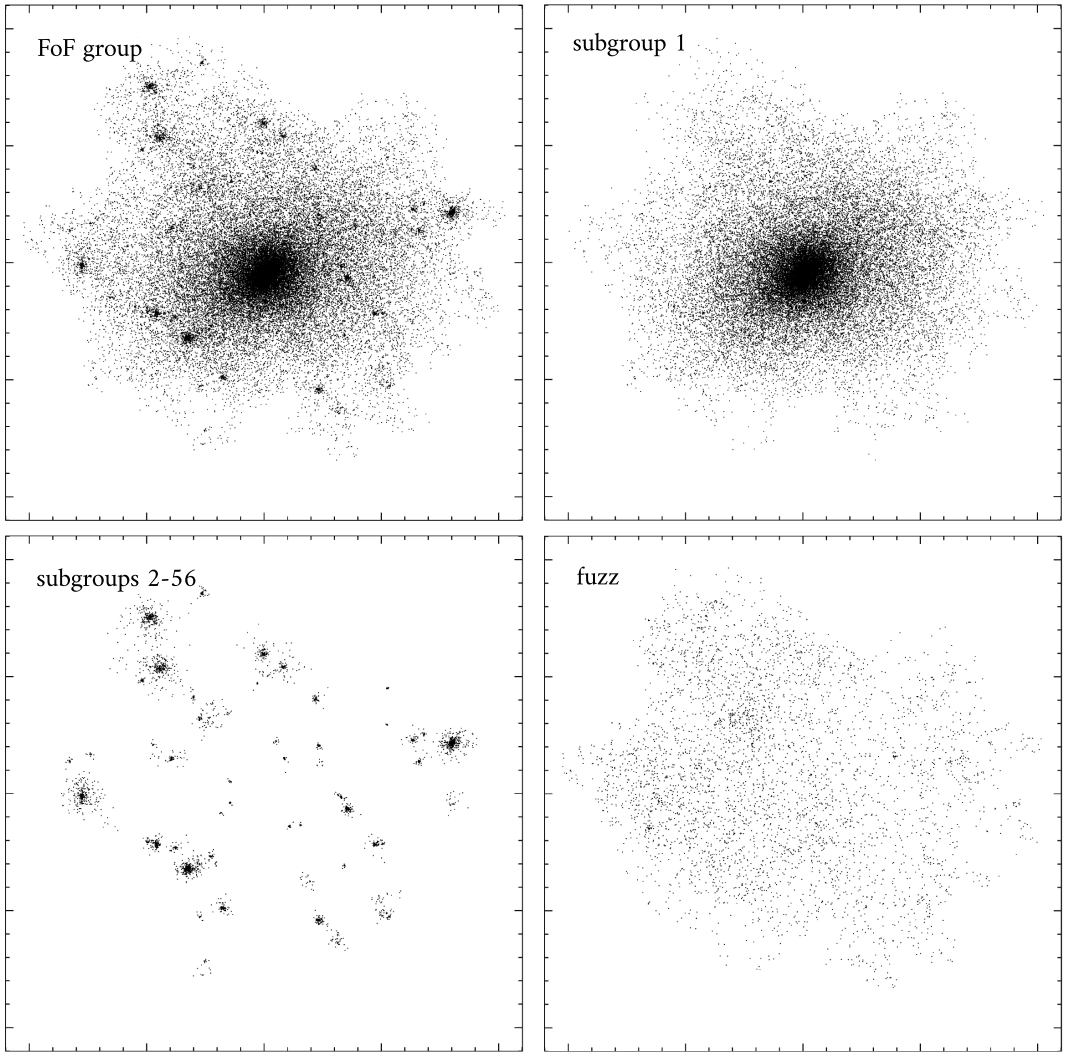

Figure 4.3: The components of the FoF and Subfind analysis shown in the case of a dark matter FoF group (top left), its main halo (top right) and its 55 subgroups (sub haloes, bottom left) in a box of a side length of ~ 3 Mpc. Particles appearing in the top left panel but not bound to any of the subgroups are fuzz, shown in the bottom right panel. Image credit: adapted from Springel et al. (2001a).

particles in the original FoF group. In this scheme, particles may at first belong to multiple over-lapping overdensities, and the distinction into separate structures is done by calculating the total energy of each particle one subgroup at a time. The last subgroup that each particle is bound to is set as its host, which means that each particle is set as a part of the densest bound local structure (i.e. the last subgroup that it was bound to). Particles which are part of the FoF group but not bound to any of the subgroups are stored as part of the FoF-data structure and called *fuzz*.

Fig. 4.3 illustrates the different components of the FoF/Subfind analysis performed on a dark matter halo in a cosmological simulation. The original FoF group is shown in the top left panel, the first and least dense subgroup on the top right, and the consecutive subgroups are shown in the bottom left panel. The bottom right panel shows particles defined as fuzz. If the particles shown in Fig. 4.3 were stellar particles, the top right panel could be thought of as the main stellar component (e.g. disk) in the galaxy. The subgroups in the bottom left panel could then be considered as star clusters, and in this case only the structures shown in the bottom left panel would be included in the further star cluster analysis.

4.5 Summary of the pipeline

As described in this Chapter, the steps from the initial conditions to observationally consistent parameters are numerous and depend on the specific observables under study. Fig. 4.4 collects in a flowchart the typical pipeline used in this thesis to obtain the different observational parameters. The top part of Fig. 4.4 includes the initial setup with the initial conditions, their stability (e.g. initial turbulent driving with SN feedback but excluding self-gravity), and the numerical simulations, discussed in Chapters 3 and 4.1. The bottom part of Fig. 4.4 depicts the post-processing pipeline from the snapshots to the observational parameters using the methods described in Chapters 4.2–4.4.

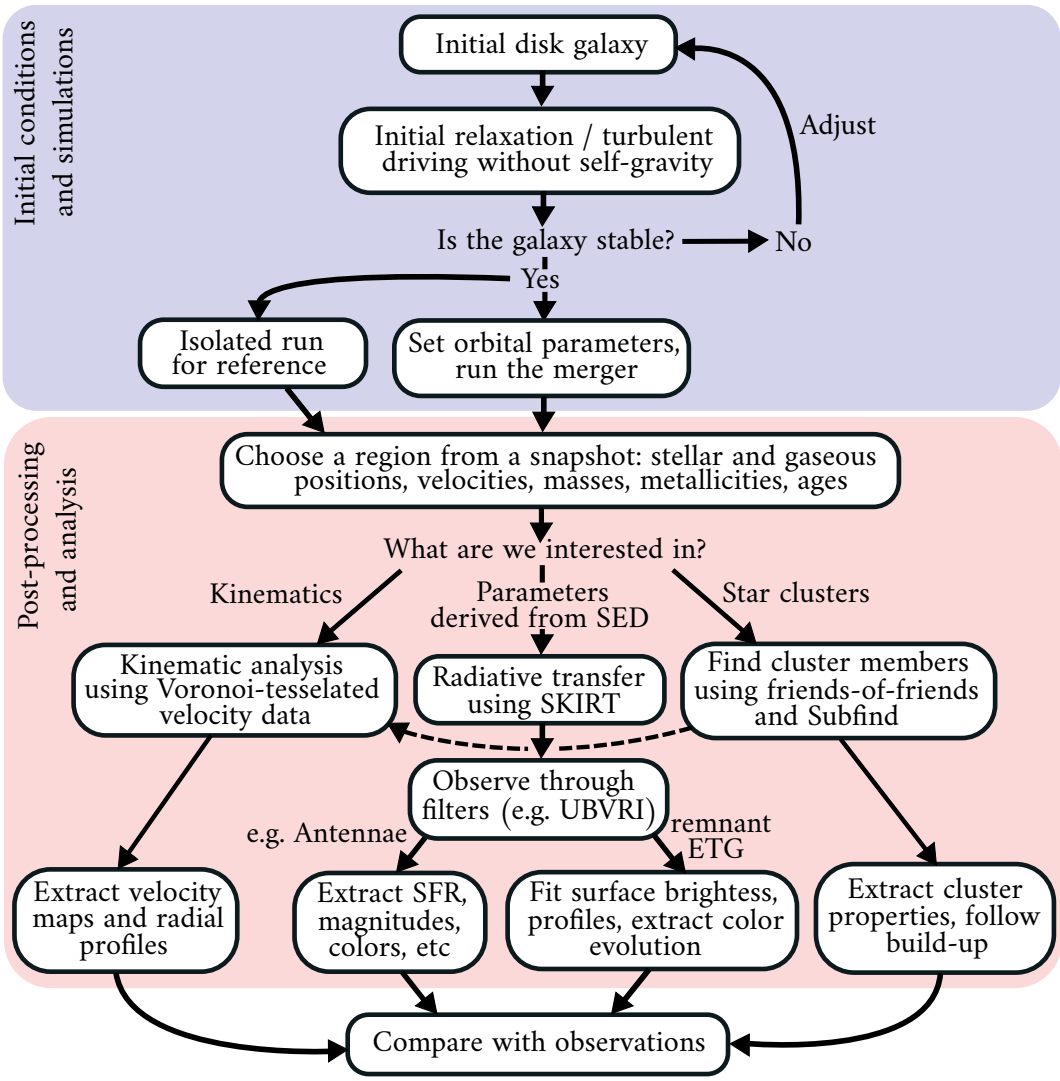

Figure 4.4: A summary of the steps needed between the set up of the initial conditions and the comparison of the simulated results to observational parameters.

5 Summary of the publications

This thesis consists of five publications. All articles are peer-reviewed journal articles and published in the Monthly Notices of the Royal Astrophysical Society, the Astrophysical Journal and the Astrophysical Journal Letters. The papers and the author's contribution are summarised below.

5.1 Paper I – The fate of the Antennae galaxies

Lahén, N., Johansson, P.H., Rantala, A., Naab, T., & Frigo, M., 2018, Monthly Notices of the Royal Astronomical Society, 475, 3934.

The Antennae galaxies (NGC 4038/4039) is the nearest ongoing archetypal merger of two disk galaxies with similar masses. The system has been widely studied in a variety of observational campaigns, which provide highly detailed constraints for the simulations studying the different phases of the ongoing merger. Paper I investigates the spatial and temporal evolution of star formation and the chemical composition in a high-resolution ($10^4\,M_\odot$ per baryonic particle) hydrodynamical simulation designed to reproduce the present-day conditions observed in the Antennae.

In Paper I the simulations were run using SPHGal, an updated version of the standard GADGET-3 simulation code, which introduces several improvements to the hydrodynamical aspects of the standard code. As the idealised merger simulations begin with disk galaxies set up in dynamical equilibrium, variables which affect the intricate feedback processes, such as the stellar ages and the metallicities, need to be carefully initialised. The author updated and calibrated the initial disk galaxy models to include radial Milky Way-like metallicity gradients and star formation histories based on observations of the disk and bulge components of local disk galaxies. The other initial galaxy and orbital parameters were set up based on previous work by Karl et al. (2010).

We followed the entire lifetime of the merging system from the first approach

until 3 Gyr after the coalescence. The simulation enables the study of the Antennae merger as well as its merger remnant in comparison to the observed Antennae and a population of local elliptical galaxies. The simulation output was post-processed using the radiative transfer code SKIRT, which was used to reduce the snapshots into spectral energy data cubes suitable to be mock observed through telescope-specific filters. Such post-processing enables the use of observational data analysis tools, and the resulting mock observations were analysed with the surface brightness analysis tool GALFIT.

Firstly, the best-match simulated Antennae was found by comparing the spectral energy distribution, metallicity, and spatial star formation properties to the observed Antennae. We studied how the metallicity gradient evolved due to the centrally concentrated star formation and how the initial stellar matter was redistributed during the merger. The 3-Gyr-old remnant was shown to evolve into the red and dead region in the observed colour-magnitude diagram. Finally, we produced line-of-sight velocity distribution maps of the simulated merger remnant, and derived the angular momentum parameter λ_R. The surface brightness and kinematic features were compared to the population of local early-type galaxies in the ATLAS^{3D} sample. As a result we introduced the best candidates to represent the possible future fate of the Antennae galaxies.

5.2 Paper II – Formation of low-metallicity globular clusters in dwarf galaxy mergers

Lahén, N., Naab, T., Johansson, P.H., Elmegreen, B., Hu, C.-Y., Walch, S., 2019, The Astrophysical Journal Letters, 879, L18.

Paper II introduces the gas-rich dwarf galaxy merger simulation analysed in Papers II and III. The simulation follows the galactic-scale evolution of two merging dwarf galaxies up to 100 Myr past the disk coalescence. The simulation is resolved at a $\sim 4\,\mathrm{M}_\odot$ baryonic mass resolution and 0.1 pc spatial resolution. As a result, the interplay between the interstellar medium and the stellar feedback processes, such as SNII events, are resolved at a level of individual massive stars. Crucially, we also model the spatially and temporally evolving dust attenuated and gas-shielded stellar UV-radiation field, and the photoionising radiation around the young massive stars.

The high-pressure, low-shear, gas-rich environment of the merging dwarf galaxy system presents opportune conditions for clustered star formation. Hundreds of stellar clusters form at masses which, if observed, would be resolved even outside

of the Local Group. In Paper II we analyse the characteristic properties of the three most massive ($\gtrsim 10^5\,\mathrm{M}_\odot$), long-lived bound stellar clusters formed during the merger. The clusters form hierarchically, each building their central density two to three orders of magnitude above the local gas density, during a time span of a few Myr. The newly formed stars were also shown to be able to deposit supernova feedback energy equalling the binding energy of the gas remaining within the clusters.

We fit the radial stellar surface density profiles of the three clusters with power-law profiles. The best-fit parameters, such as half-mass radius, the central velocity dispersion, and the mean surface density, show how some of the simulated cluster properties become at an age of 100 Myr indistinguishable from present-day globular clusters. The simulation presented in Paper II provides a compelling scenario for the formation and accretion of globular clusters into the haloes of massive galaxies, as the gas-rich low-metallicity conditions of the dwarf merger were ubiquitous in the early Universe.

5.3 Paper III – The GRIFFIN project – formation of star clusters with individual massive stars in a simulated dwarf galaxy starburst

Lahén, N., Naab, T., Johansson, P.H., Elmegreen, B., Hu, C.-Y., Walch, S., Steinwandel, U.P., Moster, B.P., 2019, The Astrophysical Journal, 891, 2.

Paper III describes in detail the simulation introduced in Paper II. We describe the star formation properties of the dwarf merger and analyse the population of young star clusters in great detail.

The star formation environment in the dwarf merger evolves through a wide range of values of thermal pressure, gas density and SFR as the merger proceeds from the first approach, through a few close passages, and past the merger induced starburst. The range spanned by the simulated gas surface density and star formation rate surface density (Σ_{SFR}) correspond almost to the entire range of values in the Kennicutt-Schmidt relation observed in local disk and dwarf galaxies. We tested the impact of imposing observational restrictions such as pixel-by-pixel sensitivity limits, which further improved the agreement with the observations.

We show how the population of young star clusters starts building up already during the first passage with an observationally consistent mass function. The power-law index of the cluster mass function is fit with ~ -1.7 and ~ -2 when using cluster mass cut-offs equal to typical observed completeness limits of $10^{2.5}\,\mathrm{M}_\odot$

and $10^3\,M_\odot$. The mass of the most massive young cluster evolves almost linearly with Σ_{SFR} similarly to what is observed in star-forming systems from the low-mass Magellanic clouds up to the more massive Antennae merger. We also demonstrate how all the young star clusters form with age spreads less than ~ 5 Myr, which sets Paper III among the first published works to successfully reproduce the narrow age spreads observed in the population of young star clusters. The observationally accurate shut-off of star formation in the clusters can be attributed to the detailed modelling of the stellar feedback.

In addition, we discuss in Paper III the connection between Σ_{SFR} and the cluster formation efficiency. Because of cluster destruction, the cluster formation efficiency needs to be inferred from young clusters, while observationally it is difficult to exclude associations and open clusters from the analysis of a young star cluster population. Our analysis on the other hand considers only bound clusters, and we report in Paper III a correlation between Σ_{SFR} and the cluster formation efficiency deriving a relation very similar to what has been analytically predicted for example in Kruijssen (2012). The absolute values in our produced Σ_{SFR} – cluster formation efficiency relation appear slightly higher than the respective observed values, which may be produced by both insufficient modelling of the earliest stellar feedback and the employed cluster selection procedure. The work presented in Papers II and III therefore presents important advances in the modelling of the physical processes necessary for clustered star formation, while leaving room for further improvement.

5.4 Paper IV – The origins of post-starburst galaxies at $z < 0.05$

Pawlik, M. M., Taj Aldeen, L., Wild, V., Mendez-Abreu, J., **Lahén, N.**, Johansson, P. H., Jimenez, N., Lucas, W., Zheng, Y., Walcher, C. J., Rowlands, K., 2018, Monthly Notices of the Royal Astronomical Society, 477, 1708.

Post-starburst galaxies (PSBs) are galactic systems in which the star formation has been quenched either momentarily or entirely. The majority of observed PSBs are found to inhabit the so-called green valley of the colour-magnitude diagram between the star-forming galaxies (blue cloud) and the red and dead quiescent galaxies (red cloud). A common cause for the transition is a gas-rich major merger, where the merger-induced star formation exhausts the gas reservoir and quenches the star formation. Other means of achieving PSB features in galaxies not undergoing a major merger include for example excursions out of the blue cloud due to internal

instabilities and out of the red cloud due to gas-rich minor mergers.

The aim of Paper IV is to quantify the fraction of post-starburst galaxies resulting from these different evolutionary paths using various indicators for their identification. PSBs are characterised in observational surveys by their spectral features as having strong hydrogen Balmer absorption lines from A-type stars together with little or no emission lines indicative of star formation. The role of active galactic nuclei is investigated as well, as the feedback due to the central supermassive black hole poses another highly temporally fluctuating mechanism for quenching.

In Paper IV we study an observational sample of 189 galaxies with PSB features and draw conclusions of their origins and evolutionary paths, comparing to a control sample of star-forming and quiescent galaxies. The observed galaxies were first divided into four groups based on their spectral features; emission-line PSBs (presence of H_α emission), dusty PSBs (H_α emission and dust, a subset of the emission-line PSBs), PSBs with AGN, and quiescent PSBs (no features other than strong Balmer absorption). For these four sets of post-starburst galaxies, their star formation histories, morphological features, and local environment were classified. Additional insight into the lifetime of the morphological features was provided by numerical major merger simulations.

A strong starburst followed by abrupt quenching, such as is characteristic for a gas-rich major merger, was concluded to be the cause for the PSB phase in the majority (60% at $M_* > 10^{10.5}\,\mathrm{M}_\odot$ and 70% at $M_* < 10^{10.5}\,\mathrm{M}_\odot$) of the 189 galaxies in the study. The rest of the low-mass ($M_* < 10^{10.5}\,\mathrm{M}_\odot$) PSB galaxies, typically found in the blue cloud, show stochastic bursts of star formation followed by a return to the blue cloud. Similarly, the rest of the high-mass ($M_* > 10^{10.5}\,\mathrm{M}_\odot$) PSBs build their mass through accretion and weak bursts of star formation as they evolve along the red cloud. Based on the star-formation histories, morphologies and environments of the PSBs in the four sets, the evolutionary sequence of low- and high-mass PSBs was introduced.

5.5 Paper V – Post-Newtonian dynamical modeling of supermassive black holes in galactic-scale simulations

Rantala, A., Pihajoki, P., Johansson, P.H., Naab, T., **Lahén, N.**, & Sawala, T., 2017, The Astrophysical Journal, 840, 53.

The observed correlation between the mass of the central supermassive black hole (SMBH) and the mass of the galactic bulge is one of the most fundamental

galaxy-scale relations. Due to the hierarchical nature of galaxy evolution, mergers of galaxies which build up the present-day early-type galaxies are common especially toward redshifts of $z > 1$. In this scenario, newly formed early-type galaxies are built with pairs of SMBHs, which evolve rapidly through three main phases. First, the SMBHs migrate toward the central region of the merger remnant via dynamical friction. After the SMBHs form a binary, their mutual evolution proceeds through three-body encounters where the binary loses orbital energy to the population of stars on suitable close orbits called the loss-cone. The third and final phase begins once the binary has shrunk to a size where gravitational waves can kick in – this phase leads to the coalescence of the SMBHs. Earlier simulation work has suggested an alternative for this scenario according to which the loss-cone can get depleted and drag forces from gas would be required for the SMBH binaries to be able to shrink down to the gravitational wave phase.

In order to simulate the three-phase evolutionary process of SMBH binaries in detail, we developed in Paper V the KETJU module – an extension to GADGET-3 which allows us to model the dynamical evolution of SMBHs in a full galactic setting. The new module introduces sub-regions around SMBHs, where the interactions between the SMBHs and the surrounding stars are calculated at high numerical accuracy using the AR-CHAIN algorithm. The main features in AR-CHAIN are the use of chained interparticle vectors, and time-transformed equations of motion solved using a specialised extrapolation method. The equations of motion of the SMBHs are supplemented with post-Newtonian terms, which enable the emission of gravitational waves and the final coalescence of the SMBHs at spatial scales of ~ 0.005 pc.

Paper V introduced the KETJU module and demonstrates its accuracy and scalability with detailed numerical tests. The performance of the method was compared against the N-BODY7 and rVINE codes. When combined with the triaxial shapes of the early-type galaxies produced in the suite of 57 high-resolution merger simulations, the three phases of the SMBH binary evolution result naturally without the need of a gaseous component. The binaries were consequently shown to merge on average 200 Myr after their formation, with a strong dependence on the eccentricity of the SMBH binary, as the result of the galaxy mergers.

5.6 Author's contribution to individual papers

- In Paper I the author improved the initial conditions generator, calibrated the new initial conditions, made minor improvements to the simulation code, prepared and executed the galaxy merger and isolated reference simulations,

post-processed the simulation output, and analysed the final results. The author prepared all figures and the first version of the manuscript, with input and comments from P.H. Johansson and T. Naab. The manuscript was commented by all the co-authors.

- In Papers II and III the author made minor improvements to the simulation code, executed the galaxy merger and isolated reference simulations, post-processed the simulation output, and analysed the final results. The author prepared all figures and the first versions of both of the manuscripts, with input and comments by T. Naab, P.H. Johansson and B. Elmegreen. All co-authors commented on both of the manuscripts.

- The author prepared and calibrated the initial galaxy models to be used in the merger simulations for Section 5.1 of Paper IV. The author helped in the set up and execution of the merger simulations, as well as in the development of the post-processing procedures. The author provided comments and took part in the general discussion regarding the manuscript and contributed to the writing of Appendix D.

- In Paper V the author contributed to the development and testing process of the KETJU module by providing expertise regarding galaxy mergers, the initial conditions and analysis of the simulation output in Section 6.3 of the article. The author provided comments during the preparation of the manuscript.

6 Concluding remarks

In this thesis we have provided a review of the astrophysical processes and the observational background relevant for modelling star formation especially in the context of galaxy mergers. The current state-of-the-art numerical simulation methods have also been reviewed, with an emphasis on the post-processing of the simulation outputs. We have demonstrated how the production of realistic mock observations require hydrodynamical simulations with detailed astrophysical models, carefully constructed initial conditions, and detailed post-processing in order to provide an accurate comparison to the observations. The work presented here in terms of the numerical simulations thus demonstrates our ability to accurately reproduce observed results related to the dynamics and star formation during various phases in the evolutionary sequence of galaxies. An example of our success is presented by the match of the metallicity and star formation properties in the simulated Antennae galaxy merger compared with its observed counterpart in Paper I.

The simulations introduced in Papers II and III present for the first time the formation of a realistic population of young star clusters in a dwarf galaxy starburst resolved with individual massive stars. The $\gtrsim 4\,\mathrm{M}_{\odot}$ baryonic mass resolution and 0.1 pc gravitational softening length enable clustered star formation in a star formation environment consistent with observed disk and dwarf galaxies. The gas-rich, low-metallicity initial conditions probe the conditions present in the high-redshift Universe, and therefore allow the formation of massive ($M_{*} \gtrsim 10^{5}\,\mathrm{M}_{\odot}$) low-metallicity objects which evolve to resemble present-day globular clusters.

However, as described in Chapter 3.1.4, globular clusters are gravitationally collisional systems. Their internal dynamical evolution is governed by two-body interactions. The evolution of the massive star clusters simulated in Papers II and III can therefore not be analysed beyond a few crossing times at reasonable accuracy. This sets an upper limit for a meaningful analysis period of a few 100 Myr in the case of our simulated globular clusters.

Paper V, on the other hand, provides the means for simulating very accurate

dynamics within specific spatial regions using the KETJU module together with the galactic-scale simulation code GADGET-3. Combining the simulation techniques presented in Papers III and V would therefore result in a significant numerical breakthrough in terms of globular cluster formation. Such a simulation could be used to model the formation and long-term evolution of massive star clusters at high accuracy while simultaneously following the large-scale evolution of the surrounding galactic environment.

The objectives for the future include both improvements to the astrophysical models in GADGET-3 as well as the use of the KETJU module for simulating the internal dynamics of young star clusters. The feedback implementation in GADGET-3 does not at the moment include for example winds from young stars nor the accretion and feedback from stellar mass black holes. Compact objects, such as neutron stars and black holes which are the remnants of supernova events, behave as collisionless point-mass particles. In addition, stellar mass binaries cannot by construction form in our simulations with softened gravity even though they should according to observations be ubiquitous especially in young star clusters.

At the moment there are at least five publications in preparation related to the already existing high-resolution simulation data. The current work on the project will be continued by the author at the Max-Planck Institute for Astrophysics in Germany as a postdoctoral fellow. The future plan of the simulation project will be two-fold; first, introduce the missing stellar processes outlined above, and second use the SPHGal implementation of GADGET-3 together with KETJU to model the long-term evolution of massive star clusters starting from gas-rich initial conditions. The present situation looks promising and the ultimate goal is to run full cosmological simulations in order to follow the formation of massive star clusters in the high-redshift Universe, and finally decipher the entire lifecycle of globular clusters.

Bibliography

Aarseth, S. J. 1963, Monthly Notices of the Royal Astronomical Society, 126, 223

Adamo, A., Kruijssen, J. M. D., Bastian, N., Silva-Villa, E., & Ryon, J. 2015, Monthly Notices of the Royal Astronomical Society, 452, 246

Appel, A. W. 1985, SIAM Journal on Scientific and Statistical Computing, vol. 6, no. 1, January 1985, p. 85-103., 6, 85

Baldry, I. K., Glazebrook, K., Brinkmann, J., et al. 2004, The Astrophysical Journal, 600, 681

Balsara, D. S. 1995, Journal of Computational Physics, 121, 357

Barazza, F. D., Jogee, S., Rix, H.-W., et al. 2006, The Astrophysical Journal, 643, 162

Barnes, J., & Hut, P. 1986, Nature, 324, 446

Barnes, J. E., & Hernquist, L. 1996, The Astrophysical Journal, 471, 115

Bate, M. R., Bonnell, I. A., & Bromm, V. 2003, Monthly Notices of the Royal Astronomical Society, 339, 577

Behroozi, P. S., Wechsler, R. H., & Conroy, C. 2013, The Astrophysical Journal, 770, 57

Bekki, K. 2009, Monthly Notices of the Royal Astronomical Society, 399, 2221

Bender, R., Doebereiner, S., & Moellenhoff, C. 1988, Astronomy & Astrophysics Supplement Series, 74, 385

Bender, R., & Moellenhoff, C. 1987, Astronomy & Astrophysics, 177, 71

Bender, R., Saglia, R. P., & Gerhard, O. E. 1994, Monthly Notices of the Royal Astronomical Society, 269, 785

Bibliography

Bensby, T., Feltzing, S., & Lundström, I. 2003, Astronomy & Astrophysics, 410, 527

Bigiel, F., Leroy, A., Walter, F., et al. 2008, The Astronomical Journal, 136, 2846

Binney, J., & Tremaine, S. 2008, Galactic Dynamics: Second Edition (Princeton University Press)

Black, J. H. 1981, Monthly Notices of the Royal Astronomical Society, 197, 553

Boissier, S., & Prantzos, N. 1999, Monthly Notices of the Royal Astronomical Society, 307, 857

Bruzual, G., & Charlot, S. 2003, Monthly Notices of the Royal Astronomical Society, 344, 1000

Camargo, D., & Minniti, D. 2019, Monthly Notices of the Royal Astronomical Society, 484, L90

Camps, P., & Baes, M. 2015, Astronomy and Computing, 9, 20

Camps, P., Trayford, J. W., Baes, M., et al. 2016, Monthly Notices of the Royal Astronomical Society, 462, 1057

Capaccioli, M. 1989, in World of Galaxies (Le Monde des Galaxies), ed. H. G. Corwin, Jr. & L. Bottinelli, 208–227

Cappellari, M., & Copin, Y. 2003, Monthly Notices of the Royal Astronomical Society, 342, 345

Cappellari, M., Bacon, R., Bureau, M., et al. 2006, Monthly Notices of the Royal Astronomical Society, 366, 1126

Cappellari, M., Emsellem, E., Bacon, R., et al. 2007, Monthly Notices of the Royal Astronomical Society, 379, 418

Cappellari, M., Emsellem, E., Krajnović, D., et al. 2011, Monthly Notices of the Royal Astronomical Society, 413, 813

Carilli, C. L., & Walter, F. 2013, Annual Review of Astronomy & Astrophysics, 51, 105

Carollo, D., Beers, T. C., Chiba, M., et al. 2010, The Astrophysical Journal, 712, 692

Chabrier, G. 2003, Publications of the Astronomical Society of the Pacific, 115, 763

Chandar, R., Fall, S. M., Whitmore, B. C., & Mulia, A. J. 2017, The Astrophysical Journal, 849, 128

Chandrasekhar, S. 1943, The Astrophysical Journal, 97, 255

Charlot, S., & Fall, S. M. 2000, The Astrophysical Journal, 539, 718

Chiboucas, K., Tully, R. B., Marzke, R. O., et al. 2011, The Astrophysical Journal, 737, 86

Chieffi, A., & Limongi, M. 2004, The Astrophysical Journal, 608, 405

Cole, S. 1991, The Astrophysical Journal, 367, 45

Conroy, C., Gunn, J. E., & White, M. 2009, The Astrophysical Journal, 699, 486

Conselice, C. J., Bershady, M. A., Dickinson, M., & Papovich, C. 2003, The Astronomical Journal, 126, 1183

Cook, D. O., Seth, A. C., Dale, D. A., et al. 2012, The Astrophysical Journal, 751, 100

Cullen, L., & Dehnen, W. 2010, Monthly Notices of the Royal Astronomical Society, 408, 669

Dabringhausen, J., Hilker, M., & Kroupa, P. 2008, Monthly Notices of the Royal Astronomical Society, 386, 864

Daddi, E., Elbaz, D., Walter, F., et al. 2010a, The Astrophysical Journal Letters, 714, L118

Daddi, E., Bournaud, F., Walter, F., et al. 2010b, The Astrophysical Journal, 713, 686

Davé, R., Katz, N., Oppenheimer, B. D., Kollmeier, J. A., & Weinberg, D. H. 2013, Monthly Notices of the Royal Astronomical Society, 434, 2645

Davies, R. L., & Illingworth, G. 1983, The Astrophysical Journal, 266, 516

de Grijs, R., Peletier, R. F., & van der Kruit, P. C. 1997, Astronomy & Astrophysics, 327, 966

de Vaucouleurs, G. 1948, Annales d'Astrophysique, 11, 247

Dehnen, W., & Aly, H. 2012, Monthly Notices of the Royal Astronomical Society, 425, 1068

Dekel, A., & Birnboim, Y. 2006, Monthly Notices of the Royal Astronomical Society, 368, 2

Di Matteo, P., Combes, F., Melchior, A. L., & Semelin, B. 2007, Astronomy & Astrophysics, 468, 61

Dolag, K., Borgani, S., Murante, G., & Springel, V. 2009, Monthly Notices of the Royal Astronomical Society, 399, 497

Dressler, A. 1980, The Astrophysical Journal, 236, 351

Dubois, Y., Pichon, C., Welker, C., et al. 2014, Monthly Notices of the Royal Astronomical Society, 444, 1453

Dutton, A. A., & Macciò, A. V. 2014, Monthly Notices of the Royal Astronomical Society, 441, 3359

Dutton, A. A., van den Bosch, F. C., & Dekel, A. 2010, Monthly Notices of the Royal Astronomical Society, 405, 1690

Efstathiou, G. 1992, Monthly Notices of the Royal Astronomical Society, 256, 43P

Einasto, J. 1965, Trudy Astrofizicheskogo Instituta Alma-Ata, 5, 87

Eker, Z., Soydugan, F., Soydugan, E., et al. 2015, The Astronomical Journal, 149, 131

Elbaz, D., Dickinson, M., Hwang, H. S., et al. 2011, Astronomy & Astrophysics, 533, A119

Elmegreen, B. G. 2018, The Astrophysical Journal, 869, 119

Elmegreen, B. G., & Falgarone, E. 1996, The Astrophysical Journal, 471, 816

Emerick, A., Bryan, G. L., & Mac Low, M.-M. 2019, Monthly Notices of the Royal Astronomical Society, 482, 1304

Emsellem, E., Cappellari, M., Krajnović, D., et al. 2007, Monthly Notices of the Royal Astronomical Society, 379, 401

Emsellem, E., Cappellari, M., Krajnović, D., et al. 2011, Monthly Notices of the Royal Astronomical Society, 414, 888

Ertl, T., Janka, H. T., Woosley, S. E., Sukhbold, T., & Ugliano, M. 2016, The Astrophysical Journal, 818, 124

Fall, S. M., Chandar, R., & Whitmore, B. C. 2005, The Astrophysical Journal Letters, 631, L133

Ferrarese, L., & Merritt, D. 2000, The Astrophysical Journal Letters, 539, L9

Freeman, K. C. 1970, The Astrophysical Journal, 160, 811

Fukugita, M., Hogan, C. J., & Peebles, P. J. E. 1998, The Astrophysical Journal, 503, 518

Geha, M., Blanton, M. R., Yan, R., & Tinker, J. L. 2012, The Astrophysical Journal, 757, 85

Georgy, C., Ekström, S., Eggenberger, P., et al. 2013, Astronomy & Astrophysics, 558, A103

Gerhard, O. E. 1993, Monthly Notices of the Royal Astronomical Society, 265, 213

Gieles, M., Portegies Zwart, S. F., Baumgardt, H., et al. 2006, Monthly Notices of the Royal Astronomical Society, 371, 793

Gilmore, G., & Reid, N. 1983, Monthly Notices of the Royal Astronomical Society, 202, 1025

Gingold, R. A., & Monaghan, J. J. 1977, Monthly Notices of the Royal Astronomical Society, 181, 375

Girardi, L., Bressan, A., Bertelli, G., & Chiosi, C. 2000, Astronomy & Astrophysics Supplement Series, 141, 371

Glover, S. C. O., & Mac Low, M.-M. 2007, The Astrophysical Journal Supplement Series, 169, 239

Grebel, E. K. 2000, in ESA Special Publication, Vol. 445, Star Formation from the Small to the Large Scale, ed. F. Favata, A. Kaas, & A. Wilson, 87

Groves, B., Dopita, M. A., Sutherland, R. S., et al. 2008, The Astrophysical Journal Supplement Series, 176, 438

Groves, B. A., Dopita, M. A., & Sutherland, R. S. 2004, The Astrophysical Journal Supplement Series, 153, 9

Guo, Q., Hu, H., Zheng, Z., et al. 2019, Nature Astronomy, 493

Haardt, F., & Madau, P. 1996, The Astrophysical Journal, 461, 20

Hannon, S., Lee, J. C., Whitmore, B. C., et al. 2019, Monthly Notices of the Royal Astronomical Society, 490, 4648

Harris, W. E. 1991, Annual Review of Astronomy & Astrophysics, 29, 543

Haşegan, M., Jordán, A., Côté, P., et al. 2005, The Astrophysical Journal, 627, 203

Heithausen, A., Bensch, F., Stutzki, J., Falgarone, E., & Panis, J. F. 1998, Astronomy & Astrophysics, 331, L65

Hernquist, L. 1990, The Astrophysical Journal, 356, 359

Herwig, F. 2005, Annual Review of Astronomy & Astrophysics, 43, 435

Hirschmann, M., Dolag, K., Saro, A., et al. 2014, Monthly Notices of the Royal Astronomical Society, 442, 2304

Honma, M., Bushimata, T., Choi, Y. K., et al. 2007, Publications of the Astronomical Society of the Pacific, 59, 889

Hopkins, P. F. 2013, Monthly Notices of the Royal Astronomical Society, 428, 2840

Howell, J. H., Armus, L., Mazzarella, J. M., et al. 2010, The Astrophysical Journal, 715, 572

Hu, C.-Y., Naab, T., Glover, S. C. O., Walch, S., & Clark, P. C. 2017, Monthly Notices of the Royal Astronomical Society, 471, 2151

Hu, C.-Y., Naab, T., Walch, S., Glover, S. C. O., & Clark, P. C. 2016, Monthly Notices of the Royal Astronomical Society, 458, 3528

Hu, C.-Y., Naab, T., Walch, S., Moster, B. P., & Oser, L. 2014, Monthly Notices of the Royal Astronomical Society, 443, 1173

Hubble, E. P. 1925, Popular Astronomy, 33, 252

Hubble, E. P. 1926, The Astrophysical Journal, 64, 321

Ibata, R., Martin, N. F., Irwin, M., et al. 2007, The Astrophysical Journal, 671, 1591

Iwamoto, K., Brachwitz, F., Nomoto, K., et al. 1999, The Astrophysical Journal Supplement Series, 125, 439

Janka, H.-T. 2012, Annual Review of Nuclear and Particle Science, 62, 407

Jeans, J. H. 1902, Philosophical Transactions of the Royal Society of London Series A, 199, 1

Joye, W. A., & Mandel, E. 2003, Astronomical Society of the Pacific Conference Series, Vol. 295, New Features of SAOImage DS9 (Astronomical Society of the Pacific, Orem, UT), 489

Karakas, A. I. 2010, Monthly Notices of the Royal Astronomical Society, 403, 1413

Karl, S. J., Naab, T., Johansson, P. H., et al. 2010, The Astrophysical Journal Letters, 715, L88

Kauffmann, G., & Haehnelt, M. 2000, Monthly Notices of the Royal Astronomical Society, 311, 576

Kennicutt, Robert C., J. 1998a, Annual Review of Astronomy & Astrophysics, 36, 189

Kennicutt, Jr., R. C. 1998b, The Astrophysical Journal, 498, 541

Kormendy, J., Fisher, D. B., Cornell, M. E., & Bender, R. 2009, The Astrophysical Journal Supplement Series, 182, 216

Kormendy, J., & Ho, L. C. 2013, Annual Review of Astronomy & Astrophysics, 51, 511

Krajnović, D., Cappellari, M., de Zeeuw, P. T., & Copin, Y. 2006, Monthly Notices of the Royal Astronomical Society, 366, 787

Krajnović, D., Bacon, R., Cappellari, M., et al. 2008, Monthly Notices of the Royal Astronomical Society, 390, 93

Kramer, C., Stutzki, J., Rohrig, R., & Corneliussen, U. 1998, Astronomy & Astrophysics, 329, 249

Kroupa, P. 2001, Monthly Notices of the Royal Astronomical Society, 322, 231

Kroupa, P., Weidner, C., Pflamm-Altenburg, J., et al. 2013, The Stellar and Sub-Stellar Initial Mass Function of Simple and Composite Populations, Vol. 5 (Springer, Dordrecht), 115

Kruijssen, J. M. D. 2012, Monthly Notices of the Royal Astronomical Society, 426, 3008

Kruijssen, J. M. D. 2015, Monthly Notices of the Royal Astronomical Society, 454, 1658

Krumholz, M. R., McKee, C. F., & Bland -Hawthorn, J. 2019, Annual Review of Astronomy & Astrophysics, 57, 227

Kustaanheimo, P., & Stiefel, E. 1965, J. Reine Angew. Math, 218, 204

Lada, C. J., & Lada, E. A. 2003, Annual Review of Astronomy & Astrophysics, 41, 57

Lada, E. A., Bally, J., & Stark, A. A. 1991, The Astrophysical Journal, 368, 432

Lahén, N., Johansson, P. H., Rantala, A., Naab, T., & Frigo, M. 2018, Monthly Notices of the Royal Astronomical Society, 475, 3934

Lahén, N., Naab, T., Johansson, P. H., et al. 2019, The Astrophysical Journal Letters, 879, L18

Lamers, H. J. G. L. M., Gieles, M., & Portegies Zwart, S. F. 2005, Astronomy & Astrophysics, 429, 173

Larsen, S. S. 2009, Astronomy & Astrophysics, 494, 539

Larsen, S. S., & Richtler, T. 2000, Astronomy & Astrophysics, 354, 836

Larsen, S. S., Strader, J., & Brodie, J. P. 2012, Astronomy & Astrophysics, 544, L14

Larson, R. B. 1974, Monthly Notices of the Royal Astronomical Society, 169, 229

Lauer, T. R. 1985, Monthly Notices of the Royal Astronomical Society, 216, 429

Lejeune, T., Cuisinier, F., & Buser, R. 1997, Astronomy & Astrophysics Supplement Series, 125, 229

Leroy, A. K., Walter, F., Brinks, E., et al. 2008, The Astronomical Journal, 136, 2782

Li, C., & White, S. D. M. 2009, Monthly Notices of the Royal Astronomical Society, 398, 2177

Lin, Y.-T., & Mohr, J. J. 2004, The Astrophysical Journal, 617, 879

Lucy, L. B. 1977, The Astronomical Journal, 82, 1013

Madau, P., & Dickinson, M. 2014, Annual Review of Astronomy & Astrophysics, 52, 415

Maio, U., Dolag, K., Ciardi, B., & Tornatore, L. 2007, Monthly Notices of the Royal Astronomical Society, 379, 963

Maltby, D. T., Almaini, O., Wild, V., et al. 2018, Monthly Notices of the Royal Astronomical Society, 480, 381

Maoz, D., & Mannucci, F. 2012, Publications of the Astronomical Society of Australia, 29, 447

Maoz, D., Mannucci, F., & Brandt, T. D. 2012, Monthly Notices of the Royal Astronomical Society, 426, 3282

Maoz, D., Mannucci, F., Li, W., et al. 2011, Monthly Notices of the Royal Astronomical Society, 412, 1508

Marinacci, F., Pakmor, R., & Springel, V. 2014, Monthly Notices of the Royal Astronomical Society, 437, 1750

Marshall, D. J., Robin, A. C., Reylé, C., Schultheis, M., & Picaud, S. 2006, Astronomy & Astrophysics, 453, 635

McKee, C. F., & Ostriker, J. P. 1977, The Astrophysical Journal, 218, 148

McLaughlin, D. E., & van der Marel, R. P. 2005, The Astrophysical Journal Supplement Series, 161, 304

Messa, M., Adamo, A., Östlin, G., et al. 2018, Monthly Notices of the Royal Astronomical Society, 473, 996

Mihos, J. C., & Hernquist, L. 1996, The Astrophysical Journal, 464, 641

Mikkola, S., & Aarseth, S. J. 1993, Celestial Mechanics and Dynamical Astronomy, 57, 439

Mikkola, S., & Merritt, D. 2006, Monthly Notices of the Royal Astronomical Society, 372, 219

Mikkola, S., & Merritt, D. 2008, The Astronomical Journal, 135, 2398

Mikkola, S., & Tanikawa, K. 1999, Monthly Notices of the Royal Astronomical Society, 310, 745

Misgeld, I., & Hilker, M. 2011, Monthly Notices of the Royal Astronomical Society, 414, 3699

Mo, H. J., Mao, S., & White, S. D. M. 1998, Monthly Notices of the Royal Astronomical Society, 295, 319

Mok, A., Chandar, R., & Fall, S. M. 2019, The Astrophysical Journal, 872, 93

Monaghan, J. J. 1992, Annual Review of Astronomy & Astrophysics, 30, 543

Moni Bidin, C., Mauro, F., Geisler, D., et al. 2011, Astronomy & Astrophysics, 535, A33

Moore, B., Lake, G., & Katz, N. 1998, The Astrophysical Journal, 495, 139

Morris, J. P., & Monaghan, J. J. 1997, Journal of Computational Physics, 136, 41

Naab, T., & Ostriker, J. P. 2017, Annual Review of Astronomy & Astrophysics, 55, 59

Naab, T., Oser, L., Emsellem, E., et al. 2014, Monthly Notices of the Royal Astronomical Society, 444, 3357

Navarro, J. F., Frenk, C. S., & White, S. D. M. 1996, The Astrophysical Journal, 462, 563

Navarro, J. F., Hayashi, E., Power, C., et al. 2004, Monthly Notices of the Royal Astronomical Society, 349, 1039

Nelson, R. P., & Langer, W. D. 1997, The Astrophysical Journal, 482, 796

Noeske, K. G., Weiner, B. J., Faber, S. M., et al. 2007, The Astrophysical Journal Letters, 660, L43

Oh, S.-H., de Blok, W. J. G., Brinks, E., Walter, F., & Kennicutt, Robert C., J. 2011, The Astronomical Journal, 141, 193

Padoan, P., Haugbølle, T., Nordlund, Å., & Frimann, S. 2017, The Astrophysical Journal, 840, 48

Patton, D. R., Pritchet, C. J., Yee, H. K. C., Ellingson, E., & Carlberg, R. G. 1997, The Astrophysical Journal, 475, 29

Paudel, S., Smith, R., Yoon, S. J., Calderón-Castillo, P., & Duc, P.-A. 2018, The Astrophysical Journal Supplement Series, 237, 36

Pawlik, M. M., Taj Aldeen, L., Wild, V., et al. 2018, Monthly Notices of the Royal Astronomical Society, 477, 1708

Peng, C. Y., Ho, L. C., Impey, C. D., & Rix, H.-W. 2002, The Astronomical Journal, 124, 266

Peng, C. Y., Ho, L. C., Impey, C. D., & Rix, H.-W. 2010, The Astronomical Journal, 139, 2097

Pilbratt, G. L., Riedinger, J. R., Passvogel, T., et al. 2010, Astronomy & Astrophysics, 518, L1

Planck Collaboration, Ade, P. A. R., Aghanim, N., et al. 2016, Astronomy & Astrophysics, 594, A13

Plummer, H. C. 1911, Monthly Notices of the Royal Astronomical Society, 71, 460

Poggianti, B. M., Aragón-Salamanca, A., Zaritsky, D., et al. 2009, The Astrophysical Journal, 693, 112

Portegies Zwart, S. F., McMillan, S. L. W., & Gieles, M. 2010, Annual Review of Astronomy & Astrophysics, 48, 431

Preto, M., & Tremaine, S. 1999, The Astronomical Journal, 118, 2532

Putman, M. E., Peek, J. E. G., & Joung, M. R. 2012, Annual Review of Astronomy & Astrophysics, 50, 491

Quinn, T., Katz, N., Stadel, J., & Lake, G. 1997, arXiv e-prints, astro

Rantala, A., Johansson, P. H., Naab, T., Thomas, J., & Frigo, M. 2018, The Astrophysical Journal, 864, 113

Rantala, A., Pihajoki, P., & Johansson, P. H. 2017, in IAU Symposium, Vol. 324, New Frontiers in Black Hole Astrophysics, ed. A. Gomboc, 342–346

Read, J. I., & Hayfield, T. 2012, Monthly Notices of the Royal Astronomical Society, 422, 3037

Read, J. I., Lake, G., Agertz, O., & Debattista, V. P. 2008, Monthly Notices of the Royal Astronomical Society, 389, 1041

Renaud, F., Boily, C. M., Fleck, J. J., Naab, T., & Theis, C. 2008, Monthly Notices of the Royal Astronomical Society, 391, L98

Rubin, V. C., Ford, W. K., J., & Thonnard, N. 1978, The Astrophysical Journal Letters, 225, L107

Sackett, P. D., Morrisoni, H. L., Harding, P., & Boroson, T. A. 1994, Nature, 370, 441

Saitoh, T. R., & Makino, J. 2013, The Astrophysical Journal, 768, 44

Salim, S., Rich, R. M., Charlot, S., et al. 2007, The Astrophysical Journal Supplement Series, 173, 267

Sancisi, R., Fraternali, F., Oosterloo, T., & van der Hulst, T. 2008, The Astronomy and Astrophysics Review, 15, 189

Sandage, A., & Binggeli, B. 1984, The Astronomical Journal, 89, 919

Sanders, D. B., & Mirabel, I. F. 1996, Annual Review of Astronomy & Astrophysics, 34, 749

Schawinski, K., Urry, C. M., Simmons, B. D., et al. 2014, Monthly Notices of the Royal Astronomical Society, 440, 889

Schaye, J., Crain, R. A., Bower, R. G., et al. 2015, Monthly Notices of the Royal Astronomical Society, 446, 521

Schechter, P. 1976, The Astrophysical Journal, 203, 297

Schiminovich, D., Wyder, T. K., Martin, D. C., et al. 2007, The Astrophysical Journal Supplement Series, 173, 315

Schmidt, M. 1959, The Astrophysical Journal, 129, 243

Sérsic, J. L. 1963, Boletin de la Asociacion Argentina de Astronomia La Plata Argentina, 6, 41

Shakura, N. I., & Sunyaev, R. A. 1973, Astronomy & Astrophysics, 500, 33

Simien, F., & de Vaucouleurs, G. 1986, The Astrophysical Journal, 302, 564

Sofue, Y., Honma, M., & Omodaka, T. 2009, Publications of the Astronomical Society of the Pacific, 61, 227

Sparke, L. S., & Gallagher, John S., I. 2007, Galaxies in the Universe: An Introduction (Cambridge University Press, Cambridge, UK)

Speagle, J. S., Steinhardt, C. L., Capak, P. L., & Silverman, J. D. 2014, The Astrophysical Journal Supplement Series, 214, 15

Spitzer, Lyman, J. 1958, The Astrophysical Journal, 127, 17

Springel, V. 2005, Monthly Notices of the Royal Astronomical Society, 364, 1105

Springel, V., Di Matteo, T., & Hernquist, L. 2005a, Monthly Notices of the Royal Astronomical Society, 361, 776

Springel, V., & Hernquist, L. 2002, Monthly Notices of the Royal Astronomical Society, 333, 649

Springel, V., & Hernquist, L. 2003, Monthly Notices of the Royal Astronomical Society, 339, 289

Springel, V., White, S. D. M., Tormen, G., & Kauffmann, G. 2001a, Monthly Notices of the Royal Astronomical Society, 328, 726

Springel, V., Yoshida, N., & White, S. D. M. 2001b, New Astronomy, 6, 79

Springel, V., White, S. D. M., Jenkins, A., et al. 2005b, Nature, 435, 629

Stasińska, G. 1990, Astronomy & Astrophysics Supplement Series, 83, 501

Stierwalt, S., Besla, G., Patton, D., et al. 2015, The Astrophysical Journal, 805, 2

Strömgren, B. 1939, The Astrophysical Journal, 89, 526

Tody, D. 1986, Society of Photo-Optical Instrumentation Engineers (SPIE) Conference Series, Vol. 627, The IRAF Data Reduction and Analysis System (Society of Photo-Optical Instrumentation Engineers, Bellingham, WA), 733

Toomre, A., & Toomre, J. 1972, The Astrophysical Journal, 178, 623

Tremmel, M., Governato, F., Volonteri, M., & Quinn, T. R. 2015, Monthly Notices of the Royal Astronomical Society, 451, 1868

Trujillo, I., Erwin, P., Asensio Ramos, A., & Graham, A. W. 2004, The Astronomical Journal, 127, 1917

Trujillo-Gomez, S., Reina-Campos, M., & Kruijssen, J. M. D. 2019, Monthly Notices of the Royal Astronomical Society, 488, 3972

van der Kruit, P. C., & Searle, L. 1981, Astronomy & Astrophysics, 95, 105

van der Marel, R. P., & Franx, M. 1993, The Astrophysical Journal, 407, 525

Vanzella, E., Calura, F., Meneghetti, M., et al. 2019, Monthly Notices of the Royal Astronomical Society, 483, 3618

Vogelsberger, M., Genel, S., Springel, V., et al. 2014, Monthly Notices of the Royal Astronomical Society, 444, 1518

Vogelsberger, M., Marinacci, F., Torrey, P., et al. 2018, Monthly Notices of the Royal Astronomical Society, 474, 2073

Wang, L., Spurzem, R., Aarseth, S., et al. 2016, Monthly Notices of the Royal Astronomical Society, 458, 1450

Westera, P., Lejeune, T., Buser, R., Cuisinier, F., & Bruzual, G. 2002, Astronomy & Astrophysics, 381, 524

Wetzstein, M., Nelson, A. F., Naab, T., & Burkert, A. 2009, The Astrophysical Journal Supplement Series, 184, 298

White, S. D. M., & Frenk, C. S. 1991, The Astrophysical Journal, 379, 52

White, S. D. M., & Rees, M. J. 1978, Monthly Notices of the Royal Astronomical Society, 183, 341

Whitmore, B. C., Chandar, R., & Fall, S. M. 2007, The Astronomical Journal, 133, 1067

Whitmore, B. C., Zhang, Q., Leitherer, C., et al. 1999, The Astronomical Journal, 118, 1551

Whitmore, B. C., Chandar, R., Schweizer, F., et al. 2010, The Astronomical Journal, 140, 75

Wiersma, R. P. C., Schaye, J., & Smith, B. D. 2009, Monthly Notices of the Royal Astronomical Society, 393, 99

Wild, V., Almaini, O., Dunlop, J., et al. 2016, Monthly Notices of the Royal Astronomical Society, 463, 832

Woosley, S. E., & Weaver, T. A. 1995, The Astrophysical Journal Supplement Series, 101, 181

Wuyts, S., Förster Schreiber, N. M., van der Wel, A., et al. 2011, The Astrophysical Journal, 742, 96

York, D. G., Adelman, J., Anderson, John E., J., et al. 2000, The Astronomical Journal, 120, 1579